



INAOE

Nonlinear acousto-optics: improvements in optical spectrum analysis

By:

M. Sc. Adán Omar Arellanes Bernabe

A dissertation Submitted to the program in Optics.

Optics department.

In partial fulfillment of the requirements for the degree of

**DOCTOR OF SCIENCES
WITH SPECIALITY IN OPTICS**

At:

**National Institute for Astrophysics,
Optics, and Electronics.**

November 2016

Tonantzintla, Puebla.

Advisor:

Dr. Alexander S. Shcherbakov
INAOE Researcher

Optics Department

©INAOE 2016

All rights reserved

The author hereby grants to INAOE permission to reproduce and to distribute copies of this thesis in whole or in part.



Abstract

In this work, the non-linear acousto-optical interaction is studied for the collinear and the non-collinear cases. First, a non-linear regime of the collinear acousto-optical interaction is considered with acoustic waves of finite amplitude considering the acoustic losses in a crystalline acousto-optical cell. The results of this analysis were confirmed first in a calcium molybdate (CaMoO_4) acousto-optical cell. After this, the results were extrapolated to predict the performances of a lithium niobate (LiNbO_3) acousto-optical cell oriented to the application in astrophysical spectroscopy near the ultraviolet range. This material, specifically, was in need of further analysis due to known phenomena within it that could affect the capabilities of such cell.

Then, the non-collinear acousto-optical interaction is studied for the multiphonon light scattering in the Bragg regime. This regime allows only two possible cases of multiphonon light scattering, namely, the two- and three-phonon acousto-optical interaction. Together with this, a specific degree of freedom for this acousto-optical interaction is introduced to regulate the acoustic frequency necessary for the interaction to occur. The multiphonon light scattering was theoretically analyzed and experimented in two different crystals; calomel (Hg_2Cl_2) for the two-phonon interaction and tellurium dioxide (TeO_2) for the three-phonon case.

Resumen

En este trabajo se estudia la interacción acusto-óptica no-lineal para los regímenes colineal y no-colineal. Primero, un régimen no-lineal de la interacción acusto-óptica colineal está bajo consideración con ondas acústicas de amplitud finita tomando en cuenta las pérdidas acústicas en una celda acusto-óptica cristalina.

Los resultados de este análisis fueron confirmados primero en una celda acusto-óptica de molibdato de calcio (CaMoO_4). Luego de esto, los resultados fueron extrapolados para predecir el desempeño de una celda acusto-óptica de niobato de litio (LiNbO_3) encaminada a su aplicación en espectroscopía astrofísica cerca del rango ultravioleta. Este material en particular, necesitó de un análisis más profundo debido a fenómenos conocidos en él que podrían afectar las capacidades de una celda de este material.

Después, la interacción acusto-óptica no colineal se estudió para el esparcimiento multifonón de luz en el régimen de Bragg. Este régimen sólo permite dos posibles casos, la interacción acusto-óptica de dos y de tres fonones. Junto con esto, un grado de libertad específico de esta interacción acusto-óptica se introdujo para regular la frecuencia acústica necesaria para que ocurra la interacción. El esparcimiento multifonón de luz se analizó teóricamente en dos cristales diferentes; cloruro de mercurio (Hg_2Cl_2) para el caso de la interacción de dos fonones y dióxido de telurio (TeO_2) para el caso de tres fonones.

List of figures

Chapter 1

Fig. 1.1. The index ellipsoid for a uniaxial medium. The shaded ellipse is perpendicular to the \vec{k} vector

Fig. 1.2. Projection of the index ellipsoid into the $k - z$ plane.

Fig. 1.3. Index surfaces for: (a) isotropic, (b) positive uniaxial, (c) negative uniaxial, and (d) biaxial medium.

Fig. 1.4. Acoustic waves in a medium; (a) pure longitudinal wave and (b) pure shear wave.

Fig. 1.5. Simple wave vector diagram of light scattering in isotropic media.

Fig. 1.6. Anomalous light scattering in an anisotropic media.

Fig. 1.7. Cuasi-collinear interaction in an anisotropic media, in the collinear interaction the three wave vectors are in the same line.

Fig. 1.8. Two-phonon light scattering occurred in anisotropic media.

Fig. 1.9. Acoustic wave traveling in a crystalline material and generating a phase grating. L is the interaction length, D is the aperture of the cell, Λ is the acoustic wavelength, and θ_B is the Bragg angle.

Chapter 2

Fig. 2.1. A 2D-plot on the plane $(\alpha x, \sigma x)$ with lines corresponding to $N = 0, 1, 2$

Fig. 2.2. Restricting the number N of unit valued maxima; the particular case of $\alpha = 0.1 \text{ cm}^{-1}$, $\sigma = 1 \text{ cm}^{-1}$ and $N \leq 2$ is shown.

Fig. 2.3. Graphical solution to Eq.(5a); positions for the unit-valued maxima as function of collinear interaction length and σ is a parameter for $N = 0$ and $\alpha = 0.1 \text{ cm}^{-1}$.

Fig. 2.4. The normalized scattered light distributions versus the dimensional length of interaction with $\alpha = 0.1 \text{ cm}^{-1}$: the dashed line is for $\sigma = 0.5 \text{ cm}^{-1}$ and solid line is for $\sigma = 1 \text{ cm}^{-1}$

Fig. 2.5. The 3D-plots of the scattered light intensity profile with $q_0/q_1 \approx 1$: (a) for the absolute values on the interval $0 \leq \sigma x < 3\pi$ and (b) for the normalized distribution on the interval $0 \leq \sigma x \leq \pi$.

Fig. 2.6. The 2D-plots $|C_1[(\sigma x), (\eta x)]|^2$ for the products $1.0 \leq \sigma x < \pi$ with $q_0/q_1 \approx 1$: (a) for the absolute values and (b) after normalization by the zero magnitudes.

Fig. 2.7. The light intensity $|C_1(x)|^2$ and a one-side dimensionless mismatch ηx versus the product σx .

Fig. 2.8. A 2D-contour for the normalized light intensity on the plane $[(\sigma x), (\eta x)]$ on the interval $0 \leq \sigma x \leq \pi$.

Fig. 2.9. The 2D-plots $|C_1[(\sigma x), (\eta x)]|^2$ for the products $\pi < \sigma x < 2\pi$ with $q_0/q_1 \approx 1$: (a) for the absolute values and (b) after normalization by the zero magnitudes.

Fig. 2.10. A 2D-contour plot for the normalized light intensity on the plane $[(\sigma x), (\eta x)]$ on the interval $0 \leq \sigma x < 3\pi$.

Fig. 2.11. The 3D plots for the absolute values of the scattered light intensity profile with $\alpha \neq 0$ and $q_0/q_1 \approx 1$ on the interval $0 \leq \sigma x \cong 3\pi$: (a) $\alpha x = 0.1$ and (b). $\alpha x = 0.5$.

Fig. 2.12. The 2D-profiles $|C_1[(\sigma x), (\eta x)]|^2$ with $q_0/q_1 \approx 1$: (a) $\alpha = 0.1 \text{ cm}^{-1}$ and $\sigma = 0.5 \text{ cm}^{-1}$ with $X_0 = 3.768 \text{ cm}$ and $X_1 = 28.55 \text{ cm}$, (b) $\alpha = 0.1 \text{ cm}^{-1}$ and $\sigma = 1 \text{ cm}^{-1}$ wherein $X_0 = 1.709 \text{ cm}$, $X_1 = 6.372 \text{ cm}$, and $X_2 = 15.39 \text{ cm}$

Fig. 2.13. Acoustic power density P vs. the parameter σ at $\lambda = 671 \text{ nm}$ in the above-chosen collinear CaMoO_4 -crystalline cell.

Fig. 2.14. Optical absorption vs. the incident light wavelength λ : within a wide spectrum (a) and in near-ultraviolet range (b) for various concentration of Mg. Solid lines are for infinitely small incident optical power density, i.e. for $\alpha_0(\lambda)$, while dotted lines are for the above-described combined spectral flux, i.e. at the saturation

Fig. 2.15. Level of optical losses vs. 4%: Mg-doped LiNbO_3 crystal length: the dotted straight lines are for the best case, i.e. for only the linear losses $\alpha_T \approx \alpha_0$, the dashed straight lines are for the worst case, i.e. for optical losses $\alpha_T = \alpha_0 + \alpha_2 I_0$, and the solid curves are for varying α_T in the second approximation, described by Eq.(23)

Fig. 2.16. Spectral dependencies for the light-induced birefringence change $\delta|\Delta n|_\lambda$: in the congruent LiNbO_3 crystal (red line) and in the congruent Mg : LiNbO_3 (blue line)

Fig. 2.17. Schematic arrangement of the experimental set-up

Fig. 2.18. The scattered light intensity $|C_1|^2$ versus the acoustic power density P with $\alpha = 0.0261 \text{ cm}^{-1}$ (solid line is for theory and circles are for experiment at $f = 61.24 \text{ MHz}$, $\lambda = 532 \text{ nm}$) and $\alpha = 0.0615 \text{ cm}^{-1}$ (squares are for experiment at $f_{\text{max}} = 94.34 \text{ MHz}$, $\lambda = 444 \text{ nm}$) in the CaMoO_4 -cell.

Fig. 2.19. Combined diagram reflecting both the 2D-theoretical plots with the product $\alpha L \approx \{0, 0.0575, 0.114, 0.271\}$ and all the above-noted experimental points. The lossless case is $\alpha L = 0$.

Fig. 2.20. The digitized oscilloscope traces for the scattered light intensity $|C_1|^2$ for the green light with $\lambda = 532 \text{ nm}$ observed at the output of the collinear CaMoO_4 cell near the central carrier acoustic frequency $f_0 = 61.24 \text{ MHz}$ and estimated at the level 0.405. Reshaping the

transmission function is followed at the same optical pump in variable scales: (a) $\sigma L \approx \pi/2$, $P \approx 0.0365 [W/mm^2]$; (b) $\sigma L \approx 2.5$, $P \approx 0.0925 [W/mm^2]$, (c) $\sigma L \approx 3.0$, $P \approx 0.133 [W/mm^2]$, and (d) $\sigma L \approx 3.2$, $P \approx 0.152 [W/mm^2]$.

Fig. 2.21. Combined plots of the spectral resolution $\delta\lambda$ and the relative scattered light intensity vs. the acoustic power density P for the pure slow shear elastic mode passing along the [010]-axis in the congruent $LiNbO_3$ -crystal: (a) at $\lambda = 405nm$, $f = 1.04 GHz$, $\alpha = 0.0991 cm^{-1}$, $\alpha_0 \approx 0.17 cm^{-1}$ and (b) at $\lambda = 440nm$, $f = 0.896 GHz$, $\alpha = 0.0740 cm^{-1}$, $\alpha_0 \approx 0.12 cm^{-1}$. Here, the solid lines (theory) and circles (experiment) are for the spectral resolution $\delta\lambda$, while the dotted lines (theory) and squares (experiment) are for the relative efficiency of the light scattering.

Chapter 3

Fig. 3.1. The non-collinear two-phonon AOI vector diagram: (a) and doubling the spectral resolution (b). Spots 1,2,3,... are related to one-phonon processes, while additional spots a,b,c,... describe refining the resolution caused by the appearance of a two-phonon interaction.

Fig. 3.2. A 3D-bandshape for the non-collinear two-phonon AOI; the axis σx (the dimensionless acoustic power density) reflects nonlinearity of the phenomenon, ηx is the dimensionless angular-frequency mismatch.

Fig. 3.3. Maxima of the non-collinear two-phonon AOI reflecting its strongly non-linear behavior along the line $\eta x = 0$.

Fig. 3.4. The intensity – mismatch profiles related to first four maxima of the non-collinear two-phonon AOI.

Fig. 3.5. Two examples of vector diagrams, indexed by “a” and “b”, inherent in nonlinear two-phonon AOI with the fixed ratio V/λ . The extraordinary refractive index n_E is described by an external faint ellipsoid, while a darker internal sphere shows the ordinary refractive index $n_O \equiv N_O$. Here, $\bar{k}_m^{a,b}$ and $\bar{K}_{a,b}$ are the wave vectors of light and acoustic waves.

Fig. 3.6. The product $2bD$ and the desirable aperture D , connected with the spectral resolution, for the slow shear elastic mode in calomel.

Fig. 3.7. The product $2bD$ and the desirable aperture D , connected with the spectral resolution, for the longitudinal elastic mode in calomel.

Fig. 3.8. The vector diagram for two-phonon light scattering in calomel where ψ is the tilt angle.

Fig. 3.9. Resolving power of the calomel-based AOC vs. the optical aperture D , the length of acousto-optical interaction L , and the acoustic attenuation parameter B .

Fig. 3.10. Optimized 2D-profiles of the light distributions at the output facet of the calomel-made AOC at $f_0 \approx 57.8, 71.0, \text{ and } 82.6$ MHz with $\alpha \approx 0.8851, 0.1336, \text{ and } 0.1808$ cm^{-1} .

Fig. 3.11. An example of an optimized 3D-profile of the issuing light distribution with $f_0 = 71.0$ MHz and $\alpha \approx 0.1336$ cm^{-1} .

Fig. 3.12. Theoretical profiles for the Gaussian centered approximations with the dimensionless apodization parameters $\beta = 0.50, 1.15, 2.10$.

Fig. 3.13. Theoretical logarithmic profiles of resolvable spots with the dimensionless apodization parameters $\beta = 0.50, 1.15, 2.10$.

Fig. 3.14. Optimized 2D-profiles of the light distributions at the output facet of the calomel-made AO cell at $f_0 \approx 50.1, 57.6$ and 64.66 MHz with $\alpha \approx 0.0665, 0.0885,$ and 0.1108 cm^{-1} .

Fig. 3.15. An example of the optimized 3D-profiles for the issuing light distributions at $f_0 \approx 57.8$ MHz with $\alpha \approx 0.885 \text{ cm}^{-1}$.

Fig. 3.16. Theoretical profiles for the Gaussian centered approximations with the dimensionless apodization parameters $\beta = 3.1, 6.0,$ and 9.0 .

Fig. 3.17. Theoretical profiles of resolvable spots with the broadening parameters $\kappa \approx 1.121, 1.248,$ and 1.391 for the same dimensionless apodization parameters $\beta = 0, 3.1, 6.0,$ and 9.0 .

Fig. 3.18. Theoretical logarithmic profiles of resolvable spots with the dimensionless apodization parameters $\beta = 0, 3.1, 6.0,$ and 9.0 .

Fig. 3.19. The design of the calomel AOC: (a) depicts the general view with the Bragg angles of incidence and scattering in three orders, while (b) shows the top view with the needed tilt angle ψ .

Fig. 3.20. The layout of the optical scheme; only the 2-nd order of a two-phonon AOI is shown.

Fig. 3.21. The design of the calomel AOC.

Fig. 3.22. Design of the calomel AO cell .

Fig. 3.23. Experimentally obtained frequency bandshape for the AOC made of calomel. The full width at the half-maximum level can be estimated by about of $\Delta f_{\text{exp}} \approx 5.1$ MHz.

Fig. 3.24. Light intensity profile of an individual resolvable spot observed in the 2nd order of scattering. It is a result of the standard processing provided by the CCD-camera. The full width at the half-maximum of the main lobe can be estimated by about of 8.2 microns.

Fig. 3.25. Experimentally obtained frequency bandshape of the calomel-made AOC at $f_0 \approx 82.6$ MHz and $\lambda = 405$ nm.

Fig. 3.26. Light intensity profile of an individual resolvable spot for the calomel-based AOC at $\lambda = 405$ nm.

Fig. 3.27. A layout of the experimental set-up; only the 2-nd order of light scattering is depicted.

Fig. 3.28. Experimentally obtained frequency band-shape of the calomel-made AO cell at $f_0 \approx 57.8$ MHz and $\lambda = 405$ nm.

Fig. 3.29. Light intensity profile of an individual resolvable spot for the calomel-based AO cell at $\lambda = 405$ nm.

Fig. 3.30. Unit-level maxima vs. the dimensionless acoustic power parameter σx at $f_0 \approx 57.8$ MHz and $\eta x = 0$: dotted line (theory) is for $a = 0$; solid line (theory) and squares (experiment) are for $z_A \approx 2$ cm, $a = 0.177$; while dashed line (theory) and triangles (experiment) are for $z_B \approx 4$ cm, $a = 0.354$.

Chapter 4

Fig. 4.1. The non-collinear three-phonon AOI vector diagram (a) and scheme of tripling the spectral resolution (b). Spots 1, 2, 3,... are related to a one-phonon AOI, the additional spots a, b, c,... describe a two-phonon AOI, while the extra-spots α , β , γ ,... correspond to the three-phonon AOI refining the spectral resolution.

Fig. 4.2. Relative light intensity $|C_3|^2$ distributions: (a) 3D-plot in the coordinates $\sigma_a x$ and ηx ; (b) a pair of 2D-plots with $\eta = 0$; when $\chi = 1.15$ (solid line) one can see a sequence of the unit level maxima, but when, for example $\chi = 1.0$ (dashed line), this sequence becomes destroyed.

Fig. 4.3. Relative light intensity $|C_3|^2$, scattered into the first maxima inherent in the three-phonon AOI, with various ratios χ lying between 0.5 and 2.0 due to the acoustic power density described by σ_a with $\eta = 0$: a) $|C_3|^2$ vs. the parameter σ_a , b) $|C_3|^2$ vs. the ratio χ , the inter- relation between σ_a and χ is shown too, and c) The corresponding 3D-plot with various ratios χ lying between 0.5 and 1.5 due to the acoustic power density described by σ_a with $\eta = 0$.

Fig. 4.4. Transmission functions i.e. relative light intensities $|C_3|^2$ distributions with $\eta \neq 0$ and $\chi = 1.15$ at the isolated points $\sigma_a x = 2.72, 8.16, \text{ and } 13.60$ specific to the unit-level maxima from Fig. 2b.

Fig. 4.5. The 2D-plots for relative light intensity $|C_3|^2$ distributions vs. in the dimensionless coordinate $\sigma_a x$ with $\eta = 0$ and $q_n/q_a = 1.15$; solid lines are for $a = 0$ and 1.0, dashed line is for $a = 0.3$, and dotted line is for $a = 0.5$. One can see a sequence of the unit level maxima and the dynamics of scaling due to effect of linear acoustic losses.

Fig. 4.6. Index surfaces for the ordinary refractive index (inner ellipsoid) and the extraordinary refractive index (outer ellipsoid). The two semi-ellipses represent the intersections of these ellipsoids with the plane of light scattering (yellow plane); declined by the tilt angle ϕ .

Fig. 4.7. Acoustic frequency and ellipticity of the incident light vs. the tilt angle ϕ needed for the three-phonon AOI in the TeO_2 crystal.

Fig. 4.8. Relations between the photo-elastic constants p_a and p_n .

Fig. 4.9. Optimized 2D-profiles of the light distributions at the output facet of the tellurium dioxide-made AOC at $f_3 = 65.0$ MHz with $\alpha \approx 0.1411 \text{ cm}^{-1}$ for the corresponding D_k (solid lines); the dashed line is for a non-optimized profile.

Fig. 4.10. An example of an optimized 3D-profile of the issuing light distribution at $f_3 = 65.0$ MHz and $(\sigma_a x)_{1,\text{opt}}^{(4)} \approx 3.47$ with $D_4 = 4.0$ cm, and $\alpha \approx 0.1411 \text{ cm}^{-1}$.

Fig. 4.11. Theoretical logarithmic profiles of resolvable spots with the dimensionless apodization parameters β_k .

Fig. 4.12. Design of the tellurium dioxide AOC for the three-phonon AOI.

Fig. 4.13. A layout of the experimental set-up; only the 3-rd order of light scattering is depicted.

Fig. 4.14. Experimentally obtained frequency bandshape of the TeO_2 -made AOC at $f_3 \approx 65$ MHz and $\lambda = 488$ nm.

Fig. 4.15 Light intensity profiles of two individual resolvable spots for the TeO_2 -based AOC at $f_3 \approx 65$ MHz and $\lambda = 488$ nm: (a) $D_{4,M} \approx 4.0$ cm and (b) $D_{6,M} \approx 6.0$ cm.

List of tables

Chapter 2

Table 2.1. Dispersion of the main refractive indices n_e and n_o in the calcium molybdate crystal [2.18].

Chapter 3

Table 3.1. Theoretical estimations; here, $\delta f = V / 2 D$ and $\delta \lambda = \delta f \lambda / f_0$ are frequency and spectral resolutions, $f_0 = \sqrt{B/(D\Gamma)}$ is the central acoustic frequency, and the product $2 b D = \lambda^2 / \delta \lambda$ includes the birefringence factor

Table 3.2. Practical estimations; here, $\Delta f = 2 |f - f_0| \approx n_0 V^2 / (\lambda L f_0)$ and $\Delta \lambda = \Delta f \lambda / f_0$ are frequency and spectral bandwidths, while $N = \Delta f / \delta f = \Delta \lambda / \delta \lambda$ is the number of resolvable spots.

Table 3.3. Pre-experimental estimations; here, $d_s = \kappa \lambda F / D$ is an ideal spot size in the approximation of geometric optics with the correction factor of apodization $\kappa \approx 1.019, 1.043,$ and $1.080, F = 85$ cm, and $D = 5.2$ cm.

Table 3.4. Pre-experimental estimations; here, $d_s = \lambda F / D$ is an ideal spot size in the approximation of geometric frequency, M_2 is the figure of acousto-optical merit, and P_2 is the acoustic power density needed for the second maxima.

Table 3.5. Comparison of theoretical and experimental data; $\delta f_{Th} \approx 3.337$ kHz and $\delta f_M \approx 4.18$ kHz.

Table 3.6. Theoretical and experimental data with nonlinear apodization for: $\delta f_{Th} \approx 3.337$ kHz with $\kappa \approx \{1.121, 1.248, 1.391\}$.

Chapter 4

Table 4.1. Theoretical characterization of TeO₂ AOC.

Table 4.2. Theoretical estimations with: $L \approx 1.2$ cm; type of the elastic mode is S [110] with $f_3 \approx 65$ MHz at $\lambda = 488$ nm; the product $\delta \lambda_K = \lambda^2 / (3 b_3 D_K)$ includes the birefringence factor b_3 . Then, $d_{s,k} = \kappa_k \lambda F / D_k$ is an ideal spot size in the approximation of geometric optics

Table 4.3. Comparison of theoretical and experimental data; $\Delta f_T \approx 562$ kHz and $\Delta f_M \approx 798$ kHz; $\Delta \lambda_T \approx 42.20$ Å and $\Delta \lambda_M \approx 60.05$ Å; at $\lambda = 488$ nm

Acknowledgements

I thank to CONACyT for the financial support and to the INAOE for giving me all the knowledge to makes this work possible.

I thank my advisor Dr. Alexander Shcherbakov for sharing all his experience, knowledge, and wisdom.

Thanks to my co-authors Dr. Vahram Chavushyan, Dr. Sergey A. Nemov, Dr. Miguel Chavez, Dr. Emanuele Bertone, Dr. Eduardo Tepichín, and Dr. Arturo Aguirre.

Thanks to my sinodals Dr. David Sánchez de la Llave, Dr. Ruben Ramos, Dr. Gabriel Martínez, Dr. Miguel Angel Bello and Dr. Mauro Sánchez for their help and support.

Thanks to all my professors and specially Dr. Ponciano Rodriguez, Dr. Victor Arrizon, Dr. Eugene Kuzin, Dr. Baldemar Ibarra, Dr. Sabino Chavez, and Dr. Nikolai Korneev.

Also thanks to my colleagues and friends for all their support and company during my studies.

Special thanks to my family for their love and support.

Contents

1. Acousto-optics	3
1.1. Background	3
1.2. Light propagation in anisotropic media	3
1.2.1. Index ellipsoid	3
1.2.2. Isotropic, uniaxial and biaxial crystals	5
1.3. Ultrasound propagation in anisotropic media	6
1.3.1. Pure longitudinal and shear modes	7
1.4. Acousto-optical interaction	7
1.4.1. General theory; wave-vector diagrams	7
1.4.2. Collinear and non-collinear interaction	8
1.4.3. Acousto-optics in crystals	9
1.5. Formulation of the problem	13
2. Transmission function of collinear acousto-optical interaction	14
2.1. Introduction	14
2.2. Three-wave collinear interaction	15
2.3. Efficiency of collinear interaction in different materials	18
2.4. Resolution of collinear interaction	20
2.4.1. Traditional approach	20
2.4.2. Medium without acoustical losses	21
2.4.3. Medium with acoustical losses	24
2.5. Some estimations	26
2.5.1. CaMoO_4	26
2.5.2. LiNbO_3	27
2.5.2.1. Induced absorption	27
2.5.2.2. Photorefraction	29
2.6. General scheme for experiments	32
2.7. Experimental results	33
2.8. Conclusions	37
3. Two- phonon acousto-optical interaction	39
3.1. Introduction	39
3.2. Non-collinear two-phonon interaction	41
3.3. $\alpha\text{-Hg}_2\text{Cl}_2$ acousto-optical cell characterization	44
3.3.1. Frequency and length	44

3.3.2. Efficiency	46
3.3.3. Resolving power	47
3.4. Local analysis of the Two-phonon acousto-optical interaction	51
3.4.1. First maxima	51
3.4.2. Second maxima	53
3.5. Theoretical estimations of a dispersive component based on the calomel-made crystalline AOC	56
3.5.1. Effect of the acoustic beam divergence	56
3.5.2. General estimations for the calomel-made AOC	57
3.5.3. Figure of acousto-optical merit for the non-collinear two-phonon light scattering in calomel crystal	57
3.6. Proof of principal experimental data	58
3.6.1. Experiment arrangement	58
3.6.1.1. First Maxima	58
3.6.1.2. Second Maxima	61
3.6.2. Experimental results	62
3.6.2.1. First Maxima	62
3.6.2.2. Second Maxima	67
3.7. Conclusion	70
4. Three phonon acousto-optical interaction	73
4.1. Introduction	73
4.2. Three phonon Bragg acousto-optical interaction	74
4.2.1. General solution	74
4.2.2. Transmission function without acoustic losses	76
4.2.3. Transmission function with acoustic losses	78
4.3. Frequency of a three phonon acousto-optical interaction	78
4.4. Photo-elastic effect in Tellurium dioxide	81
4.5. The nonlinear apodization	82
4.6. Theoretical estimations of the Tellurium dioxide cell	84
4.7. Proof of principle experiments	86
4.7.1. Experimental arrangement	86
4.7.2. Experimental results	87
4.8. Conclusion	90
5. General conclusions	92
6. Bibliography	93
7. Statements	98

Chapter 1

Acousto-Optics

In this chapter, the fundamental physical optics required to understand the acousto-optical interaction is discussed. First, the behavior of the light in anisotropic media is explained. Then, the isotropic propagation of sound in bulk materials is described. Later, the theoretical approach for the interaction of optical and acoustical waves is explained to be taken as a basis for the rest of the chapters.

1.1. Background

The interaction of optical and acoustical waves was proposed in the beginning of 20th century by Brillouin. Several developments have been made since then and mostly after the discovery of the laser in 1960s. As in every physical phenomenon, the first attempts to understand and establish a theoretical model were done with various restrictions and for linear regimes.

1.2. Light Propagation in Anisotropic Media

The simplest case of light propagation is the isotropic one, where the induced polarization is always parallel to the electric field and it is proportional to the susceptibility independently to the direction of the applied field. In an anisotropic media, the induced polarization is determined by the direction of propagation of the light and its state of polarization.

1.2.1. Index Ellipsoid and Surfaces.

These two concepts must be introduced and described in a mathematically way to make it possible to work with them and help to visualize the differences between each type of crystals. One of them is the *index ellipsoid*, which describes the refraction index of a given material depending on the direction of propagation and polarization of a given light field. This concept is described by the relation [1.2]

$$\frac{x^2}{\epsilon_{xx}} + \frac{y^2}{\epsilon_{yy}} + \frac{z^2}{\epsilon_{zz}} = 1, \quad (1.1)$$

where ϵ_{ii} are the components of the main diagonal in the dielectric tensor ϵ , and knowing that:

$$n = \sqrt{\epsilon\mu}, \quad (1.2)$$

where n is the refractive index and μ the magnetic permeability which is effectively unity for all the materials which are concerned for this thesis. Now it is possible to rewrite (1.1) into:

$$\frac{x^2}{n_x^2} + \frac{y^2}{n_y^2} + \frac{z^2}{n_z^2} = 1. \quad (1.3)$$

As an example, let $n_x = n_y = n_o$, $n_z = n_e$, and let $n_o > n_e$ so Eq.(1.3) becomes:

$$\frac{x^2 + y^2}{n_o^2} + \frac{z^2}{n_e^2} = 1, \quad (1.4)$$

with this spheroid in mind, one can consider the wave vector \vec{k} in the direction of an arbitrary angle θ to the z -axis. Then, any plane that touches the origin and that is perpendicular to this wave vector will intersect the spheroid in an ellipse, see Fig. 1.1, which will have the following properties:

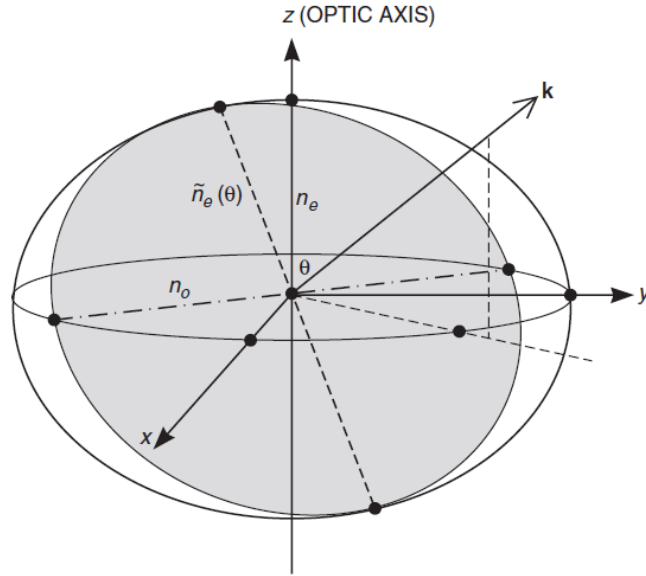


Fig 1.1. The index ellipsoid for a uniaxial medium. The shaded ellipse is perpendicular to the \vec{k} vector

- 1) The axes of this ellipse define two orthogonal directions for the electric displacement \vec{D} which satisfy simultaneously the Maxwell's equations and the constitutive relation:

$$\vec{D} = \epsilon_0 \epsilon \vec{E}. \quad (1.5)$$

One of the two axes is always in the $x - y$ plane and corresponds to the direction of polarization of the ordinary wave and its length is independent of the direction of \vec{k} . The other axis is related to the extraordinary wave and its length depends on the angle θ between \vec{k} and the z -axis.

- 2) The length of the semi-axes of the ellipse is the refractive index, n_o for the ordinary wave and $\tilde{n}_e(\theta)$ for the extraordinary wave. The value of $\tilde{n}_e(\theta)$ is easily estimated from Fig. 1.2. The length of the bold line perpendicular to k in Fig. 1.2 is the value of:

$$\tilde{n}_e(\theta) = \sqrt{\frac{\cos^2 \theta}{n_o^2} + \frac{\sin^2 \theta}{n_e^2}}. \quad (1.6)$$

On the other hand, there are the *index surfaces* which represent the values of the refractive indices for all the possible directions of propagation of the wave vector \vec{k} .

Using the previous example, the index surface would look like Fig. 1.3b or 1.3c. The planes of polarization for the ordinary and extraordinary indices are perpendicular. This characteristic will be particularly useful for some applications in the collinear acousto-optical tunable filters (AOTF).

The present work is focused on this representation and it will be explained for the different crystal types in the next section.

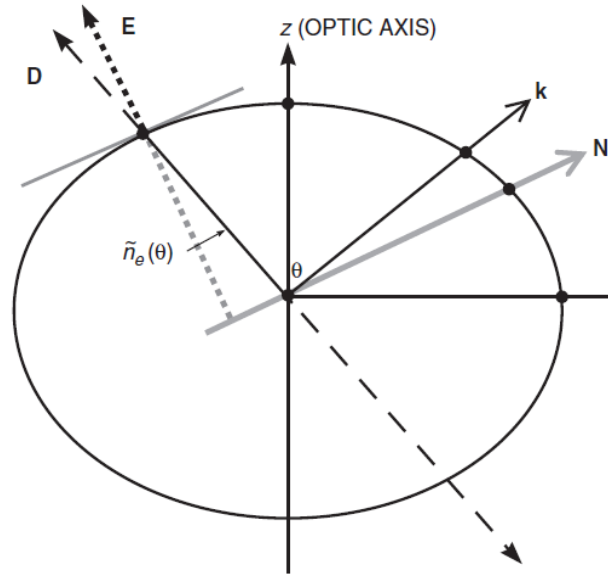


Fig. 1.2. Projection of the index ellipsoid into the $\mathbf{k} - z$ plane.

1.2.2. Isotropic, uniaxial and biaxial crystals

In crystals, the optical isotropy is observed in cubic crystal systems (also applicable for amorphous media), in these systems the dielectric tensor ϵ is given by

$$\epsilon = \epsilon_0 \begin{pmatrix} n^2 & 0 & 0 \\ 0 & n^2 & 0 \\ 0 & 0 & n^2 \end{pmatrix}, \quad (1.7)$$

where ϵ_0 is the permittivity of vacuum. In Fig. 1.3a is shown the expected index surface for this case which is the simplest one.

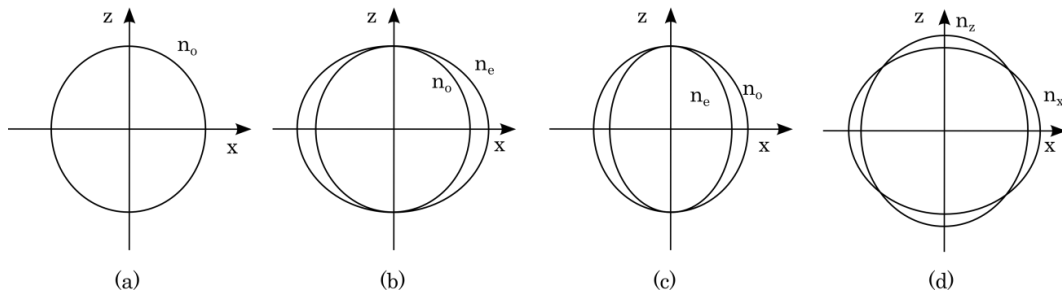


Fig. 1.3. Index surfaces for: (a) isotropic, (b) positive uniaxial, (c) negative uniaxial, and (d) biaxial medium.

There also exist the uniaxial crystals; these ones are crystals systems of tetragonal, hexagonal and trigonal kind. Their dielectric tensor is of the form:

$$\epsilon = \epsilon_0 \begin{pmatrix} n_o^2 & 0 & 0 \\ 0 & n_o^2 & 0 \\ 0 & 0 & n_e^2 \end{pmatrix}, \quad (1.8)$$

being n_o the ordinary and n_e the extraordinary refractive index. In Fig. 1.3b and 1.3c it is seen the two cases for its index surface, if $n_e > n_o$ it is called ‘positive uniaxial’ and if $n_e < n_o$ it is called ‘negative uniaxial’.

The biaxial crystals represent the most complicated case. The index surfaces for this type of crystal is shown in Fig. 1.3d. Its dielectric tensor is represented as

$$\varepsilon = \varepsilon_0 \begin{pmatrix} n_x^2 & 0 & 0 \\ 0 & n_y^2 & 0 \\ 0 & 0 & n_z^2 \end{pmatrix}. \quad (1.9)$$

1.3. Ultrasound Propagation in Anisotropic Media

The acoustic propagation is much more complicated than the light propagation, in a light wave the electromagnetic field oscillates, but in the acoustic waves are the positions of the atoms/molecules.

Strain tensor

This tensor is related to the deformation of a body. In some coordinate system the position of any point is defined by a vector \vec{r} ($x = x_1, y = x_2, z = x_3$). When the body is deformed this position changes to a new vector $r'(x'_i)$, and this displacement is given by the vector $\vec{u} = \vec{r}' - \vec{r}$;

$$u_i = x'_i - x_i, \quad (1.10)$$

which is called the displacement vector. When a body is deformed, the distance between two points will change. Let us consider two very close points with the radius vector joining the points as dx_i , the vector joining this points when deformed will be $dx'_i = dx_i + du_i$. Here the squared distance between the points is $dl^2 = dx_i^2$ before the deformation and $dl'^2 = dx_i'^2 = (dx_i + du_i)^2$ after the deformation. Now $du_i = (\partial u_i / \partial x_k) dx_k$ is substituted to rewrite

$$dl'^2 = dl^2 + 2 \frac{\partial u_i}{\partial x_k} dx_i dx_k + \frac{\partial u_i}{\partial x_k} \frac{\partial u_i}{\partial x_l} dx_k dx_l,$$

the second term on the right can be rewritten as

$$\left(\frac{\partial u_i}{\partial x_k} + \frac{\partial u_k}{\partial x_i} \right) dx_i dx_k.$$

and then, in the third term the suffixes i and l are interchanged so

$$dl'^2 = dl^2 + 2u_{ik} dx_i dx_k, \quad (1.11)$$

where the tensor u_{ik} is defined as

$$u_{ik} = \frac{1}{2} \left(\frac{\partial u_i}{\partial x_k} + \frac{\partial u_k}{\partial x_i} + \frac{\partial u_l}{\partial x_k} \frac{\partial u_l}{\partial x_k} \right). \quad (1.12)$$

u_{ik} is called the strain tensor. This tensor represents the change in the distance between two points when a body is deformed. In this case, the body is a crystal and the deformation is caused by the acoustic wave. It is easy to see, from Eq. (1.12), the symmetry of the strain tensor,

$$u_{ik} = u_{ki}. \quad (1.13)$$

Because of this symmetry the strain tensor can be diagonalized at any given point. When diagonalized at a given point, the element of length, Eq. (1.11), becomes

$$dl'^2 = (1 + 2u^{(1)}) dx_1^2 + (1 + 2u^{(2)}) dx_2^2 + (1 + 2u^{(3)}) dx_3^2,$$

where u_{ii} is the component of the diagonal of u_{ij} . From this expression is possible to see that the strain tensor is the sum of three independent directions mutually perpendicular.

1.3.1. Pure longitudinal and shear modes

Pure Longitudinal Waves

In these waves the direction of propagation of energy is in the same direction as the direction of the perturbation and only in this direction, Fig. 1.4a, generating zones of greater pressure traveling along the media.

In terms of the strain tensor, this wave is traveling in the same direction as the diagonalized strain tensor

Pure Shear Waves

Now the acoustic wave, in contrast with the longitudinal wave, makes the oscillation of the particles perpendicular to the direction of propagation, see Fig. 1.4b. Shear waves are slower than longitudinal waves and this will make them very useful for the acousto-optical applications explained later.

In terms of the strain tensor, this wave is traveling perpendicular to the direction of u_{ij} .

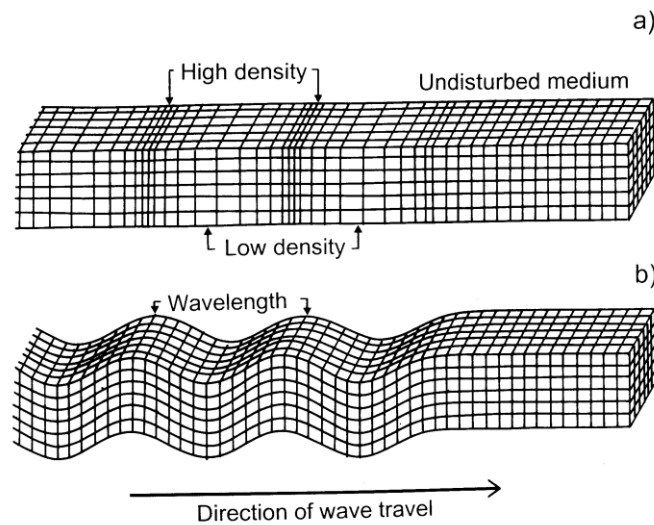


Fig. 1.4. Acoustic waves in a medium; (a) pure longitudinal wave and (b) pure shear wave.

1.4. Acousto-Optical Interactions

1.4.1. General Theory; wave vector diagrams

Suppose one acoustic field and one optic field of the same intensity, the energy of each corresponding particle is given by:

$$E = \hbar \omega, \quad (1.14)$$

where \hbar is the Planck constant divided by 2π and ω is the frequency of the particle. For the photons $\omega_L \approx 10^{14} \text{ Hz}$, and for the phonons $\omega_A \approx 10^9 \text{ Hz}$, where subindex L and A stand for light and acoustic respectively. In order to have more or less the same energy in both fields there would be 10^5 more phonons than photons, $N_L \ll N_A$ (N_L and N_A are the number of photons and

phonons respectively) so it is possible to use the given field approximation for the acoustic field.

In every physical interaction there are some measurable properties that must be conserved, for this subject, these ones are the energy and the linear momentum. In quantum mechanics, the linear momentum of a particle is:

$$p = \hbar k , \quad (1.15)$$

where k is the wave vector. So the relations that must be satisfied are:

$$\begin{aligned} \text{a) } E_L + E_A &= E_+ \\ \text{b) } \vec{p}_L + \vec{p}_A &= \vec{p}_+ \end{aligned} \quad (1.16)$$

where E stands for energy, p for momentum, the subscripts L and A are for the light and the acoustic fields, and the subscripts $+$ is for the scattered light. Using Eq. (1.14), (1.15), (1.16a) and (1.16b) is possible to arrive to two conditions:

$$\begin{aligned} \text{a) } \omega_0 + \Omega &= \omega_1 , \\ \text{b) } \vec{k}_0 + \vec{K} &= \vec{k}_1 , \end{aligned} \quad (1.17)$$

here the subscripts 0 and 1 are for the incident and the scattered light, from now on the uppercase greek letter Ω and uppercase K are for the acoustic frequency and the acoustic wave vector respectively. This conditions can be displayed in the so called “wave vector diagrams”, see Fig. 1.5. In the diagrams each vector represents the wave vector of each interacting particle and the resultant vector is the scattered photon.

These diagrams will help to visualize the two kinds of scattering that will be studied: the normal and the anomalous scattering. In the normal case, the scattered light will continue on the same surface, see Fig. 1.5, and in the anomalous case, the scattered light will “jump” to other surface, see Fig. 1.6.

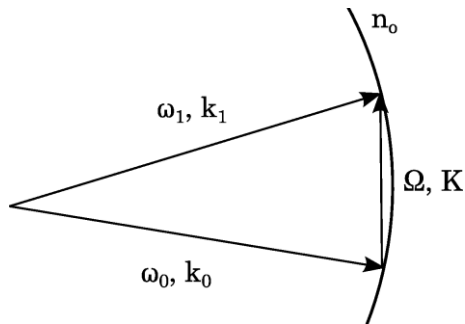


Fig. 1.5. Simple wave vector diagram of light scattering in isotropic media.

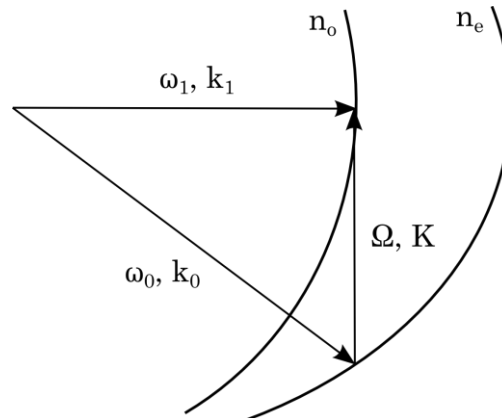


Fig. 1.6. Anomalous light scattering in an anisotropic media.

Note that the anomalous light scattering cannot occur in isotropic media because there is just one surface. On the other hand, the normal light scattering can occur on both, isotropic and anisotropic media.

1.4.2. Collinear and non-collinear interaction

Collinear Interaction

This interaction occurs when the acoustic wave and the optical wave propagate collinearly. The collinear interaction is commonly seen in anisotropic media with co-propagating waves but

there has been suggested the possibility to use counter-propagating waves to realize this interaction in a more complex phenomenon called “backward collinear acousto optic interaction” [1.3]. In Fig. 1.7, is shown the collinear interaction on anisotropic media, where the photon absorbs one phonon to change its wave vector, in so doing the light will not change its direction but its polarization state. The basic arrangement for the collinear interaction will be depicted in chapter 2.

Non-Collinear Interaction

This is the most versatile interaction because it has more degrees of freedom. Here exist an angle between the optical wave and the acoustic wave directions, Fig. 1.6. In this interaction the light can stay in the same wave vector surface by changing its direction, it even can jump to another wave vector surface and then come back to the previous surface (two phonon light scattering), see Fig. 1.8. It can occur on both, isotropic and anisotropic media (Fig. 1.5 and 1.6),

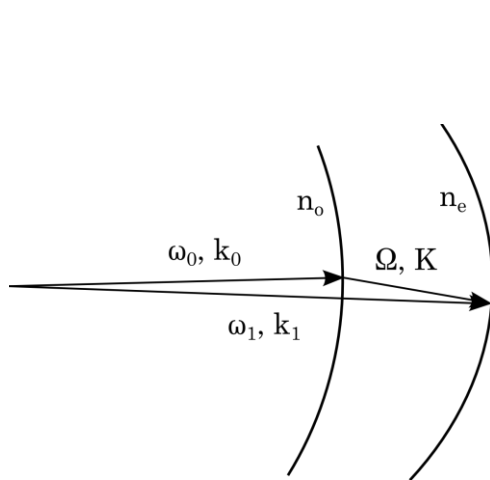


Fig. 1.7. Cuasi-collinear interaction in an anisotropic media, in the collinear interaction the three wave vectors are in the same line.

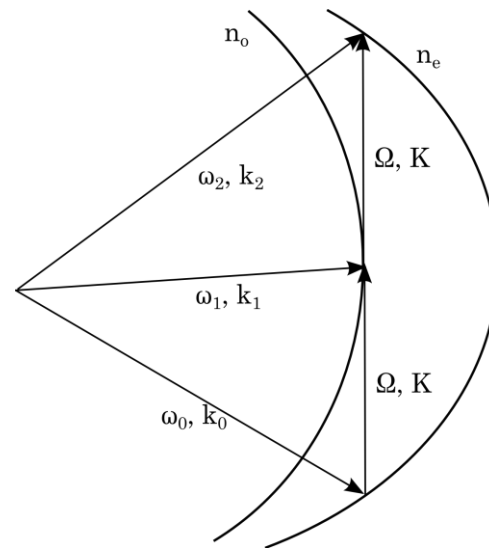


Fig 1.8. Two-phonon light scattering occurred in anisotropic media.

1.4.3. Acousto-optics in crystals

When choosing a material to work with, there are several aspects one look forward, and depending on the selected application, the material could develop great in some aspect but very bad in other ones. There is no perfect material and it is necessary to find a balance in its properties to have the best overall performance, for example; TeO_2 has a very large figure of merit M_2 , which is a good quality, but its high acoustic losses set a limit for its use in some applications.

Range of transmission

One of the most important thing to take into account is the range of transmission. This parameter tell us which light wavelengths are not (or less) absorbed by the material. Some crystal could have the best acoustic properties for some specific problem but will be useless if all the light is absorbed or even reflected.

Sound velocity

This parameter can be estimated using a simple model of an array of points of mass M separated a distance a and bounded by springs of constant C . By taking into account just the nearest neighbor interactions the sound velocity is [1.4]

$$V = \sqrt{\frac{Ca^2}{M}}. \quad (1.18)$$

Measured in cm/s , this characteristic is closely related with the figure of merit, which is described later, but also have an important role for generating the index gratings.

As it is known, the acoustic wavelength Λ , which will be directly related to the period of the phase grating, follows the relation

$$\Lambda = \frac{V}{\Omega}, \quad (1.19)$$

where V is the acoustic velocity in the material, and Ω is the acoustic frequency injected by the piezoelectric transducer. Thus, the generation of a phase gratings with more lines per centimeter will be easier in a crystal with a small acoustic velocity because the frequency needed on the piezoelectric transducer will be not too high.

Acoustic losses

For the study of this characteristic an important parameter is the ratio of the acoustic frequency Ω and the mean free path of phonons. The mean free path, in turn, is the inverse of τ , the collision time between phonons. If $\Omega\tau \gg 1$ the acoustic losses will come from the lattice phonons in thermal equilibrium. The other regime, when $\Omega\tau \ll 1$, is more interesting for this work. Here the mean free path of thermal phonons is smaller than the acoustic wavelength. The higher density regions will have greater temperature than the lower density regions and this will produce thermal conduction between them, as a result, energy from the acoustic wave will be subtracted. The previous analysis is not enough to explain the experimentally observed acoustic losses so another mechanism should exist. The Akhiezer mechanism of sound absorption was formulated to treat this phenomenon described as a phonon viscosity effect.

The attenuation α per unit path length is [1.5]:

$$\alpha \approx A \frac{\Omega^2 \tau_r}{V}, \quad (1.20)$$

where A is a constant to be determined, τ_r is the relaxation time of the thermal phonons. With this result one can say that the losses are proportional to the acoustic frequency and that low-velocity materials have higher losses than the high-velocity materials.

Acousto-optical figures of Merit

The efficiency of the light diffracted at the Bragg angle is [1.6]:

$$\eta = \frac{I_1}{I_0} = \frac{\pi^2}{2} \left(\frac{P_a/LH}{\rho V^3} \right) \left(\frac{n^3 p_{eff} L}{\lambda_0 \cos\theta} \right)^2, \quad (1.21)$$

where $P_a = LHI$ is the acoustic power in a beam of intensity I with width L and height H . Smith and Korpel in 1965 [1.6] proposed M_2 as a figure of merit for materials operating under the Bragg conditions:

$$M_2 = \frac{n^6 p_{eff}^2}{\rho V^3}, \quad (1.22)$$

where n is the refractive index, ρ is the density of the material, p_{eff} is the effective photo-elastic constant, and V is the acoustic velocity.

The efficiency is proportional to the acoustic beam width but the bandwidth is inversely proportional to the beam width. In 1966, Gordon [1.7] proposed a quantity independent of the width,

$$2\eta f_0 \Delta f = \left(\frac{n^7 p_{eff}^2}{\rho V} \right) \frac{2\pi^2}{\lambda_0^3 \cos\theta} \frac{P_a}{H}. \quad (1.23)$$

The factor

$$M_1 = \left(\frac{n^7 p_{eff}^2}{\rho V} \right) \quad (1.24)$$

is another figure of merit for materials used in modulators and deflectors.

In Eq.(1.21) and Eq.(1.23) it was assumed that the acoustic beam height is larger than the light beam diameter. Reducing the acoustic beam height to the size of the light beam and using the relation $\Lambda/L = \lambda/\varpi$ to have the same spreading angles in both optical and acoustic beams, one can get the quantity [1.8]

$$f_0 \eta = \left(\frac{n^7 p_{eff}^2}{\rho V^2} \right) \frac{\mu^2}{\lambda_0^3 \cos\theta} P_a \quad (1.25)$$

which is, in contrast with Eq.(1.21) and Eq.(1.23), independent of the sizes of the acoustic and optical beams. With this, it is possible to set

$$M_3 = \left(\frac{n^7 p_{eff}^2}{\rho V^2} \right), \quad (1.26)$$

as the third figure of merit. Each figure of merit will have certain relevance depending on the conditions of the acoustic-optical cell. For the interest of this work, the most relevant will be the figure of merit M_2 .

Elasto-optic Tensor

Also known as strain-optic tensor, is a physical quantity which relates the strain tensor and the index of refraction through the acousto-optical interaction. This interaction occurs in all states of matter and is described by

$$\Delta \eta_{ij} = \Delta \left(\frac{1}{n^2} \right)_{ij} = p_{ijkl} u_{kl}, \quad (1.27)$$

where $\Delta \eta_{ij}$ is the change in the optical impermeability tensor, u_{ij} is the strain tensor, and p_{ijkl} is the elasto-optic tensor. An acoustic wave in a crystal change the index ellipsoid of the crystal Eq. (1.1) to

$$(\eta_{ij} + p_{ijkl} u_{kl}) x_i x_j = 1. \quad (1.28)$$

Due to the symmetry of the strain and the impermeability tensor, the indices i and j as well as k and l can be permuted. The elasto-optic tensor has the same symmetry of the quadratic electro-optic tensor [1.3] so one can use the contracted indices to simplify Eq. (1.27) to

$$\Delta \left(\frac{1}{n^2} \right)_{ij} = p_{ij} u_j. \quad (1.29)$$

Photo-elastic constant

This constant can be estimated using the photo-elastic tensor p_{ijkl} , the strain tensor u_{kl} , the direction of the sound wave in the crystal \vec{d}_1 , and the direction of the interacting light \vec{d}_0 . The effective photo-elastic constant is

$$p_{eff} = \vec{d}_1 p_{ijkl} u_{kl} \vec{d}_0, \quad i, j = 1, 2, \dots, 6, \quad (1.30)$$

and using the Eqs. (1.27) and (1.28) one can rewrite Eq. (1.29) with the contracted indices to simplify the notation. Equation (1.30) then becomes

$$p_{eff} = \vec{d}_1 p_{ij} u_j \vec{d}_0. \quad (1.31)$$

This phenomenon occurs when the light propagates through a media which is under the action of acoustic waves (sound or ultrasound).

One approach for explaining this phenomenon is the next one: it is known that the sound is a perturbation which causes a difference in the pressure of the media where it travels. This perturbation produce a change in the refractive index of the material and, because of the periodicity of the acoustic wave, it creates a phase grating, see Fig. 1.9, which will be the responsible for the light to be diffracted. The parameters of this grating will be entirely determined by the intensity and the frequency of the acoustic wave.

The other approach comes from the quantum electrodynamics where the light can be treated like photons and the sound as phonons in a given field approximation, so the scattering will be caused when one photon absorbs one or more phonons and, because of the conservation of momentum, the photons will change their direction. To make it more clear, and get a deeper understanding of the phenomenon, the wave vector diagrams are introduced.

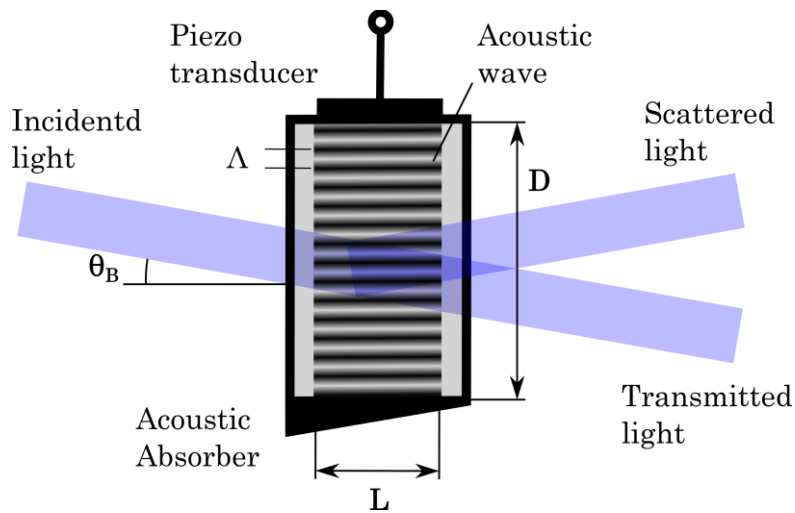


Fig. 1.9. Acoustic wave traveling in a crystalline material and generating a phase grating. L is the interaction length, D is the aperture of the cell, Λ is the acoustic wavelength, and θ_B is the Bragg angle.

Formulation of the problems

Collinear acousto-optical interaction

The first problem approached in this thesis is the continuation of the work done in my Master's degree thesis, namely, the non-linear analysis of the effect of acoustic waves of finite amplitude in the collinear acousto-optical interaction.

The non-linearity of the phenomenon will be now studied in presence of acoustical losses in a crystalline acousto-optical cell. Later, by extrapolating those results, the principally new theory of this phenomenon will be applied to predict the capabilities of an acousto-optical filter based in a more specific crystal. All the properties of the potentially usable filter will be analyzed towards the goals of contemporary demands for astrophysical spectroscopy.

Non-collinear multi-phonon light scattering

The dynamics of multi-phonon Bragg light scattering will be considered in a non-linear regime in presence of acoustical losses.

First, the theoretical approach of this phenomenon will be elaborated. Then, the search of potential materials and the specific geometry for the efficient realization of two- and three-phonon interaction will be realized.

Finally, the applications of these phenomena to acousto-optical devices with improved performances will be considered.

Transmission function of collinear acousto-optical interaction

New physical aspects of collinear acousto-optical interaction, occurred by acoustic waves of finite amplitude, are revealed and analyzed in crystalline materials exhibiting moderate linear acoustic losses. The analysis is performed in the regime of continuous traveling waves allowing specific mechanism of the acousto-optic nonlinearity. Our consideration has shown that such nonlinearity together with linear acoustic losses is able to affect the transmission function inherent in collinear interaction. In particular, the mere presence of linear acoustic losses by themselves leads to broadening the width of transmission function beginning already from very low levels of the applied acoustic power. Moreover, the transmission function exhibits a marked and quasi-periodical dependence on the applied acoustic power density; and that periodicity is governed by the linear acoustic losses. As a result, the transmission function can be significantly narrowed near isolated points at the cost of decreasing the interaction efficiency. These novelties related to collinear acousto-optical interaction accompanied by moderate linear acoustic losses have been studied and confirmed experimentally with an advanced acousto-optical cell based on calcium molybdate ($CaMoO_4$) single crystal and controlled by acoustic waves of finite amplitude.

Together with this, we explore the potentiality of using an advanced collinear $LiNbO_3$ acousto-optical filter as a dispersive element for a high-resolution optical spectrograph. This analysis is focused on weak optical signals in the blue to near-ultraviolet range accessible to ground-based facilities. We examine the phenomena affecting the filter transmission efficiency and its spectral resolution, namely, the light-induced absorption and photorefraction. The new nonlinear approach is used to determine performances of this collinear $LiNbO_3$ acousto-optical filter governed by acoustic waves of finite amplitude. The highest available spectral resolution attains $\delta\lambda = 0.15 \text{ \AA}$ at $\lambda = 370 \text{ nm}$ (the resolving power $R \sim 25000$), with an efficiency of 11%, or $\delta\lambda = 0.18 \text{ \AA}$ at $\lambda = 532 \text{ nm}$ ($R \sim 30000$), with an efficiency of 33%. A slight decrease in the spectral resolution would imply a significant increase in the transmission efficiency. Then, we have carried out proof of principle experiments with the collinear filter based on the congruent $LiNbO_3$ crystal of 6.3 cm length at $\lambda = 405$ and 440 nm to verify our analysis and estimations. Potential applications are desirable for tackling many issues in astronomy from detailed abundance analysis in a variety of targets to precise radial velocity measurement.

2.1 Introduction

Collinear acousto-optical interaction by itself had been initially revealed in the middle of the sixties in the past century by R.W. Dixon [2.1] and then, starting from the seventies has been successfully studied and exploited in various applications, among which one has to call the tunable acousto-optical filters [2.2–2.8]. The conventional analysis of this phenomenon in terms of lossless plane waves was presented in a number of classical issues [2.9, 2.10]. It allows the application of a given acoustic field approximation or, what is the same, the regime of weak coupling, when the spatial distribution of acoustic beam along a crystalline material is almost independent of the spatial distribution of light that leads to considerable theoretical and practical simplifications. In particular, a 100% efficiency of light scattering may be achieved without any effect on the acoustic beam in this case, so the above-mentioned control can be repeated many times with almost no loss of acoustic energy. Moreover, an essential difference between velocities of light and ultrasound gives us an opportunity for applying the quasi-stationary approximation to the analysis of modern problems related to collinear interaction. In the past

decades great progress has been made in acousto-optics and now it is a widely used technique in the field of data processing [2.11, 2.12]. Nevertheless, recently the existence of a new branch in studies and applications of collinear acousto-optical interaction, which is associated with acousto-optical nonlinearity, for example, in the form of three-wave coupled states, has been manifested [2.13-2.15]. That is why we believe that it is a worthwhile investment to develop these investigations, because the objects being under consideration here are closely connected with the above-mentioned nonlinearity in the regime of weak coupling. Within this consideration, we develop the exact and closed analytical model of collinear light scattering by continuous traveling acoustic waves of finite amplitude in a birefringent material with moderate linear acoustic losses. The main attention is paid to the distribution of the scattered light intensity, which can be considered as the transmission function of this process in the context of our analysis. In its turn, the width of the transmission function can be directly associated with the frequency resolution of the equivalent collinear acousto-optical filter. In so doing, we analyze the peculiarities of the effect conditioned by the acousto-optical nonlinearity, which leads to a measurable dependence of the transmission function on both the applied power density of acoustic waves of finite amplitude and the linear acoustic losses in crystalline material. Theoretically assumed novel properties of collinear acousto-optical interaction accompanied by nonlinearity and moderate linear acoustic losses are investigated experimentally with an advanced acousto-optical cell made of calcium molybdate ($CaMoO_4$) crystal and controlled by acoustic waves of finite amplitude.

2.2 Three-wave collinear interaction

Co-directional collinear acousto-optical interaction in a two-mode medium is governed by a triplet of combined partial differential equations [2.13] allowing the mismatch of wave numbers. The regime of a weak coupling [2.14, 2.15] is taken here, when two light modes are scattered by relatively slow acoustic wave of finite amplitude, but light does not affect acoustic mode. We approximate the velocities of light waves by the same value c , because practically the length of crystalline samples is less than 20 cm. Within the regime of a weak coupling, the above-noted set of equations breaks down into an equation for the complex amplitude $U(x,t)$ of acoustic wave and two combined equations for the complex amplitudes $C_0(x,t)$ and $C_1(x,t)$ of the transmitted and scattered light waves, respectively, passing along the x -axes. At the initial step, we follow the analysis developed in Ref.[2.15] for the quasi-stationary continuous-wave regime for both the incident light and the acoustic wave $U = U_0 \exp(-\alpha x) \exp(i\varphi)$, where the amplitude U_0 and the phase φ of this wave are constant, while the factor α describes the linear acoustic losses. With the boundary conditions $C_0(x=0,t) = 1$ and $C_1(x=0,t) = 0$, one can find the stationary intensities of those light waves [15].

$$\begin{aligned} \text{a) } |C_0(x)|^2 &= \frac{\eta^2}{\sigma^2 + \eta^2} + \frac{\sigma^2}{\sigma^2 + \eta^2} \cos^2[G(x) - G(0)] , \\ \text{b) } |C_1(x)|^2 &= \frac{q_0}{q_1} \frac{\sigma^2}{\sigma^2 + \eta^2} \sin^2[G(x) - G(0)] . \end{aligned} \quad (2.1)$$

$$G(x) = \frac{1}{\alpha} \left[-\sqrt{\eta^2 + \sigma^2 \exp(-2\alpha x)} + \eta \ln \left\{ \frac{2\alpha}{\eta^2} \left[\eta \exp(\alpha x) + \sqrt{\sigma^2 + \eta^2 \exp(2\alpha x)} \right] \right\} \right]. \quad (2.2)$$

Here, $q_{0,1}$ are the constants of interaction for each light wave, 2η is the mismatch of wave numbers inherent in the interacting waves (see physical details in section 3). The parameter $q_0 q_1 U_0^2 = \sigma^2$ describes both the material properties and the acoustic power. The function $G(x)$ is used to shorten the Eqs.(2.1). When $\eta = 0$, one yields $G(x) = -\alpha^{-1} \sigma \exp(-\alpha x)$, so that Eq.(2.1b) takes the form [2.15]

$$|C_1(x)|^2 = \frac{q_0}{q_l} \sin^2 \left\{ \frac{\sigma}{\alpha} [1 - \exp(-\alpha x)] \right\}. \quad (2.3)$$

Now, unlike Ref.[2.15] oriented to localizing the dissipative coupled states, the conditions of extrema efficiencies are applied to light scattering. Each extrema can be reached at $\eta=0$, so that the positions of extrema are conditioned by the losses α and the parameter σ , see Eq.(2.3). The extrema in the scattered light distribution are given by

$$\begin{aligned} \text{a) Maxima: } G(x) - G(0) &= \pi \left(N + \frac{1}{2} \right), \quad N = 0, 1, 2, \dots; \\ \text{b) Zeros: } G(x) - G(0) &= \pi M, \quad M = 1, 2, 3, \dots, \end{aligned} \quad (2.4)$$

where N and M are the numbers of maxima and zeros, respectively. These conditions lead to the equalities

$$\begin{aligned} \text{a) } \frac{\sigma}{\alpha} [1 - \exp(-\alpha x)] &= \pi \left(N + \frac{1}{2} \right), \\ \text{b) } \frac{\sigma}{\alpha} [1 - \exp(-\alpha x)] &= \pi M. \end{aligned} \quad (2.5)$$

Because the left hand sides of these formulas are limited, one can find that

$$\begin{aligned} \text{a) } N &\leq \frac{\sigma}{\alpha \pi} [1 - \exp(-\alpha x)] - \frac{1}{2}, \\ \text{b) } M &\leq \frac{\sigma}{\alpha \pi} [1 - \exp(-\alpha x)], \end{aligned} \quad (2.6)$$

i.e. the numbers N and M are restricted. Moreover, it is seen that $N \leq \frac{\sigma}{\alpha \pi} - \frac{1}{2}$ and

$M \leq \frac{\sigma}{\alpha \pi}$ in the limit of $x \rightarrow \infty$.

At first, let us consider the maxima. Eq.(2.3) can be illustrated by the following 2D-plot, which represents a few cross-sections of the right hand side of Eq.(2.5a) by planes $N=0,1,2$, see Fig. 2.1. The unit-valued maxima of Eq.(2.3) under condition imposed by Eq.(2.4a) are placed at the distances

$$X_N = -\alpha^{-1} \cdot \ln \left[1 - \frac{\alpha \pi}{\sigma} \left(N + \frac{1}{2} \right) \right]. \quad (2.7)$$

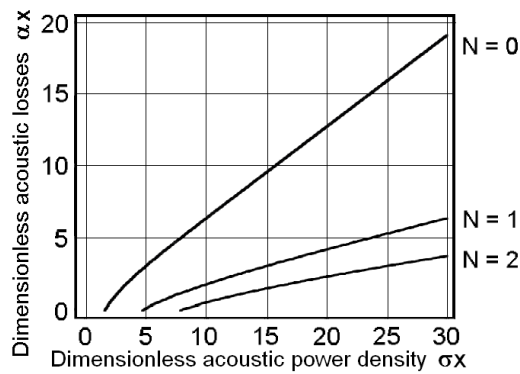


Fig. 2.1. A 2D-plot on the plane $(\alpha x, \sigma x)$ with lines corresponding to $N=0,1,2$

For example, (1) when $\alpha = 0.1 \text{ cm}^{-1}$ and $\sigma = 0.5 \text{ cm}^{-1}$, one arrives at $N \leq 1$ with $X_0 = 3.768 \text{ cm}$ and $X_1 = 28.55 \text{ cm}$; (2) when $\alpha = 0.1 \text{ cm}^{-1}$ and $\sigma = 1 \text{ cm}^{-1}$, one yields $N \leq 2$, wherein $X_0 = 1.709 \text{ cm}$, $X_1 = 6.372 \text{ cm}$, and $X_2 = 15.39 \text{ cm}$, see Fig.2.2; (3) while when $\alpha = 0.1 \text{ cm}^{-1}$ and $\sigma = 2 \text{ cm}^{-1}$, one has $N \leq 5$ with $X_0 = 0.818 \text{ cm}$, $X_1 = 2.687 \text{ cm}$, $X_2 = 4.987 \text{ cm}$, $X_3 = 7.980 \text{ cm}$, $X_4 = 12.271 \text{ cm}$, and $X_5 = 19.964 \text{ cm}$. Together with this in the medium with much lower acoustical losses, let say for instance with $\alpha = 0.01 \text{ cm}^{-1}$, one can find $N \leq 15$ for $\sigma = 0.5 \text{ cm}^{-1}$ and $N \leq 31$ for $\sigma = 1 \text{ cm}^{-1}$. Together with this, the graphical solution to Eq.(5a) gives another illustration for positions of the unit-valued maxima. For $N = 0$, these positions are depicted by intersections of the curve $1 - \exp(-\alpha x)$ with horizontal lines $\alpha\pi/(2\sigma)$ in Fig. 2.3, where $\alpha = 0.1 \text{ cm}^{-1}$.

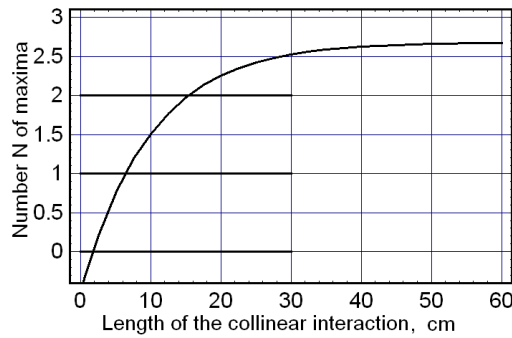


Fig. 2.2. Restricting the number N of unit valued maxima; the particular case of $\alpha = 0.1 \text{ cm}^{-1}$, $\sigma = 1 \text{ cm}^{-1}$ and $N \leq 2$ is shown.

At this step, one can analyze the zeros in the light intensity $|C_1|^2$ distribution. In so doing, Eq.(2.3) can be illustrated by a $2D$ plot, which represents a few cross-sections of the right hand side of Eq.(2.5b) by planes $M = 1, 2, 3, \dots$, which is quite similar to Fig.1. The zero-intensity points are placed at the distances

$$Z_M = -\alpha^{-1} \cdot \ln \left[1 - \frac{\alpha \pi}{\sigma} M \right]. \quad (2.8)$$

For example, (1) when $\alpha = 0.1 \text{ cm}^{-1}$ and $\sigma = 0.5 \text{ cm}^{-1}$, one arrives at $0 < M \leq 1$ with $Z_1 = 9.89 \text{ cm}$; (2) when $\alpha = 0.1 \text{ cm}^{-1}$ and $\sigma = 1 \text{ cm}^{-1}$, one yields $0 < M \leq 3$, wherein $Z_1 = 3.77 \text{ cm}$, $Z_2 = 9.89 \text{ cm}$, and $Z_3 = 28.47 \text{ cm}$, see Fig. 2.4; (3) while when $\alpha = 0.1 \text{ cm}^{-1}$ and $\sigma = 2 \text{ cm}^{-1}$, one has $0 < M \leq 6$ with $Z_1 = 1.708 \text{ cm}$, $Z_2 = 3.77 \text{ cm}$, $Z_3 = 6.386 \text{ cm}$, $Z_4 = 9.89 \text{ cm}$, $Z_5 = 15.37 \text{ cm}$, and $Z_6 = 28.47 \text{ cm}$.

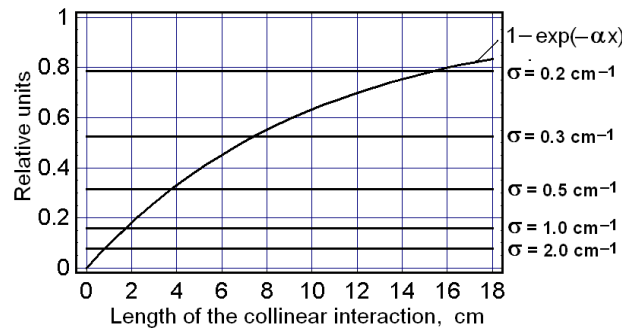


Fig.2.3. Graphical solution to Eq.(2.5a); positions for the unit-valued maxima as function of collinear interaction length and σ is a parameter for $N = 0$ and $\alpha = 0.1 \text{ cm}^{-1}$.

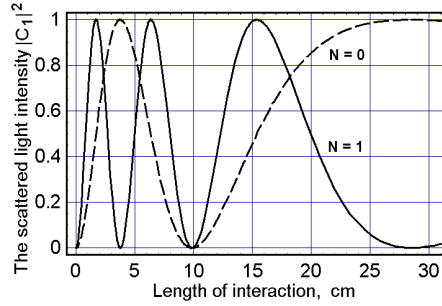


Fig. 2.4. The normalized scattered light distributions versus the dimensional length of interaction with $\alpha = 0.1 \text{ cm}^{-1}$: the dashed line is for $\sigma = 0.5 \text{ cm}^{-1}$ and solid line is for $\sigma = 1 \text{ cm}^{-1}$

Finally, Eq.(2.3) can be directly exploited for illustrating the light intensity dependences under consideration. In the above-noted approximation $q_0/q_1 \approx 1$ one can obtain the plots presented in Fig.4. The extrema of each individual curve are coincided with the calculated above values for X_N and Z_M , see Eqs.(2.7) and (2.8). At this step, one has to remind about approximate character of the analysis developed in Ref. [2.15] and to note that Eq. (2.2) as well as Eq. (2.7) and (2.8) are not valid for infinite distances.

2.3 Efficiency of collinear interaction in different materials

Now let us consider a few practically useful estimations related to experimental observation of the collinear acousto-optical interaction with linear acoustic losses in a birefringent cell made of a calcium molybdate (CaMoO_4) single crystal. In this particular case, one can observe only anomalous process of light scattering, so that the parameters $q_{0,1}$ are described [2.9] by

$$q_{0,1} = \frac{|\vec{k}_{0,1}|}{4n_{0,1}^2} (\vec{e}_0 \Delta \varepsilon \vec{e}_1). \quad (2.9)$$

Here, $n_{0,1}$ are the refractive indices for the interacting light waves, $|\vec{k}_{0,1}| = 2\pi n_{0,1}/\lambda$, λ is the light wavelength in a vacuum, and the last term in brackets, describing the efficiency of interaction, is subject to find. This term includes the eigen-orts $\vec{e}_{0,1}$ of polarizations for the incident and scattered light beams as well as the tensor $\Delta \varepsilon$ of perturbations of the dielectric permittivity under action of the acoustic wave in a medium. To estimate the efficiency of collinear acousto-optical interaction in a calcium molybdate cell, i.e. to find the contribution of brackets to Eq.(2.9), we consider the above-mentioned geometry of interaction including the shear acoustic wave with the wave normal ort \vec{m} is passing along the [100]-axis, so that $\vec{k}_{0,1} = \vec{m} |\vec{k}_{0,1}|$; while its vector \vec{u} of the transversal elastic displacements is oriented along the [001]-axis in that crystalline material, i.e. $\vec{m} = [1,0,0]$ and $\vec{u} = [0,0,1]$. Thus, one can write the deformation tensor γ and the unperturbed dielectric permittivity tensor ε in the main crystallographic axes as

$$\text{a) } \gamma = \frac{\gamma_0}{2} (\vec{u} \cdot \vec{m} + \vec{m} \cdot \vec{u}) = \frac{\gamma_0}{2} \begin{pmatrix} 0 & 0 & 1 \\ 0 & 0 & 0 \\ 1 & 0 & 0 \end{pmatrix}, \quad \text{b) } \varepsilon = \begin{pmatrix} \varepsilon_0 & 0 & 0 \\ 0 & \varepsilon_0 & 0 \\ 0 & 0 & \varepsilon_e \end{pmatrix}. \quad (2.10)$$

Here, γ_0 is the amplitude of the shear deformation, while $\varepsilon_0 = n_0^2$ and $\varepsilon_e = n_e^2$ are the eigenvalues of the unperturbed dielectric permittivity tensor ε . Now, the tensor γ of the second rank with the components γ_{kl} ($k, l = 1, 2, 3$) can be converted into a 6-dimension vector

$\bar{\gamma} = \gamma_0(0,0,0,0,1,0)$ with the components $\bar{\gamma}_\mu$ ($\mu=1, \dots, 6$) using the standard procedure [2.14], which includes re-notating $\bar{\gamma}_\mu = \gamma_{kk}$ ($\mu=1, 2, 3$) and $\bar{\gamma}_\mu = 2\gamma_{kl}$ ($k \neq l, \mu=4, 5, 6$). If now one will use the same procedure [2.14] and take the photo-elastic tensor p of the fourth rank for a calcium molybdate single crystal in the form of a 6×6 matrix \hat{p} , it will be allowed first to construct and to calculate the product $\hat{p}\bar{\gamma} = \gamma_0(0,0,0, p_{45}, p_{44}, 0)$, and then to convert the result back to the form of a standard tensor ($p\gamma$) of the second rank.

The next step of our analysis is connected with finding the dielectric permittivity perturbations tensor $\Delta\varepsilon$, whose components can be written as $\Delta\varepsilon_{ij} = \varepsilon_{im}\varepsilon_{nj} p_{mnkl} \gamma_{kl}$ [9]. In the particular case of a $CaMoO_4$ -crystal whose point symmetry group is $4/m$, one can write [2.14 – 2.16]:

$$p_{\lambda\mu} = \begin{pmatrix} p_{11} & p_{12} & p_{13} & 0 & 0 & p_{16} \\ p_{12} & p_{11} & p_{13} & 0 & 0 & -p_{16} \\ p_{31} & p_{31} & p_{33} & 0 & 0 & 0 \\ 0 & 0 & 0 & p_{44} & p_{45} & 0 \\ 0 & 0 & 0 & -p_{45} & p_{44} & 0 \\ p_{61} & -p_{61} & 0 & 0 & 0 & p_{66} \end{pmatrix} = \begin{pmatrix} 0.17 & -0.15 & -0.08 & 0 & 0 & 0.03 \\ -0.15 & 0.17 & -0.08 & 0 & 0 & -0.03 \\ 0.10 & 0.10 & 0.08 & 0 & 0 & 0 \\ 0 & 0 & 0 & 0.06 & 0.06 & 0 \\ 0 & 0 & 0 & -0.06 & 0.06 & 0 \\ 0.10 & -0.10 & 0 & 0 & 0 & 0.03 \end{pmatrix}. \quad (2.11)$$

The result of calculating has the form

$$\Delta\varepsilon = \gamma_0 \varepsilon_0 \varepsilon_e \begin{pmatrix} 0 & 0 & p_{44} \\ 0 & 0 & p_{45} \\ p_{44} & p_{45} & 0 \end{pmatrix}. \quad (2.12)$$

Now, we take into account the orts $\vec{e}_{0,1}$ of polarization for the incident and scattered light waves. When the wave vectors of these light waves are collinear to the wave normal ort \vec{m} for the acoustic wave and, of course, to the [100]-axis in calcium molybdate crystal, the eigen-orts $\vec{e}_{0,1}$, of light polarizations should be oriented, as it directly follows from Eq.(2.10b), along the [010] and [001] axes, so that one can take, for example, $\vec{e}_0 = [0,1,0]$ and $\vec{e}_1 = [0,0,1]$ with $n_0 = n_o$ and $n_1 = n_e$. As a result, one can obtain the contribution of brackets to Eq.(2.9) as

$$\vec{e}_0 \Delta\varepsilon \vec{e}_1 = \vec{e}_1 \Delta\varepsilon \vec{e}_0 = \gamma_0 \varepsilon_0 \varepsilon_e p_{45}. \quad (2.13)$$

In so doing, one can find that $q_{0,1} = \pi(2\lambda)^{-1} n_{e,o} \gamma_0 n_{o,e}^2 p_{45}$. One can see now that the difference between q_0 and q_1 is rather small, because $q_0/q_1 = n_e/n_o$. Then, because the amplitude of deformation can be explained as $\gamma_0 = \sqrt{2P/(\rho V^3)}$, where P is the acoustic power density, one can finally obtain

$$\text{a) } q_0 = \frac{\pi}{\lambda} \sqrt{\frac{P}{2} \left(\frac{n_e^2 n_o^4 p_{45}^2}{\rho V^3} \right)}, \quad \text{b) } q_1 = \frac{\pi}{\lambda} \sqrt{\frac{P}{2} \left(\frac{n_o^2 n_e^4 p_{45}^2}{\rho V^3} \right)}. \quad (2.14)$$

It should be noted that the factors taken in brackets in Eqs.(2.14) represent the figure of acousto-optical merit peculiar to estimating the efficiency of crystalline materials in acousto-optics [2.17], while the refractive indices are slightly dispersive in behavior, see Table 2.1.

Table 2.1. Dispersion of the main refractive indices n_e and n_o in the calcium molybdate crystal [2.18].

λ , nm	500	600	700	800	900	1000
n_e	2.0239	1.9983	1.9843	1.9781	1.9705	1.9658
n_o	2.0116	1.9884	1.9775	1.9683	1.9634	1.9597

At this step, we are ready to perform a few numerical estimations inherent in the collinear interaction under consideration at the light wavelength of $\lambda = 671 \text{ nm}$ in the CaMoO_4 -crystalline cell. Taking the material density $\rho = 4.34 \text{ g/cm}^3$, acoustic velocity $V = 2.95 \cdot 10^5 \text{ cm/s}$, $p_{45} = 0.06$, $n_e = 1.9889$, $n_o = 1.9811$, and $\Delta n = 0.0078$ at the chosen light wavelength [2.18], one can calculate the figure of acousto-optical merit $M_2 = n_o^3 n_e^3 p^2 (\rho V^3)^{-1}$, where p is an effective photo-elastic constant, and ρ is the crystal density, as $M_2 \approx 1.977 \cdot 10^{-18} (\text{s}^3/\text{g})$ with an accuracy of about 1%.

2.4 Resolution of collinear interaction

2.4.1 Traditional approach

It is well known that the spectral resolution $\delta\lambda$ and the frequency resolution δf of collinear acousto-optical filters are usually estimated as $|\delta\lambda| = (\lambda/f_0) \delta f$ and $\delta f = V/L$, where f_0 and V are the carrier frequency and velocity of acoustic wave; L is the longitudinal aperture of filter, i.e. the length of acousto-optical interaction. It is obviously seen that these formulas do not include potential influence of the initial acoustic power density on the resolution.

At first, let us consider the lossless medium in the case of infinitely small signals, i.e. with $\sigma \rightarrow 0$. In so doing, one can estimate $G(x) = \eta x$, $G(0) = 0$, and write

$$|C_1(x)|^2 = \left(\frac{q_0 (\sigma x)^2}{q_1} \right) \cdot \frac{\sin^2(\eta x)}{(\eta x)^2}, \quad (2.15)$$

where the distance x can be considered as a parameter. Historically, estimating the resolution is connected with the well-known Rayleigh criterion, which predicts in fact separating a pair of the neighboring $(\sin u/u)^2$ -shaped distributions at the intensity level of $v \approx 0.4055$. This is exactly the case of Eq.(2.15), and one has to resolve the transcendent algebraic equation $\sin(\eta x) = v^{1/2}(\eta x) \approx 0.6368(\eta x)$. The first (both positive and negative) solutions to this algebraic equations are $\eta_{(\pm)} x = \pm \pi/2$. They lead to the bandwidth from $\eta_{(-)} x = -\pi/2$ to $\eta_{(+)} x = +\pi/2$, i.e. to the full bandwidth at the intensity level: $v \approx 0.4055$ $\Delta \eta x = \eta_{(-)} x + \eta_{(+)} x = |-\pi/2| + |+\pi/2| = \pi$. Together with this a one-side mismatch η had been previously determined as $\eta = \Delta K/2 = \pi \delta f/V$, so that in the more detailed form $\eta_{(\pm)} = \pi \delta f_{(\pm)}/V$ (where $\delta f_{(\pm)}$ are the corresponding one-side frequency deviations) and consequently, the total deviation of the mismatch is given by $\Delta \eta = \eta_{(-)} + \eta_{(+)} = \pi(\delta f_{(-)} + \delta f_{(+)})/V = \pi \delta f/V$. Combining the expressions, which include $\Delta \eta$, one arrives at the above-noted formula $\delta f = V/x$, where one can undoubtedly put $x = L$.

Thus, one can see that full width of the main lobe inherent in a $(\sin u/u)^2$ – shaped distribution at the intensity level $\nu \approx 0.4055$ gives the “standard” determination of the frequency resolution in acousto-optics, which is conditioned by the limit $\sigma \rightarrow 0$.

2.4.2 Medium without acoustical losses

Now, let us consider the lossless case with signals of the finite amplitude when $\sigma \neq 0$. Because of $G(x) = x \sqrt{\sigma^2 + \eta^2}$ and $G(0) = 0$, one can write

$$|C_1|^2 = \left(\frac{q_0}{q_1} \right) \frac{(\sigma x)^2}{(\sigma x)^2 + (\eta x)^2} \sin^2 \left[\sqrt{(\sigma x)^2 + (\eta x)^2} \right]. \quad (2.16)$$

To estimate the frequency resolution at the above-noted intensity level $\nu \approx 0.4055$ Eq.(2.16) has to be normalized as

$$\frac{|C_1|^2}{|C_1(\eta=0)|^2} = \left[\frac{(\sigma x)^2}{(\sigma x)^2 + (\eta x)^2} \right] \cdot \frac{\sin^2 \left[\sqrt{(\sigma x)^2 + (\eta x)^2} \right]}{\sin^2(\sigma x)}. \quad (2.17)$$

The 3D-plots inherent in these distributions are presented in Fig.2.5 for the scattered light intensity $|C_1(x)|^2$ in absolute units, see Eq.(2.16), and for the normalized intensity from Eq.(2.17) in practically reasonable approximation $q_0/q_1 \approx 1$. Figure 2.5a gets the interval $0 \leq \sigma x < 3\pi$ and illustrates a regular structure in absolute units, which exhibits reaching a sequence of unit-valued maxima along the line $\eta x = 0$ with a dimensionless period $\sigma x = \pi$. Figure 2.5b reflects the normalized distribution on the smaller interval $0 \leq \sigma x \leq \pi$ and includes the level $\nu \approx 0.4055$ -plane for estimating the width in terms of a one-side dimensionless mismatch ηx .

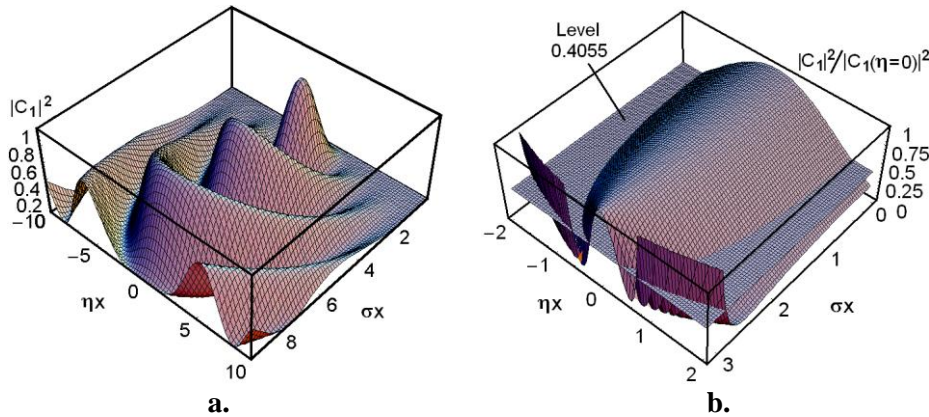


Fig. 2.5. The 3D-plots of the scattered light intensity profile with $q_0/q_1 \approx 1$: (a) for the absolute values on the interval $0 \leq \sigma x < 3\pi$ and (b) for the normalized distribution on the interval $0 \leq \sigma x \leq \pi$.

A set of 2D-plots for the scattered light intensity $|C_1[(\sigma x), (\eta x)]|^2$ is presented in Figs.2.6 in the absolute form for the range of products $1.0 \leq \sigma x < \pi$ in the same approximation $q_0/q_1 \approx 1$. These 2D-plots illustrate in details the dynamics of evolving the distributions step by step and confirm that one can expect narrowing the normalized intensity profile noted by Eq.(2.17) with $\sigma x \rightarrow \pi$ from smaller values as depicted in Fig.2.5b.

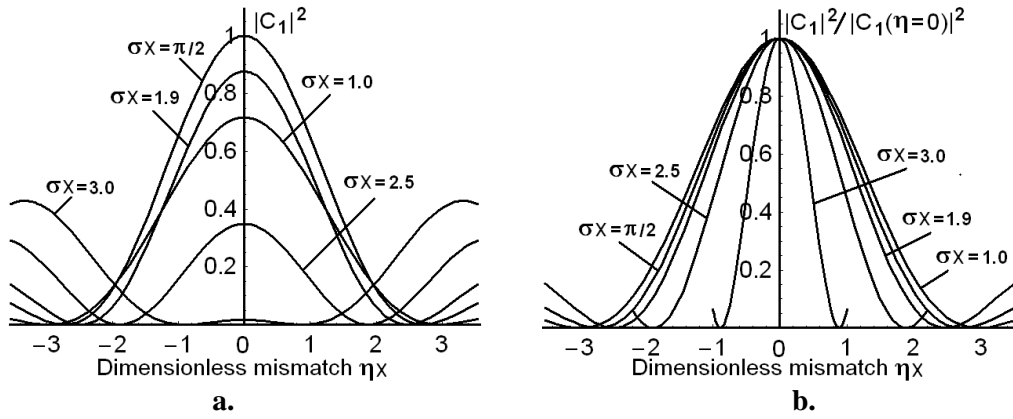


Fig. 2.6. The 2D-plots $|C_1[(\sigma x), (\eta x)]|^2$ for the products $1.0 \leq \sigma x < \pi$ with $q_0/q_1 \approx 1$:
 (a) for the absolute values and (b) after normalization by the zero magnitudes.

With $1.0 \leq \sigma x < \pi$, estimations at the above-chosen intensity level $v \approx 0.4055$ give one-side mismatches $\eta x(\sigma x = 1.0) = 1.511$, $\eta x(\sigma x = \pi/2) = 1.414$, $\eta x(\sigma x = 2.0) = 1.292$, $\eta x(\sigma x = 2.5) = 1.059$, and $\eta x(\sigma x = 3.0) = 0.524$, see Fig.2.6b, which lead to the corresponding full bandwidths $\Delta \eta x(\sigma x) = 2\eta x(\sigma x)$. These numbers should be compared with the previously obtained a one-side mismatch estimation $\eta x(\sigma x \rightarrow 0) = \pi/2 \approx 1.5708$ and the full bandwidth $\Delta \eta x(\sigma x \rightarrow 0) = \pi$, corresponding to relatively low efficiency of light scattering in the regime of a given incident optical field approximation. One can see from these estimations and Fig.6 that the contribution from acoustic wave of the finite amplitude narrows the profiles, and the most efficient regime, providing theoretically 100% efficiency of light scattering, can be achieved with $\sigma x = \pi/2$, see Fig.2.6a, when the profile width will be about 10% better than in the case of a low-power non-optical wave. Growing the product σx makes it possible to narrow profile for more, but at the cost of decreasing the efficiency significantly. Nevertheless, a desirable balance between the contour width and efficiency can be found here, for instance in vicinity of $\sigma x \cong 2.0$, if the case requires.

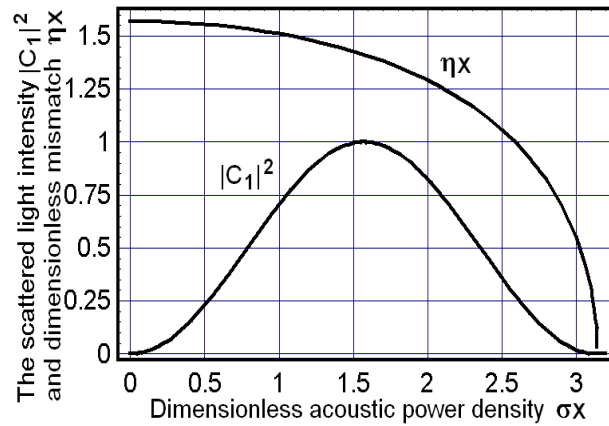


Fig.2. 7. The light intensity $|C_1(x)|^2$ and a one-side dimensionless mismatch ηx versus the product σx .

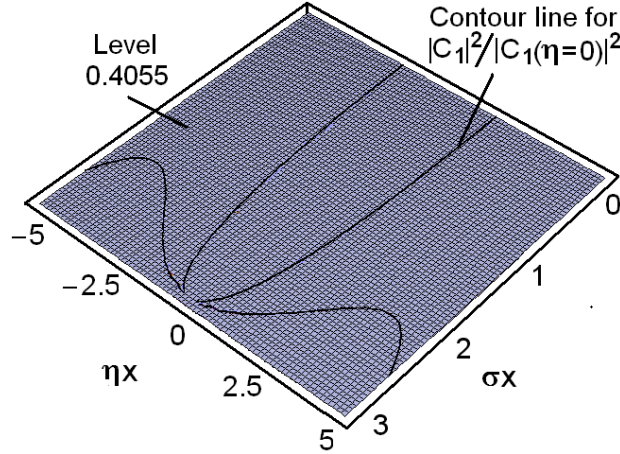


Fig. 2.8. A 2D-contour for the normalized light intensity on the plane $[(\sigma x), (\eta x)]$ on the interval $0 \leq \sigma x \leq \pi$.

Figure 2.8 represent a 2D-contour plot for the normalized light intensity on the plane $[(\sigma x), (\eta x)]$. The contour lies on the interval $0 \leq \sigma x \leq \pi$ and demonstrates the tendency of squeezing the normalized light intensity profile with growing the product σx . As a result, one can see that profile width at $\sigma x \rightarrow \pi$ is a few times narrower than initial one with $\sigma x \rightarrow 0$, i.e. squeezing of the transmission function is observed.

Another set of 2D-plots for the normalized scattered light intensity $|C_1[(\sigma x), (\eta x)]|^2 \cdot |C_1(\eta=0)|^{-2}$ is presented in Fig.2.9 for the range of products $\pi < \sigma x < 2\pi$. This range of products σx has not been shown in Fig.2.5b. It is clearly seen from Fig.2.9 that the profile width becomes dramatically gained within this range. The most effective case when $|C_1(\eta=0)|^2 = 1$ is reached at $\sigma x = 3\pi/2$, see Fig.2.9a, but it gives already the profile one-side width $\eta x(\sigma x = 3\pi/2) \approx 2.5$ at the level 0.4055, which is definitely wider than the corresponding profile in the range of products $\pi < \sigma x < 2\pi$.

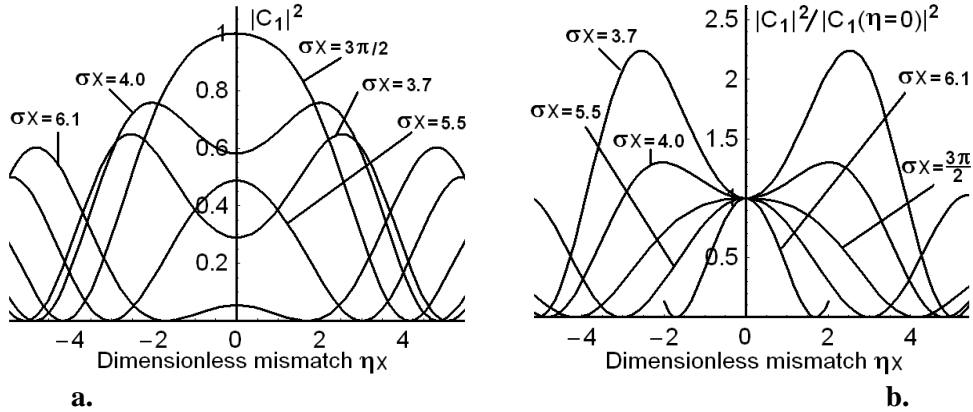


Fig. 2.9. The 2D-plots $|C_1[(\sigma x), (\eta x)]|^2$ for the products $\pi < \sigma x < 2\pi$ with $q_0/q_1 \approx 1$: (a) for the absolute values and (b) after normalization by the zero magnitudes.

Figure 2.10 demonstrates the general tendency to repeat squeezing the profile $|C_1[(\sigma x), (\eta x)]|^2$ periodically, although only the interval $\pi \leq \sigma x < 3\pi$ is depicted here. However, the presented 2D-contour plot shows clearly that each next period exhibits a wider profile in the vicinity of the points $\sigma x \rightarrow (\pi/2) + m\pi$, $m=0,1,2,3, \dots$ related to maximal efficiency of light scattering as well as at the points $\sigma x \rightarrow (m+1)\pi$ of maximal squeezing at this period with the chosen number m . It should be noted that the dynamics of profile transformation within each particular period can be imagined in certain respects by analogy with

the plots presented in Figs.2.6 and 2.9 with obvious corrections, of course, for scaling along the ηx -axis. Thus, Fig.2.10 makes it possible to conclude that increasing the dimensionless product σx as far as the involved number m grows does not promise any additional squeezing the profile in comparison with the case of $m=0$.

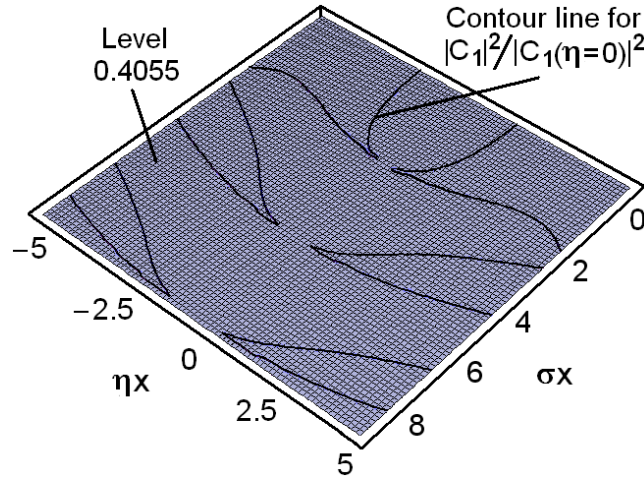


Fig. 2.10. A 2D-contour plot for the normalized light intensity on the plane $[(\sigma x), (\eta x)]$ on the interval $0 \leq \sigma x < 3\pi$.

2.4.3 Medium with acoustical losses

It is well known [2.2-2.7] that the transmission function width (TFW) δf of collinear acousto-optical interaction is usually estimated by $\delta f = V/L$, where V is the acoustic wave velocity and L is the longitudinal aperture of crystal, i.e. the length of acousto-optical interaction. It is seen that this formula does not include both the acoustic attenuation and the potential influence of initial acoustic power density on the TFW.

At first, let us consider Eqs.(2.4b) and (2.5b) in the lossless medium with $\alpha=0$ and in the case of infinitely small signals, i.e. with $\sigma \rightarrow 0$. In so doing, one can estimate $G(x, \alpha=0) = \eta x$, $G(0, \alpha=0) = 0$, and write

$$|C_1(x)|^2 = \left(\frac{q_0 (\sigma x)^2}{q_1} \right) \cdot \frac{\sin^2(\eta x)}{(\eta x)^2}, \quad (2.18)$$

where the distance x can be considered as a parameter. Historically, determination of the taken alone TFW for a collinear acousto-optical filter is connected with estimating its full-width at half maximum (FWHM), see for instance [2.2, 2.3]. However, within resolving dense sets of neighboring lines in optical spectra, the widely used Rayleigh criterion could be preferable and it will be exploited. The choice of a concrete criterion does not look critically important as the more that one of them can be converted into the other one by the factor ~ 0.886 for the contour in Eq.(2.18). The Rayleigh criterion predicts in fact separating a pair of the neighboring $(\sin u/u)^2$ -shaped distributions at the intensity level of $v \approx 0.405$. This is exactly the case of Eq.(18), and one has to resolve the transcendent algebraic equation $\sin(\eta x) = v^{1/2}(\eta x) \approx 0.6368(\eta x)$. The first (both positive and negative) solutions to this algebraic equation are $\eta_{(\pm)} x = \pm \pi/2$. They lead to the bandwidth from $\eta_{(-)} x = -\pi/2$ to $\eta_{(+)} x = +\pi/2$, i.e. to the full bandwidth at the intensity level: $v \approx 0.405$, which is given by $\Delta \eta x = \eta_{(-)} x + \eta_{(+)} x = |-\pi/2| + |+\pi/2| = \pi$. Together with this a one-side mismatch η had been previously [see Eqs.(2.1)] determined as $\eta = \Delta K/2 = \pi \delta f/V$, so that in the more detailed form $\eta_{(\pm)} = \pi \delta f_{(\pm)}/V$ (where $\delta f_{(\pm)}$ are the corresponding one-side frequency deviations) and

consequently, the total deviation of the mismatch is given by $\Delta\eta = \eta_{(-)} + \eta_{(+)} = \pi(\delta f_{(-)} + \delta f_{(+)})/V = \pi\delta f/V$. Combining the expressions, which include $\Delta\eta$, one arrives at the above-noted formula $\delta f = V/x$, where one can undoubtedly put $x=L$. Thus, one can see that full width of the main lobe inherent in the $(\sin u/u)^2$ – distribution at the intensity level $v \approx 0.405$ gives the “standard” determination of the frequency resolution in acousto-optics or the TFW, which is conditioned by the limit $\sigma \rightarrow 0$. In the case of a moderately lossy medium, i.e. with $\alpha \neq 0$ and $\sigma \rightarrow 0$, Eqs.(2.2) give us

$$\begin{aligned} \text{a) } G(x, \alpha \neq 0) &= \alpha^{-1} \eta [\alpha x - 1 + \ln(4\alpha\eta^{-1})], \\ \text{b) } G(0, \alpha \neq 0) &= \alpha^{-1} \eta [-1 + \ln(4\alpha\eta^{-1})]. \end{aligned} \quad (2.19)$$

As a result, $G(x, \alpha \neq 0) - G(0, \alpha \neq 0) = \eta x$ as well and one arrives at Eq.(2.18). Consequently, the traditional conclusion lies in the fact that under condition of infinitely small signals, i.e. with $\sigma \rightarrow 0$, the acoustic losses do not affect the TFW independently on the concrete level of those linear losses.

Then, one can naturally consider Eq.(2.1b) in the case of $\alpha \neq 0$ under acting the signals of finite amplitude when $\sigma \neq 0$. The 3D-plots peculiar to these distributions are presented in Fig.2.11 for the scattered light intensity $|C_1(x)|^2$ in terms of the absolute units in practically reasonable approximation $q_0/q_1 \approx 1$ on the interval $0 \leq \sigma x \leq 3\pi$. Regular structures exhibit reaching a sequence of unit-valued maxima along the line $\eta x = 0$ within various dimensionless σx – periods depending on the product $\alpha x \neq 0$. In fact, one can consider the result of growing the product αx as a scaling along the σx -axis, which leads to a shift of unit-valued maxima in the larger σx – direction.

Now, the TFW can be considered in a medium with moderate acoustical losses under the requirement of maximal efficiency. In the case of a moderate acoustical losses, Eqs.(2.1) and (2.2) should be exploited in their original forms as well with $\alpha \neq 0$ and $\sigma \neq 0$. The above-formulated requirement of maximal efficiency of light scattering leads to Eqs.(2.4) and (2.5) as well as to Figs.2.1,2.2. Numerical simulations for 2D-profiles of the intensities $|C_1(x)|^2$ with $q_0/q_1 \approx 1$ have been performed in three cases of moderate acoustical losses, namely: (1) $\alpha = 0.1 \text{ cm}^{-1}$, $\sigma = 0.5 \text{ cm}^{-1}$ (with $X_0 = 3.768 \text{ cm}$ and $X_1 = 28.55 \text{ cm}$); and (2) $\alpha = 0.1 \text{ cm}^{-1}$, $\sigma = 1 \text{ cm}^{-1}$ (with $X_0 = 1.709 \text{ cm}$, $X_1 = 6.372 \text{ cm}$, $X_2 = 15.39 \text{ cm}$), see 2D-plots in Fig.2.12. Thus the presence of moderate acoustical losses in a medium varies significantly the spatial scale of the light scattering processes. Together with this, a limited number of unit-value maxima will appear as far as our approximate solution is valid. These circumstances make it necessary to estimate potential TFW in more detail.

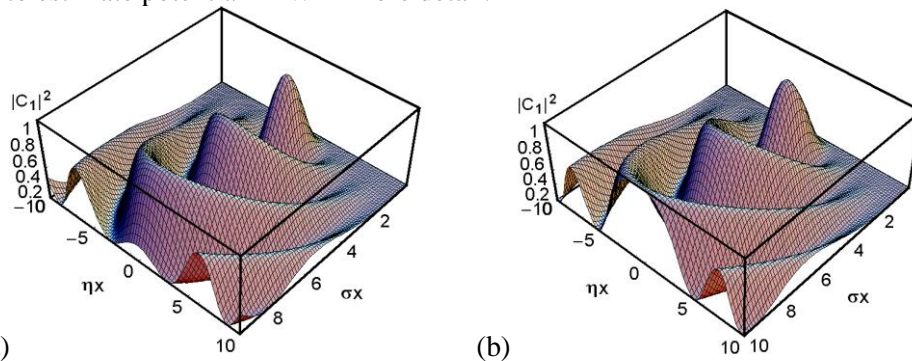


Fig.2.11. The 3D plots for the absolute values of the scattered light intensity profile with $\alpha \neq 0$ and $q_0/q_1 \approx 1$ on the interval $0 \leq \sigma x \leq 3\pi$: (a) $\alpha x = 0.1$ and (b). $\alpha x = 0.5$.

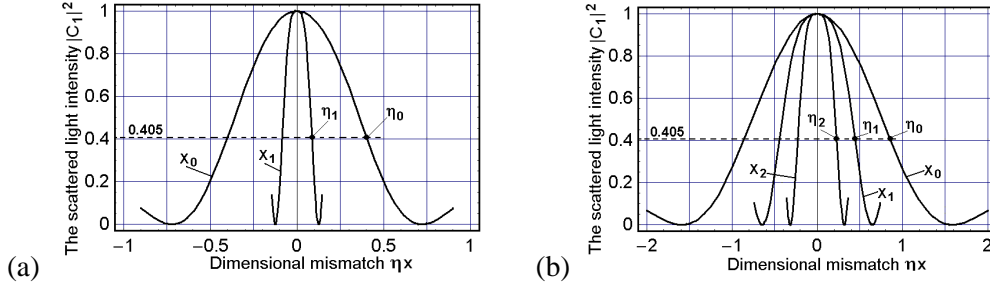


Fig.2.12. The 2D-profiles $|C_1[(\sigma x), (\eta x)]|^2$ with $q_0/q_1 \approx 1$: (a) $\alpha = 0.1 \text{ cm}^{-1}$ and $\sigma = 0.5 \text{ cm}^{-1}$ with $X_0 = 3.768 \text{ cm}$ and $X_1 = 28.55 \text{ cm}$, (b) $\alpha = 0.1 \text{ cm}^{-1}$ and $\sigma = 1 \text{ cm}^{-1}$ wherein $X_0 = 1.709 \text{ cm}$, $X_1 = 6.372 \text{ cm}$, and $X_2 = 15.39 \text{ cm}$

2.5 Some estimations

2.5.1 CaMoO₄

Together with this, one can estimate the potential contributions of the acoustic losses. The coefficient of linear attenuation for the chosen shear acoustic wave passing along the [100]-axis is $\Gamma = 60(\text{dB}/\text{cm GHz}^2)$ in a calcium molybdate single crystal [2.18]. The factor α of the amplitude acoustic losses measured in cm^{-1} can be expressed via the standard relation: $\alpha(\text{cm}^{-1}) = 0.1152 \cdot \Gamma(\text{dB}/\text{cm GHz}^2) \cdot f^2(\text{GHz})$. The carrier frequency f_0 , peculiar to the collinear acousto-optical interaction in calcium molybdate at the above-mentioned light wavelength 671 nm , can be calculated as $f_0 = \Delta n \cdot V / \lambda \approx 34.3 \text{ MHz}$, so that one can estimate the amplitude factor of acoustic losses by $\gamma = \Gamma(\text{dB}/\text{cm GHz}^2) \cdot f_0^2(\text{GHz}) \approx 0.07056(\text{dB}/\text{cm})$ and $\alpha = 0.00813 \text{ cm}^{-1}$. Due to the smallness of the factors γ and α , one can neglect the effect of acoustic attenuation and consider this case like practically lossless one.

The angular divergence of acoustic beam in a calcium molybdate collinear cell at the frequency $f = 34.3 \text{ MHz}$ can be estimated as well. Practically, a reliable spatial size of the initial acoustic beam aperture that we will consider is close to $d \approx 0.2 \text{ cm}$. Thus, one can estimate $\Lambda = V/f = 8.6 \cdot 10^{-3} \text{ cm}$, and $\varphi = \Lambda/d \approx 4.3 \cdot 10^{-2} \text{ rad} \approx 2.464^\circ$, and conclude that the angular divergence of acoustic beam can be also omitted. The full mismatch $\Delta\eta$ is connected with the frequency resolution δf . Due to the above-mentioned expression $\Delta\eta = \pi \delta f / V$, one can find $\delta f = (\Delta\eta \cdot x) / (\pi L)$.

At this step, we are ready to perform a few practical numerical estimations inherent in the collinear interaction at the light wavelength of $\lambda = 671 \text{ nm}$ in the CaMoO_4 -crystalline cell with $M_2 \approx 1.977 \cdot 10^{-18}(\text{s}^3/\text{g})$ and $L = 4.4 \text{ cm}$. The periodicity of collapsing the resolution (see Fig.2.13) is characterized by simple formula $\sigma_m L = m\pi$, so that for a pair of the first periods with $m = 1, 2$ one has $\sigma_1 = \pi/L \approx 0.714 \text{ cm}^{-1}$ and $\sigma_2 = 2\pi/L \approx 1.428 \text{ cm}^{-1}$.

Using the standard determination introduced above, one can write

$$\text{a) } \sigma = U_0 \sqrt{q_0 q_1} \approx \frac{\pi}{\lambda} \sqrt{\frac{P}{2} M_2}, \quad \text{b) } P \approx \frac{2\lambda^2 \sigma^2}{\pi^2 M_2}. \quad (2.20)$$

Consequently, Eq.(2.20) gives $P[\text{W}/\text{mm}^2] \approx 0.457 \cdot (\sigma[\text{cm}^{-1}])^2$, so that $P_1 \approx 0.233[\text{W}/\text{mm}^2]$ for σ_1 and $P_2 \approx 0.932[\text{W}/\text{mm}^2]$ for σ_2 , see Fig.2.13. One can see that reaching the second point of collapsing the resolution needs four-times higher acoustic power density in comparison

with the first point and looks rather conjectural from the viewpoint of requirements to electric strength inherent in the available piezoelectric transducer. Then, the above-presented theoretical 2D-contour plot had shown that each next period exhibits a wider profile in the vicinity of the points $\sigma x \rightarrow (\pi/2) + m\pi$, $m = 0, 1, 2, 3, \dots$ related to maximal efficiency of light scattering at this period. This is why we have restricted ourselves by reaching the first point of collapsing the resolution within the experiments.

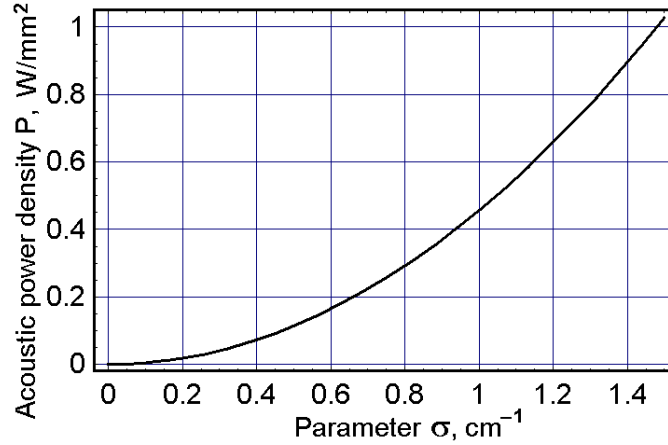


Fig. 2.13. Acoustic power density P vs. the parameter σ at $\lambda = 671 \text{ nm}$ in the above-chosen collinear CaMoO_4 -crystalline cell.

2.5.2 LiNbO_3

Exploiting LiNbO_3 crystal as a material for an AOF requires a set of additional estimations conditioned by the presence of the light-induced absorption and photorefraction in this material. These effects had been observed in LiNbO_3 crystals within the optical range from near ultraviolet to infrared radiation, and it might bring difficulties for optical spectroscopy due to reducing performances of an AOF. Nevertheless, the possibility exists to exploit this crystal, whose optical properties can be modified by relatively small concentrations of some dopants. There are a few dopants such as, for example, iron, magnesium or hafnium, which are widely investigated and used in various applications. Here, however, we will restrict ourselves only to Mg -doped LiNbO_3 crystals[2.22,2.23] keeping in mind potential exploitation of an AOF in near ultraviolet range[2.24].

2.5.2.1 Induced absorption

Originally, light absorption in Mg -doped LiNbO_3 crystals can be characterized by the absorption factor $\alpha_0(\lambda)$ at infinitely small incident optical power density. This factor is rather dispersive in behavior specifically near the edge of absorption, i.e. in near ultra-violet range, and it depends on the particular concentration of dopant. The set of solid lines in Fig. 2.14a illustrates the behavior of the absorption factor $\alpha_0(\lambda)$ for the congruent LiNbO_3 crystal (CLN) and the congruent LiNbO_3 crystals doped by 4, 7 or 9 % of Mg (see notations CMg4, CMg7, and CMg9) under action of infinitely small incident optical power density. The second set of curves is presented for the near ultra-violet range in Fig. 2.14b. It shows the above-noted solid lines (conditioned by the absorption factor $\alpha_0(\lambda)$ only) together with the dotted lines, which depict the combined optical losses including the light-induced absorption governed by an additional external spectral flux I . This additional flux is chosen in such a way that contributions of the light-induced absorption do not exceed about 10% of the original optical losses $\alpha_0(\lambda)$ for all the considered concentrations of magnesium dopant [2.22], and moreover, this flux has spectrally uniform distribution along all the visible and near ultra-violet ranges.

Experimental data show [2.22] that the noted 10% excess over $\alpha_0(\lambda)$ means physically achieving the saturation of the light-induced absorption. After that, one can find from Fig. 2.14 that the best option, i.e. appearing a minimal light-induced absorption, is associated evidently with 4% *Mg*-doped *LiNbO₃* crystal providing, for example, $\alpha_0(\lambda) \approx 0.28 \text{ cm}^{-1}$ at $\lambda = 370 \text{ nm}$.

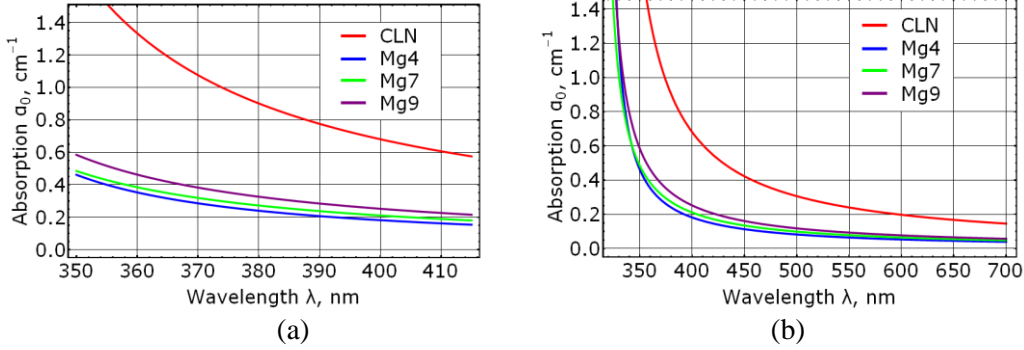


Fig. 2.14. Optical absorption vs. the incident light wavelength λ : within a wide spectrum (a) and in near-ultraviolet range (b) for various concentration of Mg. Solid lines are for infinitely small incident optical power density, i.e. for $\alpha_0(\lambda)$, while dotted lines are for the above-described combined spectral flux, i.e. at the saturation

Anyway, the plots presented in Fig. 14b can be interpreted as the presence of total optical losses $\alpha_T = \alpha_0 + \alpha_2 I(x)$ consisting of the basic absorption $\alpha_0(\lambda)$ together with an additional contribution $\alpha_2 I(x)$, where the dispersive factor $\alpha_2(\lambda)$ describes the nonlinear light-induced absorption. The last contribution depends on the external light flux $I(x)$, which is varied during its propagation along a crystal due to optical losses, while $I(x=0) = I_0$. In the case when I_0 can be considered as an infinitely small value, one yields the absence of the light induced absorption with linear losses $\alpha_T \approx \alpha_0$. By this it means that an effect of the self-action takes place, and in the supposition of exponential attenuation, one can write, for example,

$$I(x) \approx I_0 \exp[-(\alpha_0 + \alpha_2 \{ I_0 \exp[-(\alpha_0 + \alpha_2 I_0)x] \} x)] \quad (2.23)$$

in the second approximation. As it follows from Eq.(2.23), the assumed difference of 10% does not look too dramatic from the viewpoint of losses within the doped *LiNbO₃* crystal based AOF. Therefore, for the illustrative difference of 10% one can conclude that the doped *LiNbO₃* crystal length in AOF can be estimated from the diagram presented in Fig. 2.15. By this it means that, for instance, the aforementioned 4% *Mg*-doped *LiNbO₃* crystal is able to provide the crystal length about 8 *cm* at $\lambda = 370 \text{ nm}$ with the optical losses $\alpha_0(\lambda) \approx 0.28 \text{ cm}^{-1}$ as well as the length close to 13 *cm* at $\lambda = 405 \text{ nm}$ with the optical losses $\alpha_0(\lambda) \approx 0.17 \text{ cm}^{-1}$, if the chosen optical transmittance $\sim 10\%$ is technically acceptable. For comparison, the plots related to the visible range at $\lambda = 532 \text{ nm}$ with $\alpha_0(\lambda) \approx 0.07 \text{ cm}^{-1}$ are shown as well.

These plots demonstrate that one can observe some dynamic in varying losses. On the one hand, ideal case corresponds to the absence of light-induced absorption when only the linear losses give their contribution and $\alpha_T \approx \alpha_0$ due to infinitely small value of I_0 , see the dotted straight lines in Fig. 2.15. On the other hand, the formal theoretical limit $\alpha_T = \alpha_0 + \alpha_2 I_0$ can be noted near the input facet of a crystal, see the dashed straight lines in Fig. 2.15. Physically, the initial maximal optical losses $\alpha_T = \alpha_0 + \alpha_2 I_0$ exhibit depletion of light-induced contribution together with reducing the light flux $I(x)$, so that optical losses will slowly approach to $\alpha_T \approx \alpha_0$, see the solid curves in Fig. 2.15 described by Eq.(2.23) in the second approximation.

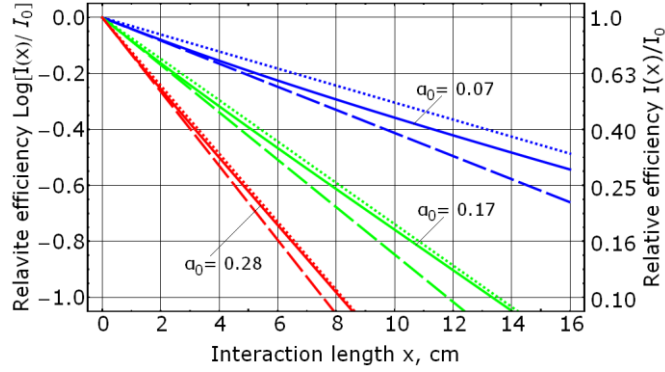


Fig. 2.15. Level of optical losses vs. 4%: Mg – doped $LiNbO_3$ crystal length: the dotted straight lines are for the best case, i.e. for only the linear losses $\alpha_T \approx \alpha_0$, the dashed straight lines are for the worst case, i.e. for optical losses $\alpha_T = \alpha_0 + \alpha_2 I_0$, and the solid curves are for varying α_T in the second approximation, described by Eq.(2.23)

2.5.2.2 Photorefraction

Photorefraction means changing the refractive indices caused by the rearrange of charges and holes in a material. Such changes, known also as “optical damage”, are governed by the incident optical field, and they depend on the intensity of that field. There is a chance to use $LiNbO_3$ crystals, which is supported by the improved optical damaged resistance in Mg – doped $LiNbO_3$ crystals [2.19,2.20] for the AOFs in near ultraviolet range [2.21]. Let us start from so-called uniform nonlinear photorefraction, when the effect of photorefraction does not exhibit any dependence on coordinates and time. Quantitatively, the uniform photorefraction in $LiNbO_3$ crystals under an action of an external optical beam with the particular light wavelength λ can be estimated as a variation of the birefringence $\delta|\Delta n|_\lambda$ using the scalar expression [2.23]

$$\delta|\Delta n|_\lambda \cong \frac{Rk I_{0,\lambda} \alpha_0(\lambda)}{\sigma_C}, \quad (2.24)$$

where $|\Delta n|$ is the birefringence of a crystal, R is the generalized electro-optical coefficient, k is the Glass constant, $I_{0,\lambda}$ is the incident light intensity at the individual light wavelength λ , and $\sigma_C = \sigma_D + \sigma_P$ is the conductivity, in which σ_D is the dark conductivity and σ_P is the photoconductivity. For the sake of simplicity, one can consider the factors R , k , and σ_C independent of the optical wavelength in Eq.(2.24). One can see the directly proportional dependence between the light-induced birefringence change $\delta|\Delta n|_\lambda$ and the optical absorption factor $\alpha_0(\lambda)$ depending only on the optical wavelength remaining unaltered. After that, one can examine the data related to the optical absorption factor $\alpha_0(\lambda)$ and the light-induced birefringence change $\delta|\Delta n|_\lambda$ [2.24] measured in the saturation regime and valid, consequently, for long exposure times. These data had been obtained in the congruent $LiNbO_3$ crystal (CLN) and in the congruent $LiNbO_3$ crystal doped by 4 % of Mg (CMg4) to increase the resistance to photorefraction. With these results, it is possible to estimate the spectral dependence for the light-induced birefringence change $\delta|\Delta n|_\lambda$ in $Mg : LiNbO_3$ crystal.

Figure 2.16 illustrates the effect of photorefraction in $LiNbO_3$ crystals in the near ultra-violet range. One can see that the use of an adequate amount of Mg as a dopant improves the

resistance to photorefraction in comparison with an undoped $LiNbO_3$ crystal. For optical wavelengths larger than 370 nm , a contribution of the photorefractive effect remains constant up to mid infrared wavelengths. As it is seen in Fig. 2.16, the photorefraction effect is reasonable for the congruent $LiNbO_3$ crystal (CLN) at the wavelengths longer than 340 nm . Nevertheless, this situation can be definitely improved with the use of the congruent $Mg : LiNbO_3$ (CMg4) crystal whose acceptable level of photorefraction is shifted down to about 320 nm .

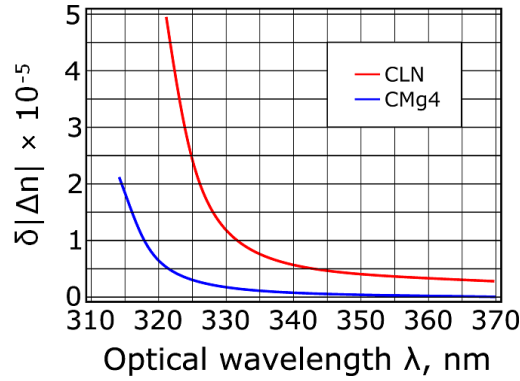


Fig. 2.16. Spectral dependencies for the light-induced birefringence change $\delta|\Delta n|_{\lambda}$: in the congruent $LiNbO_3$ crystal (red line) and in the congruent $Mg : LiNbO_3$ (blue line)

Then, as it had been described in section 2.3.1, the total dispersive optical losses $\alpha_T = \alpha_0 + \alpha_2 I(x)$ consist of the basic absorption $\alpha_0(\lambda)$ together with an additional contribution $\alpha_2 I(x)$, where the dispersive factor $\alpha_2(\lambda)$ describes the nonlinear light-induced absorption, while $I(x) = I_0 \exp[-(\alpha_0 + \alpha_2 I(x))x]$. Now, the product $I_{0,\lambda} \alpha_0(\lambda)$ in Eq.(2.24) has to be substituted by the other product $I_{\lambda}(x) \alpha_T(\lambda)$, which looks as

$$\alpha_T I(x) = I_0 \exp[-(\alpha_0 + \alpha_2 I_0)x] (\alpha_0 + \alpha_2 I_0 \exp\{-[\alpha_0 + \alpha_2 I_0]x\}) \quad (2.25)$$

in a reasonable approximation. For infinitely thin samples $x \rightarrow 0$ or for infinitely small light flux intensity $I_0 \rightarrow 0$, Eq.(2.25) gives

$$\text{a) } \alpha_T I(x) = I_0 (\alpha_0 + \alpha_2 I_0), \quad \text{b) } \alpha_T I(x) \approx I_0 \alpha_0 \exp(-\alpha_0 x), \quad (2.26)$$

respectively. Then, when $x \rightarrow 0$ and $I_0 \rightarrow 0$ together, both the Eqs.(2.26) give the same limit $\alpha_T I(x) \approx I_0 \alpha_0$ as it was in Eq.(2.24). It is seen from Eq.(2.25) that even using that approximation, one arrives at nonlinear photorefraction, whose effect is decreasing with an increasing length of the crystal, so that for really thick samples, about 10 cm and more, one has to apply exponential coordinate dependences, which involve faster attenuation into consideration. This reduction in the photorefraction effect leads, in fact, to additional variations of the birefringence along a crystal, i.e. to another kind of non-uniformity for the birefringence that affects performances of the AOF. At the same time, one can keep a minimum of terms that includes the initial light intensity I_0 , which can be small in practice. In doing so, Eq.(2.25) can be expanded into a series as

$$\alpha_T I(x) \approx I_0 \exp(-\alpha_0 x) \{ \alpha_0 + \alpha_2 I_0 [\exp(-\alpha_0 x) - \alpha_0 x] \} \quad (2.27)$$

in the second approximation with respect to the intensity I_0 , which gives both the Eqs.(2.26) in those limits.

At this step, rather well grounded experimentally supposition can be made, namely, variations of the birefringence $\delta|\Delta n|_{\lambda}$ are additive in behavior when, for example, a few optical beams

with various light wavelengths will be directed on a crystal. By this it means that, in the case of a black body radiation with the incident spectral flux density $F(\lambda)$, the combined effect of photorefraction within all the spectral range $\Delta\lambda$ under action of the total flux I_0 can be estimated from Eqs.(2.24) and (2.27) as

$$\begin{aligned} \text{a) } \delta |\Delta n| &\cong \frac{Rk}{\sigma_c} \int_{\Delta\lambda} \left\{ \alpha_0(\lambda_0) \exp[-\alpha_0(\lambda_0)x] + \right. \\ &\left. \left[\exp[-\alpha_0(\lambda_0)x] \{ \exp[-\alpha_0(\lambda_0)x] - \alpha_0(\lambda_0)x \} \int_{\Delta\lambda} \alpha_2(\lambda_0, \lambda_1) F(\lambda_1) d\lambda_1 \right] \right\} F(\lambda_0) d\lambda_0, \\ \text{b) } I_0 &= \int_{\Delta\lambda} F(\lambda) d\lambda. \end{aligned} \quad (2.28)$$

Because of the data from Fig. 2.16, the lower bound of integration in Eq.(2.28) must be taken close to 320 nm or higher to reduce the potential influence of photorefraction. Considering the fact that the expected range of observations is narrow enough, one can consider the incident spectral flux density $F(\lambda)$ as almost constant of λ and take $F(\lambda)$ out of the corresponding integrals in Eq.(2.28). In doing so., one can obtain a quadratic algebraic equation relative to $F(\lambda)$ from Eq.(2.28a) and find

$$\text{a) } \frac{\sigma_c \delta |\Delta n|}{R k_0} \approx A_0(x)F + A_1(x)F^2, \quad \text{b) } A_0(x) = \int_{\Delta\lambda} \alpha_0(\lambda_0) \exp[-\alpha_0(\lambda_0)x] d\lambda_0,$$

$$\text{c) } A_1(x) = \int_{\Delta\lambda} \left[\exp[-\alpha_0(\lambda_0)x] \{ \exp[-\alpha_0(\lambda_0)x] - \alpha_0(\lambda_0)x \} \int_{\Delta\lambda} \alpha_2(\lambda_0, \lambda_1) d\lambda_1 \right] d\lambda_0. \quad (2.29)$$

$$F \cong \frac{1}{2A_1^2(x)} \left[-A_0(x) + \left(A_0^2(x) + 4A_1(x) \cdot \frac{\sigma_c \delta |\Delta n|}{R k_0} \right)^{1/2} \right]. \quad (2.30)$$

Now one has to establish a proper criterion for estimating an acceptable level of photorefraction, which still does not affect performances, in particular the spectral resolution of the AOF. For this purpose, we suggest to use criterion that had been exploited for the optical non-uniformity ΔB of the birefringence in a crystal reflecting optical imperfectness along a crystal. In our case, the same birefringence $|\Delta n| \approx 0.1$ is for both the congruent $LiNbO_3$ crystal (CLN) and for the congruent 4% Mg : $LiNbO_3$ (CMg4) crystal. By this it means that rather acceptable level of photorefraction, considering a homogeneous change in the birefringence over all the spectral range, can be estimated by the value $\delta |\Delta n| \leq 10^{-6}$. Then, using Eq.(2.30), one can estimate the maximum incident spectral flux density measured in $W/(mm^2\text{\AA})$, under action of which the effect of photorefraction on optical properties of $LiNbO_3$ crystals is small enough to be neglected, i.e. for which the photorefraction will be acceptable, i.e. $\delta |\Delta n| < 10^{-6}$.

If the product: $A_1(x=0)F$ in Eq.(2.29a) can be considered small in comparison with $A_0(x=0)$, a first approximation can be used for estimating maximal flux density $F(\lambda)$. Consequently, one can obtain

$$F \cong \frac{\sigma_c \delta |\Delta n|}{R k_0 A_0(x=0)}. \quad (2.31)$$

Using the above-threshold for acceptable photorefraction, one can estimate the limits for the spectral flux density by $F_{\max} \leq 43 \mu W/(mm^2\text{\AA})$ in the $LiNbO_3$ and $F_{\max} \leq 355 \mu W/(mm^2\text{\AA})$

for the 4% $Mg : LiNbO_3$ within the spectral range $\Delta\lambda$ from $320nm$ to $700nm$. Thus, we can be sure that it will be possible to neglect the photorefractive effect in the potential AOF.

For the common case of stars, the light intensity is of the order of $10^{-18} W/(mm^2 \cdot \text{\AA})$ on Earth. With this in mind, one can select one of the brightest stars, namely, Vega with $F_0 \approx 6.2 \cdot 10^{-18} W/(mm^2 \cdot \text{\AA})$ to make the respective estimations. Considering the light from Vega, collected by a telescope of $2m$ in diameter ($F_T \approx 1.95 \cdot 10^{-5} \mu W/(mm^2 \cdot \text{\AA})$), the calculated light-induced birefringence change is $\delta|\Delta n| \approx 10^{-12}$ for the congruent $LiNbO_3$ and $\delta|\Delta n| \approx 10^{-13}$ for the 4% $Mg : LiNbO_3$.

2.6 General scheme for experiments

To realize experimentally the process of collinear interaction we have used the scheme shown in Fig. 2.17. It consists of a continuous-wave laser, a $CaMoO_4$ -crystalline acousto-optical cell with a pair of the Glan-Taylor crystalline polarizers (with the extinction ratio 10^5 each), a wide-aperture silicon photo-detector, and a set of electronic equipment for both generating and registering the corresponding electric ultra-high-frequency (UHF) radio-wave signals. Initially, the tunable UHF-signal is applied to the electronic input port of the collinear acousto-optical cell through a wide-band UHF-amplifier HD18858 ($10 - 1000 MHz$, $8W$), see Fig. 2.17, and to the input of an oscilloscope (computer) as the etalon signal.

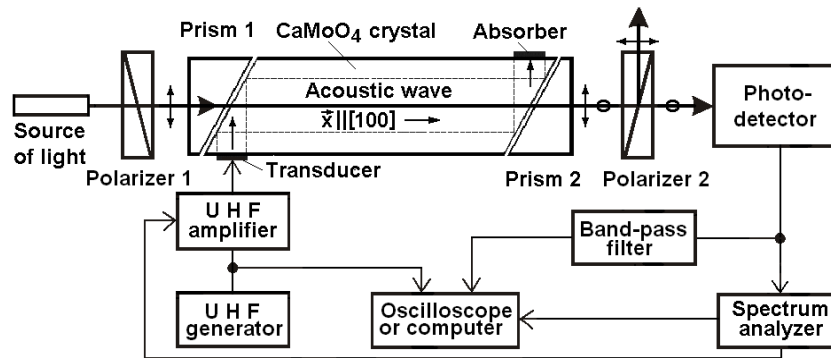


Fig.2.17. Schematic arrangement of the experimental set-up

A two-mode co-propagating collinear $CaMoO_4$ crystalline cell was characterized by a crystal length $L = 4.4 cm$ along the $[100]$ -axis, an acoustic velocity $V = 2.95 \cdot 10^5 cm/s$ for the shear elastic mode whose displacement vector is oriented along the $[001]$ -axis. The continuous-wave beams (solid-state lasers from CrystaLaser; the output optical power $\sim 30 - 40 mW$; $\lambda = 444, 532, \text{ and } 633 nm$; transverse mode TEM_{00} ; single longitudinal mode, providing narrow enough optical spectral line) had been used as an optical pump during the experiments with the traveling-wave regime of interaction between the pumping light beam and the acoustic wave. It had been done, first, to keep just the visible range of operation with light beams simplifying the experimental conditions of observations. Then, the visible range of light overlaps rather wide range of acoustic frequencies ($35 - 95 MHz$) and makes accessible varying the acoustic losses as much as possible (about 5 times) due to a square-law dependence of the attenuation on the frequency. Turning back to the scheme, the first polarizer was precisely aligned in correspondence with the optical axes of a crystal in a cell. As the optical pump and the continuous-wave acoustic wave were interacted, already two orthogonally polarized light beams, incident and signal ones, passed through a cell. The second polarizer gave us an opportunity to be aligned in correspondence with the polarization of the signal beam and to extract the output optical signal, see Fig. 2.17. Then, one can restrict oneself by a maximal level

$P \leq 0.5 \text{ W/mm}^2$ of acoustic power density, which is conditioned by the absolute acoustic power magnitude of about 2 W and the acoustic beam cross section of about 4 mm^2 in the chosen collinear cell. Consequently, one can calculate that $\sigma \leq 2 \text{ cm}^{-1}$. These estimations demonstrate that the above-noted limitations on both the needed acoustic power densities and the magnitudes of the parameter σ , related to the firsts extrema, lie in the frames of acceptable values.

Not all the functional connections shown in Fig. 2.18 had been exploited at the same time. At least three regimes can be separated. One of them was related to measuring the light intensity dependences at the fixed acoustic carrier frequency. Two others were connected with estimating the frequency dependencies at stepwise variations of the applied acoustic power. They both include exploitation of the sweep-generator from spectrum analyzer and provide operating with the band-pass filter (bandwidth $\sim 5 \text{ kHz}$) and oscilloscope as well as with the spectrum analyzer (bandwidth $\leq 10 \text{ Hz}$), in particular, for calibrations and accurate measurements of frequency.

2.7 Experimental results

The nonlinear dynamics of varying the transmission functions peculiar to the advanced collinear CaMoO_4 acousto-optical cell has been sequentially followed during our experiments. A triplet of experiments had been carried out. At first, the scattered light intensity $|C_1|^2$ as the function of the acoustic power density P with the fixed length of interaction $L = 4.4 \text{ cm}$ had been registered under condition of $P \leq 0.5 \text{ W/mm}^2$ (i.e. $\sigma \leq 2 \text{ cm}^{-1}$). To identify better the expected influence of moderate linear losses on the transmission functions of that cell the maximal acceptable acoustic frequency $f_{\max} = 94.34 \text{ MHz}$, accompanied by $\lambda = 444 \text{ nm}$, had been chosen to provide the highest possible for this cell acoustic attenuation $\alpha = 0.1152 \cdot \Gamma f_{\max}^2 \approx 0.0615 \text{ cm}^{-1}$. For the comparison, the similar plot for $\alpha = 0.0261 \text{ cm}^{-1}$ related to $f = 61.24 \text{ MHz}$ and $\lambda = 532 \text{ nm}$ has been chosen. The corresponding experimental plots are depicted in Fig. 2.18. One can see that a few extrema, namely, two maxima and one zero had been achieved at each optical wavelength and registered during the measurements carried out. The presented here trace for $\lambda = 532 \text{ nm}$ can be compared with the theoretical plot.

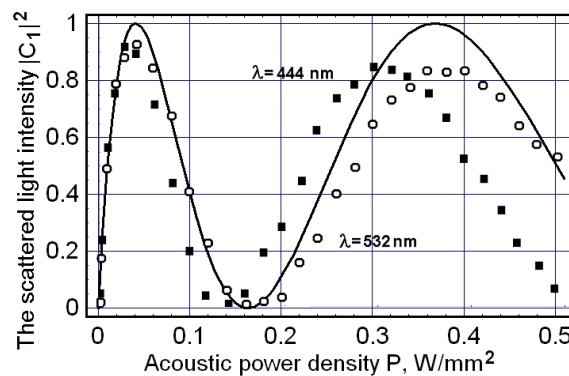


Fig. 2.18. The scattered light intensity $|C_1|^2$ versus the acoustic power density P with $\alpha = 0.0261 \text{ cm}^{-1}$ (solid line is for theory and circles are for experiment at $f = 61.24 \text{ MHz}$, $\lambda = 532 \text{ nm}$) and $\alpha = 0.0615 \text{ cm}^{-1}$ (squares are for experiment at $f_{\max} = 94.34 \text{ MHz}$, $\lambda = 444 \text{ nm}$) in the CaMoO_4 -cell.

Merely the presence of moderate linear acoustic losses is able to affect the width of the transmission function. Reshaping the transmission function has been followed with

approximately one and the same input optical pump at various light wavelengths and at very close to one another values of the product σL , which all can be characterized as “rather small” in a view of realizing a limit to infinitely small input acoustic signals.

To keep a balance between as low as acceptable level of the acoustic power in that limit, on the one hand side, and to have an option for reliable measurements of the transmission function width, on the other hand side, the product $\sigma L \approx 0.2$ had been chosen experimentally. In fact, fixing this product leads, nevertheless, to $\sigma = 0.04545 \text{ cm}^{-1}$ and remarkably different levels of the needed acoustic power densities $P[\text{W}/\text{cm}^2] \approx 0.27 \cdot (\lambda[\mu\text{m}])^2$ for its realization. Using Eq.(2.22b) for $\lambda_{A,B,C} = \{633, 532, 444\} \text{ nm}$ connected with $f_{A,B,C} = \{43.47, 61.24, 0.533\} \text{ MHz}$, one can find $P_{A,B,C} = \{1.082, 0.764, 0.533\} \text{ mW}/\text{mm}^2$ and the products $(\alpha L)_{A,B,C} \approx \{0.0575, 0.114, 0.271\}$, respectively. Then one can estimate theoretically the mismatches ηx as the function of the total acoustic losses αL at various frequencies as $(\eta x)_A = 1.614$, $(\eta x)_B = 1.656$, and $(\eta x)_C = 1.761$, which give theoretically $\delta f_A = 68.89 \text{ kHz}$, $\delta f_B = 70.53 \text{ kHz}$, and $\delta f_C = 75.15 \text{ kHz}$.

A few examples of the corresponding digitized oscilloscope traces, estimated at the level of 0.405 conditioned by the Rayleigh criterion. These traces for the scattered light intensity $|C_1|^2$ had been observed at the output of the above-described collinear CaMoO_4 cell at various carrier acoustic frequencies, which provide various magnitudes of the linear acoustic losses depending quadratically on those frequencies.

Finally, the effect of non-linear narrowing had been observed via measuring the widths peculiar to profiles of the scattered light intensity $|C_1|^2$ as a function of the applied acoustic power density explained in terms of the dimensionless product σL . For this purpose, we had taken the regime of scattering the green light with $\lambda = 532 \text{ nm}$ connected with the acoustic wave frequency $f_0 = 61.24 \text{ MHz}$, which provides sufficiently tangible total acoustic attenuation $\alpha L \approx 0.114$ all over the cell aperture. At first, both the 2D-theoretical plots with the product $\alpha L \approx \{0, 0.0575, 0.114, 0.271\}$ and the observed experimental data as points are combined in Fig. 2.19.

Then, the oscilloscope traces for the scattered light component intensity $|C_1|^2$ detected during the experiments with the collinear CaMoO_4 crystalline cell and estimated at the level 0.405 conditioned by the Rayleigh criterion. All these traces can be interpreted in terms of the above-developed theory.

The most left triplet of experimental points in Fig. 2.19 corresponds to $\sigma L \approx 0.20$ that is very close to zero. They reflect the transmission functions inherent in the regime with almost infinitely small amplitude of the controlling acoustic signal. This value σL (which is non-zero, in fact) had been taken as an example to show adequately conventional representation for the transmission function width being reasonably close to the traditional estimation $\delta f \approx V/L = 67.045 \text{ kHz}$ in our case, as well as to have a chance for identifying the output light distributions whose relative intensity were small enough, i.e. about 3.5%. All the other points in Fig. 2.19 are related to only $\lambda = 532 \text{ nm}$ with varying product σL .

The points, peculiar to $\sigma L \approx \{0.5, 1.0, \pi/2\}$ are presented in Fig. 2.19; and the last of them is illustrated by the oscilloscope trace in Fig. 2.20a. From the viewpoint of widely used acousto-optic approach, they can be considered as a natural testimony of growing the relative intensity

of the output optical signal up to the products σL equal to 0.202, 0.657, and ~ 1.0 under action of the increasing acoustic power density. They all exhibit the transmission function width of more or less the same order, which varies slightly from the above-mentioned 71.03 kHz to $\delta f \approx 70.42$ kHz, $\delta f \approx 67.84$ kHz, and $\delta f \approx 64.04$ kHz for $\sigma L \approx \{0.5, 1.0, \pi/2\}$, respectively.

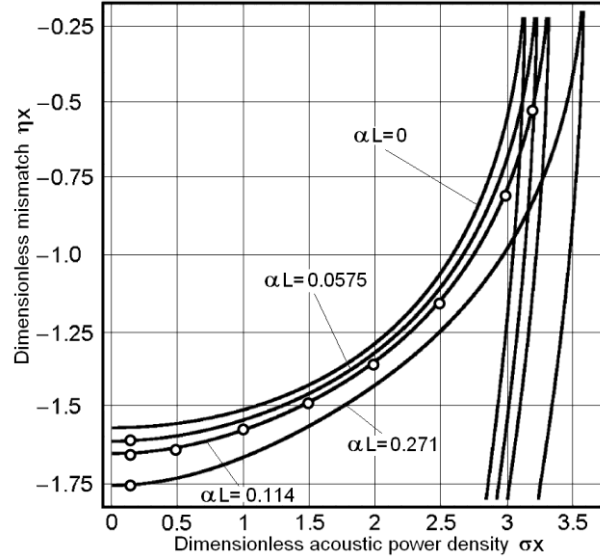


Fig. 2.19. Combined diagram reflecting both the 2D-theoretical plots with the product $\alpha L \approx \{0, 0.0575, 0.114, 0.271\}$ and all the above-noted experimental points.

The lossless case is $\alpha L = 0$.

The numerical estimations are given by the values $\delta f = 69.81$ kHz, $\delta f = 67.34$ kHz, and $\delta f = 63.40$ kHz at the same σL . Such a conclusion looks rather plausible within quasi-linear approximation for the transmission function as well as in the course of possible measurements in the frequency domain with not enough accuracy. Nevertheless, further increase of the acoustic power density, depicted by the points with $\sigma L \approx 2.0$ and $\sigma L \approx 2.5$ in Fig. 2.19 and the oscilloscope trace in Fig. 2.20b, is able to demonstrate step by step that the existing specific acousto-optical nonlinearity leads to narrowing the transmission function to $\delta f \approx 58.46$ kHz and $\delta f \approx 50.17$ kHz, respectively, while theoretically one can find $\delta f \approx 57.67$ kHz and $\delta f \approx 48.987$ kHz. This process is accompanied by decreasing the relative intensity of the output optical beam down to about 0.9 and 0.5 in the so chosen points. Finally, the last traces, see Fig. 2.19 as well as Figs. 2.20c and 2.20d, illustrate obviously nonlinear process of narrowing the transmission function or improving the frequency resolution in the vicinity of the first point $\sigma L = \pi$ of a collapse. Namely the values $\sigma L \approx 3.0$ and $\sigma L \approx 3.20$ have been taken to have an opportunity for revealing the transmission function characterized by $\delta f \approx 34.13$ kHz and even $\delta f \approx 21.95$ kHz (theoretically $\delta f \approx 33.46$ kHz and $\delta f \approx 21.52$ kHz) whose relative intensities become already really small and do not exceed 0.09 and 0.01, respectively.

Thus, one can conclude that we have revealed nonlinear narrowing of the transmission function inherent in collinear acousto-optical interaction occurred by the acoustic waves in a medium with moderate losses. This nonlinear effect can be interpreted also as improving the spectral and frequency resolution peculiar to the equivalent collinear acousto-optical filter operated by the controlling acoustic waves of finite amplitude. In fact, we have found an opportunity to exchange a portion of transmittance for a portion of accuracy. Sometimes, for instance in astrophysical observations, it could be useful practically when extremely bright object is under optical spectrum analysis. Rather adequate theory of this effect has been developed analytically and illustrated via the corresponding computer simulations. In particular, a periodicity for the

nonlinear narrowing of the transmission function, which includes a set of points for its collapses originating periodically, has been found and estimated. It has been shown that the first period of similar collapsing exhibits the best relation between the width and magnitude of the narrowed transmission function from the viewpoint of practical application. Then, the needed estimations have been performed for collinear interaction in the visible range in a CaMoO_4 crystal. The results of our experiments illustrating the nonlinear narrowing of the transmission function within propagation of acoustic waves with moderate losses in the collinear calcium molybdate crystalline cell have been presented and briefly discussed.

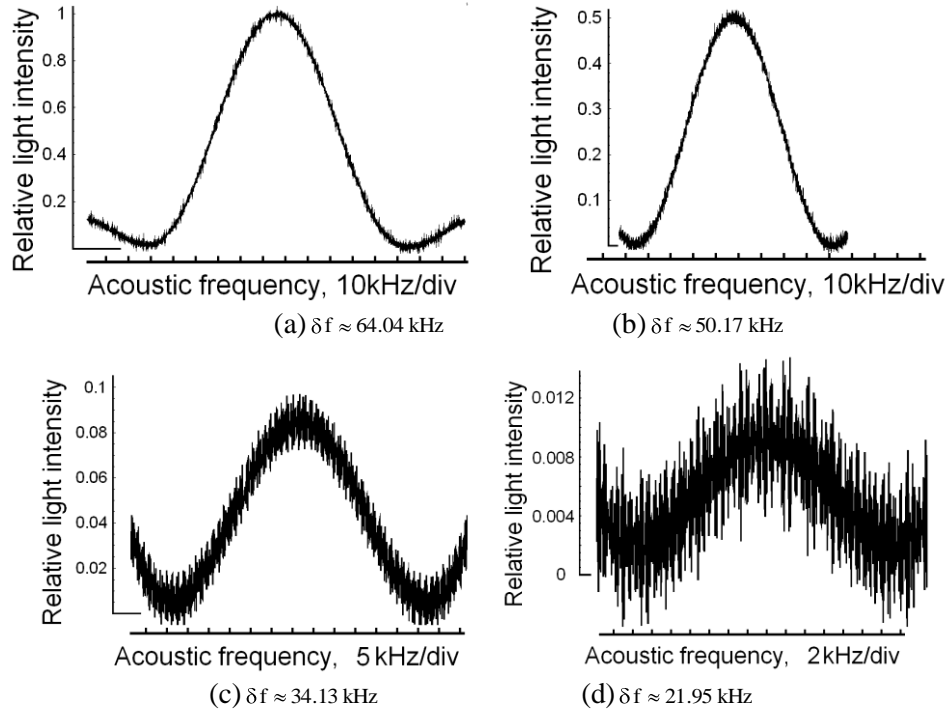


Fig. 2.20. The digitized oscilloscope traces for the scattered light intensity $|C_1|^2$ for the green light with $\lambda = 532 \text{ nm}$ observed at the output of the collinear CaMoO_4 cell near the central carrier acoustic frequency $f_0 = 61.24 \text{ MHz}$ and estimated at the level 0.405. Reshaping the transmission function is followed at the same optical pump in variable scales: (a) $\sigma L \approx \pi/2$, $P \approx 0.0365 [W/mm^2]$; (b) $\sigma L \approx 2.5$, $P \approx 0.0925 [W/mm^2]$, (c) $\sigma L \approx 3.0$, $P \approx 0.133 [W/mm^2]$, and (d) $\sigma L \approx 3.2$, $P \approx 0.152 [W/mm^2]$.

Using the experimental data, one can create the combined diagrams, which include theoretical plots for the spectral resolution $\delta\lambda$ and the relative scattered light intensity I versus the acoustic power density P of the above-noted slow shear acoustic mode at $\lambda = 405 \text{ nm}$ with $f = 1.04 \text{ GHz}$, $\alpha = 0.0991 \text{ cm}^{-1}$, $\alpha_0 \approx 0.17 \text{ cm}^{-1}$ and at $\lambda = 440 \text{ nm}$ with $f = 0.896 \text{ GHz}$, $\alpha = 0.0740 \text{ cm}^{-1}$, $\alpha_0 \approx 0.12 \text{ cm}^{-1}$, see Fig. 2.21.

The congruent LiNbO_3 (CLN) exhibits a higher optical absorption coefficient compared to 4% Mg-doped LiNbO_3 . Theoretically speaking, this fact demerit the transparency of the congruent LiNbO_3 crystal and therefore, the efficiency is reduced considerably, for example, peak efficiency of about 30% for 405 nm to a peak efficiency of 5% in the same wavelength. Nevertheless, the expected spectral resolution is not affected dramatically. Following the previous example, the spectral resolution for the peak efficiency is about 0.25 \AA for both cases and using the same acoustic power density.

In Fig. 2.21, the experimental data provide a spectral resolution $\delta\lambda$ which is just marginally larger than the theoretical prediction, at both wavelengths and along all the range of acoustic

power density: at $\lambda = 405$ nm the average overestimation is of 0.019 Å, while at 440 nm the experimental $\delta\lambda$ is in average (excluding the point at $P = 0.12$ W/mm²) 0.022 Å larger. As far as the relative scattered light intensity is concerned, we observe a relatively good agreement with the theoretical curve all over the probed acoustic power density P interval. However, at both wavelengths, the experimental maximum value is lower (of about 0.0041 at 405 nm and 0.0065 at 440 nm), although the value of P , at the peak of efficiency curve, coincides with the theoretical prediction. The noncoincidences of theoretical and experimental peaks for the relative scattered light intensities are about 8% and 12% at 405 nm and 440 nm, respectively.

Generally, the differences between theoretical performances and the experimentally obtained data shown in Fig. 2.21 indicate that evidently not all the phenomena (maybe even some of the omitted ones) associated with the effect under consideration had been taken into account, so that our theoretical model could be potentially improved. The last one is true especially for areas of relatively higher acoustic power density. Nevertheless, the smallness of those differences confirms substantially the opportunity to make the above-realized approximations, i.e. omitting some terms.

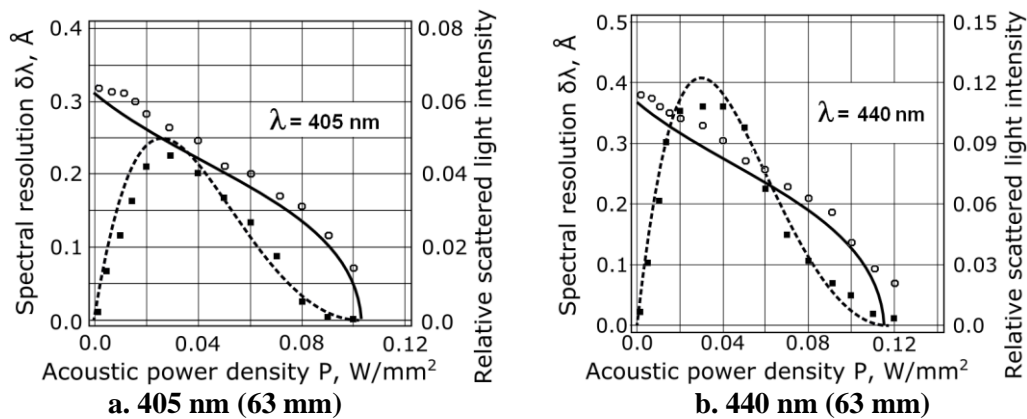


Fig. 2.21. Combined plots of the spectral resolution $\delta\lambda$ and the relative scattered light intensity vs. the acoustic power density P for the pure slow shear elastic mode passing along the $[010]$ -axis in the congruent $LiNbO_3$ -crystal: (a) at $\lambda = 405$ nm, $f = 1.04$ GHz, $\alpha = 0.0991$ cm⁻¹, $\alpha_0 \approx 0.17$ cm⁻¹ and (b) at $\lambda = 440$ nm, $f = 0.896$ GHz, $\alpha = 0.0740$ cm⁻¹, $\alpha_0 \approx 0.12$ cm⁻¹. Here, the solid lines (theory) and circles (experiment) are for the spectral resolution $\delta\lambda$, while the dotted lines (theory) and squares (experiment) are for the relative efficiency of the light scattering.

2.8 Conclusions

Thus, one can conclude that we have revealed nonlinear squeezing of the transition function inherent in the collinear acousto-optical interaction under condition of the simplifying approximation of lossless (or low-loss) propagation for the acoustic waves [2.25-2.28]. This nonlinear effect can be interpreted also as improving the spectral and frequency resolution peculiar to the collinear acousto-optical filter operated by the controlling acoustic waves of the finite amplitude. Rather adequate theory of this effect has been developed analytically and illustrated via the corresponding computer simulations. In particular, a periodicity for the nonlinear squeezing of the transition function, which includes a set of points for its collapses originating periodically, has been found and estimated. It has been shown that the first period of similar collapsing exhibits the best relation between the width and magnitude of the squeezed transition function from the viewpoint of practical application. Then, the needed estimations has been performed for the collinear interaction, which made it possible to choose a dark-red light laser beam, lying still in the visible range, and a low-frequency acoustic wave, providing its almost lossless propagation, in a $CaMoO_4$ single crystal. Finally, the results of our experiments illustrating the nonlinear squeezing of the transition function with lossless propagation of

acoustic waves in the collinear calcium molybdate crystalline cell have been presented and briefly discussed.

The encouraging results from the previous sections support the use of a 4% Mg : LiNbO₃ AOF as a high-resolution dispersive element for a spectrograph for astronomical observations. We summarize in Table 2.2 four illustrative examples of the performance of such AOF operating in nonlinear regime.

The transmission efficiency steeply increases with increasing light wavelength and with decreasing length of the filter, nevertheless the efficiency still remains higher than 30% in the near ultraviolet, if the spectral resolution is limited to $\delta\lambda = 0.28\text{--}0.29 \text{ \AA}$. However, we demonstrated the possibility to reach a resolution as high as $\delta\lambda = 0.12\text{--}0.15 \text{ \AA}$ ($R > 24600$), preserving at the same time an efficiency higher than 10% over all the spectral interval that we considered [2.29-2.31]. Also note that the results are quite similar for both the longitudinal and the shear modes.

We analyzed in their combined totality all the possible factors determining efficiency of operation and spectral resolution and we obtained the highest available spectral resolution for any collinear AOF to our knowledge. We also explored the opportunity to trade an amount of efficiency for an improvement in resolution.

Finally, we have realized proof of principle experiments with congruent LiNbO₃ crystalline AOF of 6.3 cm length at the optical wavelengths 405 nm and 440 nm, which confirm our theoretical predictions and numerical estimations. The performed analysis and preliminary experimental data can be considered like a step in creating an advanced collinear LiNbO₃ acousto-optical filter for astrophysical spectroscopy in the near ultraviolet with significantly improved high spectral resolution. These results can be potentially used practically for accurate spectroscopic observations of astronomical targets.

Two-phonon acousto-optical interaction

Principally new features of square-law nonlinearity peculiar to the non-collinear two-phonon acousto-optical interaction governed by elastic waves of finite amplitude in birefringent crystals are revealed and studied. An additional degree of freedom represented by the dispersive birefringence factor, which can be distinguished within this nonlinear phenomenon, is found and characterized. This physical degree of freedom gives us a one-of-a-kind opportunity to apply the two-phonon acousto-optical interaction in practice for the first time.

The formerly identified additional degree of freedom, unique to this regime, is exploited for designing the cell with an eye to doubling the resolution due to two-phonon processes. We clarify the role of varying the central acoustic frequency and acoustic attenuation using that degree of freedom. Then, the efficiency of calomel is exploited to expand the cell's bandwidth at the cost of its efficiency.

The needed theoretical analysis is developed and proof-of-principle experiments, performed with a specially designed unique wide-aperture acousto-optical cell made of the calomel (α - Hg_2Cl_2) single crystal, are presented. The achieved spectral resolution 0.205 \AA at 405 nm and the resolving power $19,800$ are the best to our knowledge for acousto-optical spectrometers dedicated to space or airborne operations.

Here, in addition, we present an advanced analytical description of this phenomenon in the amplitude and frequency domains; and what is more, we orient it mainly at the second unit-level maximum. This nonlinearity together with the linear acoustic losses in an acousto-optical cell produces a new effect of nonlinear apodization.

3.1 Introduction

Application of the non-collinear acousto-optical interaction (AOI) to optical spectrum analysis had given rise to the non-collinear acousto-optical filters (AOFs) that have been in constant improvement since their appearance in late 1960s. Unlike the collinear AOFs, which are very restricted to a spectrum of available crystalline materials where the collinear AOI exists, the non-collinear AOFs can work within several optically anisotropic materials. From the beginning, the most desirable material for designing the non-collinear AOFs was tellurium dioxide (TeO_2). This crystal is characterized by extremely low acoustic velocity associated with the slow shear elastic mode passing along the $[110]$ -axis. This fact, together with moderate refractive indices and photo-elastic constant, produces a very high acousto-optical figure of merit M_2 [3.1]. In spite of rather large acoustic losses, which usually accompany slow elastic modes in crystals, exploiting the TeO_2 -crystals makes it possible to achieve up to 100% operating efficiency at quite reasonable acoustic power densities. The spectral resolution of about 20 \AA at an optical wavelength of $\lambda = 633 \text{ nm}$ had been achieved with an efficiency of 96% and an interaction length of $\sim 50 \text{ mm}$ [3.2]. Together with this, the spectral resolution of $\sim 4 \text{ \AA}$ at the same wavelength had been predicted for that crystal with the optimized design [3.2]. Nowadays, even commercial TeO_2 -based AOFs can achieve a spectral resolution 3.2 \AA at $\lambda = 633 \text{ nm}$ with an efficiency higher than 50% [3.3]. Recently, studies for imaging purposes have exploited the tellurium dioxide for theoretical analysis in order to compensate the optical dispersion in a non-collinear filter to obtain better performances using the optical activity inherent in the TeO_2 crystal [3.4].

In recent years, the potassium dihydrophosphate (KDP) crystal had been investigated as a more profitable material for the non-collinear AOFs. This material is suitable for ultraviolet wavelengths thanks to its wide transmission range. Due to the photo-elastic tensor properties of KDP, similar AOFs have to use the slow shear elastic mode passing along a direction tilted by a few degrees to the [100]-axis, which is associated with a higher effective photo-elastic constant increasing the figure of merit. The KDP crystal is one of the most progressive materials for non-collinear AOFs in the middle to near-ultraviolet range. The KDP-based non-collinear AOFs promise significantly better performances than the existing α -quartz-based collinear AOFs that are the most widely used and the most appropriate AOFs for the ultraviolet [3.5]. In particular, the KDP-crystal has a figure of merit M_2 four times higher than α -quartz crystal [3.6]. Past year, it has been reported that the KDP-based non-collinear AOF has been improved by enhancing the angular aperture of this AOF and achieving a spectral resolution of 2.5 Å at $\lambda = 205$ nm [3.7].

Together with this, the mercurous chloride or calomel (α - Hg_2Cl_2) crystal is another promising material for acousto-optical devices. This material has tetragonal symmetry, anomalously small acoustic velocity for the slow shear elastic mode passing along the [110]-axis (being almost 2 times lower than in tellurium dioxide), large refractive indices and birefringence, and promises a really high figure of merit M_2 . Initially, the acousto-optic properties of small-size samples of this material had been studied in 1976, and later crystals of about 50 mm long were investigated [3.8]. The longitudinal acoustic mode (in several directions) can be exploited as well, but the figure of acousto-optical merit of such configuration is not as great as for the slow shear mode [3.9]. Currently, we have designed an innovative acousto-optical cell (AOC), based on this previously underrated material, for the frontline of information technology.

The main goal of our investigations is to reveal novel physical details inherent in the nonlinearity of a non-collinear two-phonon AOI controlled by elastic waves of finite amplitude, to investigate features of this nonlinearity both theoretically and experimentally in wide-aperture crystals with moderate linear acoustic attenuation, and to consider an opportunity for parallel optical spectrum analysis with the significantly improved spectral resolution. Studying the local unit-level maxima in the distribution of light scattered into the second order, which appear periodically as the power density of elastic waves grows, makes it possible to identify a variety of the transfer function profiles peculiar to these maxima in the isolated planes of angular-frequency mismatches. Availability of similar maxima gives us an opportunity to choose the desirable profile for the transfer function at the fixed angle of incidence for the incoming light beam with a wide optical spectrum.

Then, we find that non-collinear two-phonon processes of AOI are nearly 100% efficient at the fixed optical wavelength for various acoustic frequencies as well as with the fixed acoustic frequency for various optical wavelengths due to the existence of an additional dispersive birefringence factor that can be distinguished within this non-linear phenomenon. However, the first option with the fixed optical wavelength cannot be used for linear spectrum analysis of radio-wave signals principally owing to the existence of a strongly non-linear dependence between the incoming electronic signal, i.e. the acoustic waves of finite amplitude in an AOC, and the scattered light waves. In contrast, under the same conditions a dependence of the scattered light waves on the incident light is nevertheless linear within the nonlinear non-collinear two-phonon AOI, which can also double the spectral resolution. Therefore, in view of developing a new approach to parallel spectrum analysis of wide-spectrum optical signals with significantly improved resolution, we choose the second option with the fixed acoustic frequency, see Fig. 3.1, which gives us an opportunity to propose a pioneer practical application of the non-collinear two-phonon AOI for the first time to our knowledge. Generally speaking, potential spectral resolution of spectrometers exploiting the non-collinear AOC includes ordinary birefringence of a crystal as a basic parameter of the chosen material, which determines its possibilities.

In applying this new approach, we demonstrate an opportunity to replace the physically limited birefringence of a crystal by that significantly larger birefringence factor, inherent in the non-collinear two-phonon AOI. Moreover, it can be done together with doubling the spectral resolution, which is peculiar to the non-collinear two-phonon AOI in principle, as shown in Fig. 3.1. These possibilities are demonstrated theoretically for the crystals of tetragonal symmetry as examples and confirmed during the experiments with a specially designed unique wide-aperture AOC using the calomel ($\alpha\text{-Hg}_2\text{Cl}_2$) single crystal and governed by elastic waves of finite amplitude.

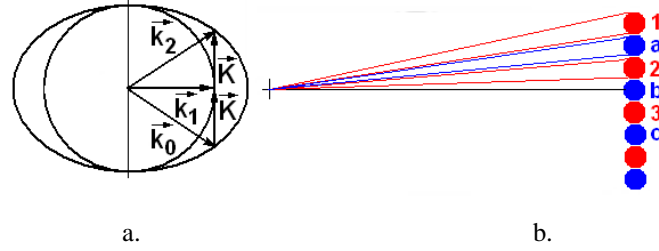


Fig. 3.1. The non-collinear two-phonon AOI vector diagram: (a) and doubling the spectral resolution (b). Spots 1,2,3,... are related to one-phonon processes, while additional spots a,b,c,... describe refining the resolution caused by the appearance of a two-phonon interaction.

3.2 Non-collinear two-phonon interaction

Strongly nonlinear behavior of optical components with the Bragg AOI in an anisotropic medium can be achieved easily in usual experiments without any observable influence of the scattering process on the acoustic wave. In this case the amplitude of the acoustic wave is governed by a homogeneous wave equation in so-called weak coupling regime [3.10]. Let us assume that the area of propagation for the acoustic wave, traveling almost perpendicularly to the light beams, is bounded by two planes $x = 0$ and $x = L$ in a uniaxial crystal, taking into account both angular and frequency mismatches in the wave vectors. Usually, the Bragg acousto-optical processes include three-waves: the incident and scattered light modes as well as an acoustic mode, and incorporates conserving both the energy and the momentum for each partial act of a one-phonon AOI [3.11]. However, at certain incident angles of light shining on selected crystal cuts and at a fixed frequency of the acoustic wave, one can observe Bragg scattering of light caused by the participation of two phonons, so that the conservation laws are given by $\nu_1 = \nu_0 + f$, $\vec{k}_1 = \vec{k}_0 + \vec{K}$, $\nu_2 = \nu_0 + 2f$, and $\vec{k}_2 = \vec{k}_0 + 2\vec{K}$ simultaneously (ν_m , \vec{k}_m and f , \vec{K} are the frequencies and wave vectors of light and acoustic waves, $m = 0, 1, 2$), see Fig. 1a. Such a four-wave process occurs at the frequency f_0 of the acoustic wave, exactly peculiar to a two-phonon AOI, which can be determined from [3.12]

$$f_0 = \lambda^{-1} V b, \quad (3.1)$$

where $b = \sqrt{|n_0^2 - n_1^2|}$ is remarkably dispersive birefringence factor and $n_0 \neq n_1$ are the current refractive indices of a crystal, V is the ultrasound velocity, λ is the incident light wavelength. The polarization of light in the zero and second orders is orthogonal to the polarization in the first order; whereas the frequencies of the light beams in the first and second orders of scattering are shifted by f_0 and $2 f_0$, respectively, with reference to the zero order due to the Doppler frequency shift.

A set of equations for the complex amplitudes $C_m(x)$ of light waves ($m = 0, 1, 2$), appearing due to a quasi-stationary two-phonon Bragg AOI governed by acoustic waves of finite amplitude, is given by [3.12]

$$\begin{aligned}
\text{a) } \frac{dC_0}{dx} &= -\sigma C_1 \exp(-i\eta_0 x), \\
\text{b) } \frac{dC_1}{dx} &= \sigma [C_0 \exp(i\eta_0 x) - C_2 \exp(-i\eta_1 x)], \\
\text{c) } \frac{dC_2}{dx} &= \sigma C_1 \exp(i\eta_1 x),
\end{aligned} \tag{3.2}$$

where x is the coordinate along light propagation. The combined effect of factors expressing both the acousto-optical material efficiency and the acoustic power is described by $\sigma = \pi (\lambda \cos \theta)^{-1} \sqrt{M_2 P/2}$; θ is the angle of incidence for an external plane light wave, M_2 is the figure of acousto-optical merit, and P is the acoustic power density. A square-law nonlinearity exists that is connected to the products $C_m P^{1/2}$ on the right sides of Eq.(3.2). The constant angular-frequency mismatches $\eta_m = k_{m,x} - k_{m+1,x}$ are explained in terms of x -components for light wave vectors. We analyze Eq.(2) with the simplest boundary conditions $|C_0(x=0)|^2 = I$, $C_{1,2}(x=0) = 0$ and exploit the conservation law $|C_0|^2 + |C_1|^2 + |C_2|^2 = I$, resulting from Eq.(3.2), where I is the intensity of the incident continuous-wave light beam.

Now, we assume the precise angular alignment of the incident light and expand η_0 and η_1 into series in terms of powers of only the frequency detuning $|f - f_0|$ for the current acoustic frequency f relative to the frequency $f_0 = \Omega_0 / (2\pi)$. In the second order approximation, one can obtain from the diagram of wave vectors that $\eta_0 \approx \pi \lambda n_1^{-1} V^{-2} |f - f_0|^2$ and $\eta_1 \approx \pi \lambda n_0^{-1} V^{-2} (4 f_0 |f - f_0| + 7 |f - f_0|^2)$ [3.12] with $n_0 < n_1$. Therefore, in the first order approximation we may put $\eta_0 \approx 0$ and $\eta \approx \eta_1 \approx 4\pi \lambda n_0^{-1} V^{-2} f_0 |f - f_0|$. After that, one can put $S_{0,1} = C_{0,1}$, $S_2 = C_2 \exp(-i\eta x)$ and rewrite Eq.(3.2) as

$$\begin{aligned}
\text{a) } \frac{dS_0}{dx} &= -\sigma S_1, & \text{b) } \frac{dS_1}{dx} &= \sigma (S_0 - S_2), & \text{c) } \frac{dS_2}{dx} &= \sigma S_1 - i\eta S_2.
\end{aligned} \tag{3.3}$$

Now, the corresponding boundary conditions are

$$S_0(x=0) = 1, \quad S_{1,2}(x=0) = 0. \tag{3.4}$$

This set of the combined first-order differential equations can be converted into a triplet of equations of the third-order for complex amplitudes S_m , and these equations are independent from one another. In the case of $d\sigma/dx = 0$, these equations reduce to one describing all the light waves

$$\frac{d^3 S_m}{dx^3} + i\eta \frac{d^2 S_m}{dx^2} + 2\sigma^2 \frac{dS_m}{dx} + i\eta \sigma^2 S_m = 0. \tag{3.5}$$

The general solution for the complex amplitude S_2 is

$$S_2 = \frac{\sigma^2 \exp(a_1 x)}{(a_1 - a_2)(a_1 - a_3)} - \frac{\sigma^2 \exp(a_2 x)}{(a_1 - a_2)(a_2 - a_3)} + \frac{\sigma^2 \exp(a_3 x)}{a_1 a_2 - a_1 a_3 - a_2 a_3 + a_3^2}; \tag{3.6}$$

where a_k , ($k = 1, 2, 3$) are the roots of the characteristic equation $a^3 + i\eta a^2 + 2\sigma^2 a + i\eta \sigma^2 = 0$ for Eq.(3.5). This solution leads to a 3D-distribution $|C_2|^2 = |S_2(\sigma x, \eta x)|^2$, expressed in terms of 2 dimensionless parameters σx and ηx , describing the acoustic power density and the angular-frequency mismatch, respectively, see Fig. 3.2. This plot demonstrates a specific square-law acousto-optical nonlinearity inherent in the non-collinear two-phonon AOI governed by elastic waves of finite amplitude. Moreover, Fig. 3.3 exhibits a sequence of unit-level maxima that are often desirable for potential practical applications, particularly to the spectrum analysis of optical signals. The first quartet of maxima is placed at the points $(\sigma x)_1 \approx 2.22$, $(\sigma x)_2 \approx 6.66$, $(\sigma x)_3 \approx 11.11$, and $(\sigma x)_4 \approx 15.55$. At these points, one can obtain four particular profiles in terms of the dimensionless angular-frequency mismatch ηx , see Fig. 3.4.

Then, plots in Fig. 3.4 also demonstrate an influence of specific acousto-optical square-law nonlinearity and show that the second maximum in Fig. 3.3 already gives close to the widest bandwidth of a two-phonon AOI at a reasonably high acoustic power parameter $(\sigma x)_2 \approx 6.66$. Consequently, exactly this maximum with a two-side variation of the dimensionless mismatch about $\Delta\eta = (\eta x)_+ + (\eta x)_- \approx 4\pi$ at the half-maximum level can be selected as the most appropriate one for realizing a wide-bandwidth two-phonon AOI. In the case of exact angular alignment, the mismatch η is only achieved by the frequency detuning $|f - f_0|$, so that, as it is seen directly from Eq.(2), $\eta = 2\pi |f - f_0| / V$. With $x = L$, the second profile from Fig. 4 leads to $\Delta\eta \approx 2\eta \approx 4\pi / L$, so that the frequency bandwidth for the second maximum is given by

$$\Delta f = 2 |f - f_0| \approx n_0 V^2 / (\lambda L f_0). \quad (3.7)$$

Here, the length L of AOI, the current frequency f_0 , and the optical wave length λ have to provide the Bragg regime of AOI.

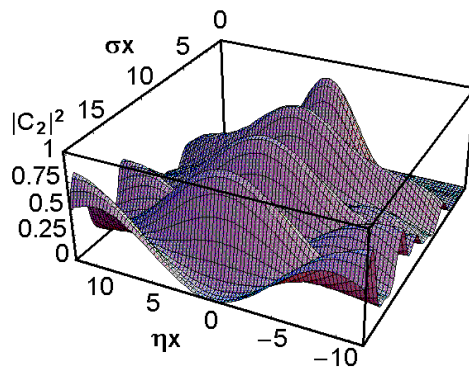


Fig. 3.2. A 3D-bandshape for the non-collinear two-phonon AOI; the axis σx (the dimensionless acoustic power density) reflects nonlinearity of the phenomenon, ηx is the dimensionless angular-frequency mismatch.

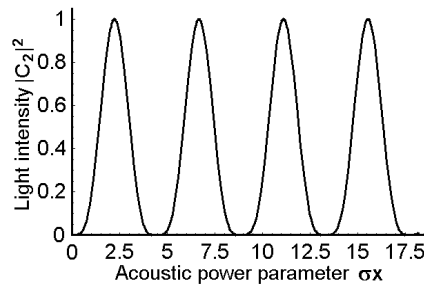


Fig. 3.3. Maxima of the non-collinear two-phonon AOI reflecting its strongly non-linear behavior along the line $\eta x = 0$.

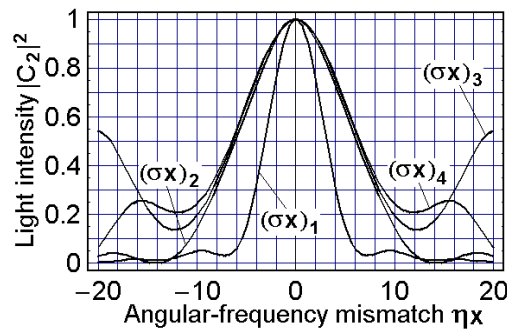


Fig. 3.4. The intensity – mismatch profiles related to first four maxima of the non-collinear two-phonon AOI.

3.3 α -Hg₂Cl₂ acousto-optical cell characterization

3.3.1 Frequency and length

To make more concrete our consideration an appropriate acousto-optically effective crystalline material will be selected for further analysis. During the selection of a similar appropriate material, a few possibilities of exploiting either longitudinal L or shear S elastic modes passing along various directions had been preliminarily estimated. In particular, the subjects of our attention were the modes L[001] and S[110] in rutile (TiO₂), S[100] in lithium niobate (LiNbO₃), L[100] and S[110] in calomel (α -Hg₂Cl₂). They allow the non-collinear two-phonon AOI and can be considered as desirable alternatives operating at rather different acoustic frequencies. The analysis has shown that the best option for further experiments, motivated by very high efficiency of AOI and not too high acoustic frequency, is the calomel single crystal. This crystal belongs to the 4/mmm-tetragonal symmetry group, has spectral transmission band $\Delta\lambda = 0.38 - 28 \mu\text{m}$ and the material density $\rho \approx 7.2 \text{ g / cm}^3$ [3.13]. It has a pair of dispersive refractive indices, whose main values are $N_O = 1.9634$ and $N_E = 2.6217$ at the wavelength $\lambda = 633 \text{ nm}$. Then, in particular, this crystal allows at least two pure elastic modes, namely, the slow shear mode with the wave vector $\vec{K} \parallel [110]$, the displacement vector $\vec{u} \parallel [1\bar{1}0]$, the phase velocity $V_{SS} \approx 0.347 \times 10^5 \text{ cm/s}$, and the acoustic wave attenuation factor $\Gamma \approx 230 \text{ dB / (cm GHz}^2 \text{)}$. There is also the longitudinal mode with $\vec{K} \parallel \vec{u} \parallel [100]$, $V_L \approx 1.622 \times 10^5 \text{ cm/s}$, and $\Gamma \approx 12.5 \text{ dB / (cm GHz}^2 \text{)}$. It is important to note that both these elastic modes are potentially suitable for effective non-collinear two-phonon AOI.

Now, we make the new step of studying the nonlinearity of non-collinear two-phonon AOI, see Fig. 3.5. This step can be represented for the corresponding processes of scattering in terms of two surfaces for the refractive indices of ordinary (see the internal dark sphere) and extraordinary (see the external faint ellipsoid) light waves for a tetragonal crystal at the fixed optical wavelength λ (here, the calomel crystal at $\lambda = 633 \text{ nm}$ is taken as an example with $N_E \geq N_O$). The sizes of both sphere and ellipsoid will be varied depending on λ due to remarkable dispersion of the crystalline material within potential optical range. The vertical axis in Fig. 3.5 is oriented along the optical axis [001] of a crystal, while orientation for a pair of the horizontal axes depends on the chosen elastic modes.

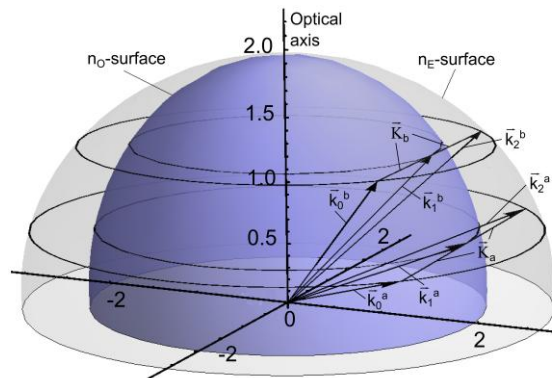


Fig. 3.5. Two examples of vector diagrams, indexed by “a” and “b”, inherent in nonlinear two-phonon AOI with the fixed ratio V / λ . The extraordinary refractive index n_E is described by an external faint ellipsoid, while a darker internal sphere shows the ordinary refractive index $n_O \equiv N_O$. Here, $\vec{k}_m^{a,b}$ and $\vec{K}_{a,b}$ are the wave vectors of light and acoustic waves.

For the calomel crystal, in particular, they can be taken as [110] and [11, $\bar{0}$] for the slow shear mode or as [100] and [010] for the longitudinal mode. Then, in either case, this figure includes a pair of vector diagrams illustrating two opportunities for two-phonon AOI through various angles, which use different acoustic frequencies and birefringence factors b . Two triplets of

vectors, going from the geometric center of surfaces, represent the optical wave vectors describing the corresponding orders of AOI, whereas sequential pairs of the acoustic wave vectors reflect two-phonon processes. The upper vector diagram in Fig. 3.5 corresponds to smaller birefringence, i.e. to smaller factor b , and lower acoustic frequency f_0 (i.e. shorter vectors \vec{K}) than the other vector diagram depicted lower, operating by larger factor b and higher acoustic frequency f_0 (i.e. longer vectors \vec{K}). Thus these plots reflect the existence of an additional physical degree of freedom inherent in the nonlinearity of the two-phonon AOI. This degree of freedom permits the fixed frequency f_0 to exert control over various optical wavelengths scattered through different angles. In this case, one has to consider two pairs of surfaces peculiar to the refractive indices of ordinary and extraordinary light waves for a tetragonal crystal and each similar pair of surfaces will correspond to an individual light wavelength. Nevertheless, the corresponding vector diagrams for two different nonlinear processes of two-phonon AOI will include acoustic vectors \vec{K} of the same lengths characterizing the same acoustic frequency f_0 .

Calomel is a uniaxial crystal, so that $n_o \equiv N_o$ is the main refractive index for the ordinary state of polarization, while n_e depends on a direction in a crystal and has the form of an ellipsoid. We are interested in rather small tilts from the [001]-axis. Therefore, one can consider the angle $\psi \in [0, \pi/2]$ of a tilt from the [001]-axis. Considering the geometry yields

$$n_e^2 = \frac{N_E^2 N_O^2 (1 + \tan^2 \psi)}{N_E^2 + N_O^2 \tan^2 \psi} \geq n_o^2 \equiv N_o^2 . \quad (3.8)$$

Substituting Eq.(3.8) into Eq.(3.1), one can obtain

$$\psi [rad] = \arctan \left[\frac{\lambda f_0 N_E}{N_o \sqrt{V^2 (N_E^2 - N_o^2) - \lambda^2 f_0^2}} \right] . \quad (3.9)$$

Then, within designing an AOC based on a crystal with moderate acoustic losses and under the action of the acoustic wave of finite amplitude, the spectral resolution $\delta\lambda_0$ of potential dispersive component based on similar AOC can be estimated as

$$\delta\lambda_0 = \lambda^2 / (2bD) . \quad (3.10)$$

This value does not include any parameters of the acoustic wave and, besides the optical aperture D , depends only on the birefringence factor b peculiar to a crystal and the incident light wavelength λ . The desirable aperture D in Eq.(3.10) has to be chosen to satisfy a few requirements depending on a set of various physical factors, the main one is the acoustic attenuation. If an acceptable level of acoustic losses per optical aperture D is B [dB/aperture], one can write that $D = B / (\Gamma f_0^2)$. From these formulas, one can find the denominator in Eq.(3.10) to be

$$2bD = \frac{2\lambda B}{V\Gamma f_0} . \quad (3.11)$$

Restricting ourselves to the level $B \equiv 6\text{dB/aperture}$ and using the above-mentioned data for the two chosen pure elastic modes in calomel, one can obtain for $\lambda = 405$ nm and 633 nm (see in the following plots shown in Figs. 3.6 and 3.7).

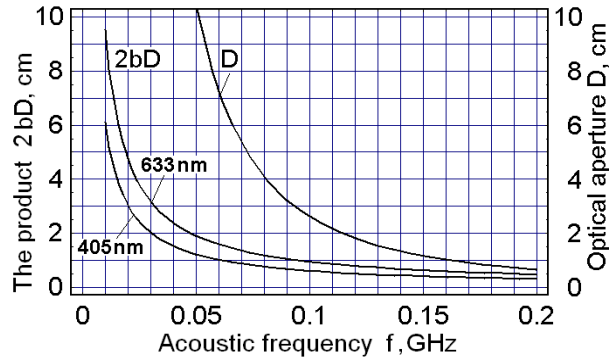


Fig. 3.6. The product $2bD$ and the desirable aperture D , connected with the spectral resolution, for the slow shear elastic mode in calomel.

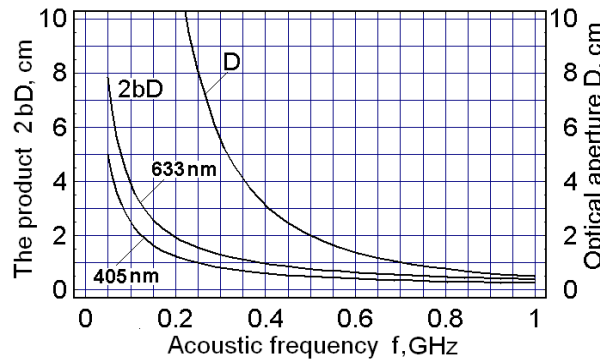


Fig. 3.7. The product $2bD$ and the desirable aperture D , connected with the spectral resolution, for the longitudinal elastic mode in calomel.

Before we analyze these diagrams further, we motivate the above-taken selection of the level $B = 6$ dB for acoustic losses per optical aperture. As such, we attempt to describe shaping the resolvable spot after an AOC in a spectrum analyzer. The normalized distribution $I(u)$ of light intensity of that individual resolvable spot is given by

$$I(u, \alpha_0) = \frac{\sin^2(\pi u) + \sinh^2(\alpha_0/2)}{[1 + (2\pi u/\alpha_0)^2] \sinh^2(\alpha_0/2)}, \quad (3.12)$$

where $u = wD/\lambda F$; w is the physical spatial coordinate in the focal plane, F is the focal distance of the integrating lens, and $\alpha_0 = \alpha D$ is the acoustic loss factor per aperture. Analysis of Eq. (3.12) shows that $\alpha_0 \equiv B = 6$ dB / aperture gives the first zero in the distribution $I(u)$ at a level about -20 dB. Choosing $B = 6$ dB allows us to avoid unnecessarily strong limitations for this stage of studies. Together with this, the main lobe in the distribution $I(u)$ will be almost no widened at $B = 6$ dB / aperture.

3.3.2 Efficiency

Obtaining the figure of acousto-optical merit M_2 inherent in the selected cut of an α - Hg_2Cl_2 crystal first requires finding the effective photo-elastic constant p_{eff} . To do so, keep in mind that each dynamic acoustic grating can be characterized by its symmetric deformation tensor of the second rank $\gamma = (\vec{u} \cdot \vec{q} + \vec{q} \cdot \vec{u})/2$, where $\vec{q} = \vec{K}/|K|$ is the unit vector of the wave normal.

The case of the slow shear elastic mode with $\vec{K} \parallel [110]$, $\vec{u} \parallel [1\bar{1}0]$

Due to $\vec{q} = (1,1,0)/\sqrt{2}$ and the normalized displacement vector is $\vec{u} = (1,-1,0)/\sqrt{2}$, the corresponding deformation tensor takes the following dyadic form

$$\gamma^{(S)} = 0.5 \{ (\bar{x}_1 \bullet \bar{x}_1) - (\bar{x}_2 \bullet \bar{x}_2) \}. \quad (3.13)$$

The tensor $\gamma^{(S)}$ of the second rank with the components $\gamma_{kl}^{(S)}$ ($k, l = 1, 2, 3$) in the basis $(\bar{x}_1, \bar{x}_2, \bar{x}_3)$ can be converted into a 6-dimension vector $\bar{\gamma}^{(S)} = (1, -1, 0, 0, 0, 0)$ [3.14]. To estimate the efficiency of AOI associated with the above selected slow shear acoustic mode, the photo-elastic tensor p of the fourth rank should be converted into the form of a 6×6 matrix with the components $p_{\lambda\mu}$. For $\alpha\text{-Hg}_2\text{Cl}_2$ ($4/mmm$), the matrix representation for the tensor p gives the following non-zero components: $p_{11} = p_{22} = 0.551$, $p_{12} = p_{21} = 0.44$, $p_{13} = p_{23} = 0.256$, $p_{31} = p_{32} = 0.137$, $p_{33} = 0.1$, $p_{44} = p_{55}$ - unknown, and $p_{66} = 0.047$ at $\lambda = 633$ nm [3.15]. Now, one can calculate the matrix product $p \bar{\gamma}^{(S)} = 0.5 (p_{11} - p_{12}) (1, -1, 0, 0, 0, 0)$ and convert it back to the form of a standard tensor ($p \gamma^{(S)}$) of the second rank [3.14]. The effective photo-elastic constant can be written from the scalar form $p_{eff}^{(S)} = \bar{e}_1 (p \gamma^{(S)}) \bar{e}_0$; i. e.

$$p_{eff}^{(S)} = 0.5 (p_{11} - p_{12}) \bar{e}_1 [(\bar{x}_1 \bullet \bar{x}_1) - (\bar{x}_2 \bullet \bar{x}_2)] \bar{e}_0, \quad (3.14)$$

where the vectors \bar{e}_0 and \bar{e}_1 usually describe the polarization states of incident and scattered light beams, respectively. Within the anomalous non-collinear AOI the eigen polarization vectors \bar{e}_0 and \bar{e}_1 of the incident and scattered light beams should be orthogonal to one another $\bar{e}_0 \perp \bar{e}_1$, and they both should also be lying in the same plane as the wave vector $\vec{K} \parallel [110]$.

For the sake of simplicity, in this case, one can take $\bar{e}_0 \parallel \vec{K}$ and $\bar{e}_1 \parallel \vec{u}$, i.e. $\bar{e}_0 = (1, 1, 0) / \sqrt{2}$ and $\bar{e}_1 = (1, -1, 0) / \sqrt{2}$. Then, one can obtain $(p \gamma^{(S)}) \cdot \bar{e}_0 = 2^{3/2} (p_{11} - p_{12}) (1, -1, 0)$ and find

$$p_{eff}^{(S)} = \bar{e}_1 (p \gamma^{(S)}) \bar{e}_0 = 0.5 (p_{11} - p_{12}) \approx 0.055. \quad (3.15)$$

The corresponding figure of acousto-optical merit M_2 also depends on the material density $\rho = 7.2$ g/cm³ and a pair of rather dispersive refractive indices. Using, for instance, $n_o = 1.9634$ and $n_E = 2.6217$ at $\lambda = 633$ nm, one can find $M_2^{(S)} = n_o^3 n_E^3 (p_{effmax}^{(S)})^2 / (\rho V_{SS}^3) \approx 1371 \times 10^{-18}$ s³/g. This value demonstrates that the anomalous regime of AOI governed by the pure slow shear acoustic mode in the calomel single crystal is very efficient and is able to provide an effective two-phonon AOI.

3.3.3 Resolving power

In physical optics, the resolving power (RP) is expressed usually as the ratio $R = \lambda / \delta\lambda$ [16], where λ is the incident light wavelength and $\delta\lambda$ is the spectral resolution. It is one of the most important parameters peculiar to various dispersive optical components, including both traditional static diffraction gratings and AOCs, representing dynamic diffraction gratings. Besides that, the RP of a static diffraction grating can be characterized by the product $R = |v| N$, where v is the order of diffraction and N is a number of the lighted slits. In fact, N includes the lighted aperture d [mm] of that grating and the slit density S [lines/mm] because of $N = S d$. Combining these simple formulas, one arrives at

$$\delta\lambda = \lambda / (|v| S d) = \lambda / (|v| N). \quad (3.16)$$

In acousto-optics, the RP of an AOC as the dynamic diffraction grating depends significantly on the chosen regime of light scattering. The key value here is a number of the lighted slits, which has various determinations caused by a regime. The non-collinear two-phonon light scattering occurs at the acoustic wave frequency f_0 [3.12], specific to the needed central optical wavelength λ_0 , so that one can write

$$f_0 = V b / \lambda_0, \quad (3.17)$$

where $b = \sqrt{|n_0^2 - n_1^2|}$ is the birefringence factor, $n_0(\lambda) \neq n_1(\lambda)$ are the current refractive indices of a crystal. Thus, the number of slits N can be expressed as $N = D f_0 / V$, where the ratio f_0 / V describes the inverted acoustic wavelength, which is an analogue of the slit density. Substituting this formula into Eq.(3.16), one yields

$$\delta\lambda = V\lambda_0 / (|v| D f_0) . \quad (3.18)$$

Then, using Eq.(3.17), one will have $\delta\lambda = \lambda_0^2 / (|v| b D)$. Therefore, in an acoustically low-loss case with $|v| = 2$ peculiar to the non-collinear two-phonon light scattering, the spectral resolution takes the form

$$\delta\lambda = \lambda_0^2 / (2b D) . \quad (3.19)$$

There are a few factors limiting the RP of an AOC, which can be represented as functions of the central optical wavelength λ_0 inherent in the chosen regime of light scattering. The first of them is directly follows from Eq.(3.19) in the form

$$R_1 \leq 2b D / \lambda_0 , \quad (3.20)$$

where the optical aperture D serves as a parameter.

Then, the acoustic beam divergence, as it is passing through the light beam, is under the second geometrical limitation for the RP. Physically, it is the requirement upon the piezoelectric transducer to operate in the acoustic Fresnel zone restricting the acoustic beam divergence. This limitation couples the piezoelectric transducer length L (that represents the length of acousto-optical interaction in fact) with the distance from that transducer to the point of half power level in the near-field zone of the acoustic waves. Practically, this distance is equivalent to the optical aperture D , so that one can write $D = L^2 f_0 / (2V)$. Substituting the last expression for D together with Eq.(3.17), into Eq.(3.20), one yields

$$R_2 \leq \frac{2b L^2 f_0}{\lambda_0 2V} = \frac{b^2 L^2}{\lambda_0^2} . \quad (3.21)$$

The third limitation is connected with the linear acoustic attenuation. It can also be represented as a function of the central optical wavelength. If the level of acoustic attenuation B [dB] per the optical aperture D of a cell is acceptable, the size of allowable optical aperture is equal to $D \leq B \Gamma^{-1} f_0^{-2}$. Substituting this formula into Eq.(3.20) and using Eq.(3.17), one arrives at the following expression

$$R_3 \leq \frac{2B [dB] \lambda_0 [\mu m] \times 10^{14}}{b \Gamma [dB/(cm \cdot GHz^2)] (V [cm/s])^2} . \quad (3.22)$$

Thus a triplet of the above-mentioned independent limitations restricts the RP of an AOC. In the particular case of a two-phonon light scattering, one can take a set of rather effective and available materials. However, one can see from Eqs.(3.14) – (3.16) that these limitations for the RP always include the ratio b/λ_0 , i.e. their spectral dependencies are determined by a behavior of the dispersive birefringence factor b inherent in a material. Because of Eq.(3.17) gives the expression $b/\lambda_0 = f_0/V$, the obtained limitations can be expressed in the same terms as

$$\text{a) } R_1 \leq \frac{2f_0 D}{V} , \quad \text{b) } R_2 \leq \frac{f_0^2 L^2}{V^2} , \quad \text{c) } R_3 \leq \frac{2B [dB] \times 10^7}{\Gamma [dB/(cm \cdot GHz^2)] f_0 [MHz] V [cm/s]} . \quad (3.23)$$

Equations (3.23) demonstrate that the RP of an AOC depends significantly on the chosen acoustic frequency. An acceptable size of the aperture D depends on various physical factors, the most important of which is the acoustic attenuation.

Now, we are coming to principally new step in studying the nonlinearity of non-collinear two-phonon AOI [3.17], see Fig. 3.8. This step can be represented for the corresponding processes of scattering in terms of two surfaces for the refractive indices of ordinary (see the internal dark sphere) and extraordinary (see the external faint ellipsoid) light waves for a tetragonal crystal at the fixed optical wavelength λ_0 (here, the calomel crystal is taken as an example with $N_E \geq N_O$). The sizes of both sphere and ellipsoid will be varied depending on λ_0 due to remarkable dispersion of the crystalline material within potential optical range. The vertical axis in Fig. 3.8 is oriented along the optical axis [001] of that crystal, while orientation for a pair of the horizontal axes depends on the chosen elastic modes. For the calomel crystal, in particular, they can be taken as [110] and $[1\bar{1}0]$ axes for the slow shear mode. Then, this figure represents the vector diagram, illustrating an opportunity for the two-phonon light scattering through various angles; which includes an optimal acoustic frequency with the birefringence factor b adequate to the chosen λ_0 . A triplet of vectors, going from the geometric center of surfaces, represents the optical wave vectors describing the corresponding orders of light scattering, whereas a pair of the sequential acoustic wave vectors \vec{K} reflects the two-phonon process. The tilt angle ψ characterizes an angle between the optical axis and the geometrical plane including all the optical and acoustic wave vectors. The availability of the angle ψ reflects the existence of an additional physical degree of freedom inherent in the nonlinearity of the two-phonon light scattering. This degree of freedom permits the fixed frequency f_0 to exert control over various optical wavelengths scattered through different angles. In this case, one has to consider two pairs of surfaces peculiar to the refractive indices of ordinary and extraordinary light waves for a tetragonal crystal and each similar pair of surfaces will correspond to an individual light wavelength.

Calomel is a uniaxial crystal, so that $n_O \equiv N_O$ is the main refractive index for the ordinary state of polarization whose 3D-distribution is a sphere. The refractive index n_E for the extraordinary polarization ($n_E < n_O$) depends on a direction of light propagation in a crystal, and its 3D-distribution has the form of an ellipsoid. We are interested in rather small tilts from the [001]-axis, therefore, one can consider the angle $\psi \in [0, \pi / 2]$ of a tilt from the [001]-axis. Considering the geometry yields and using Eq.(3.17), one can obtain

$$\tan \psi = \frac{\lambda_0 f_0 N_E}{N_O \sqrt{V^2 (N_E^2 - N_O^2) - \lambda_0^2 f_0^2}}. \quad (3.24)$$

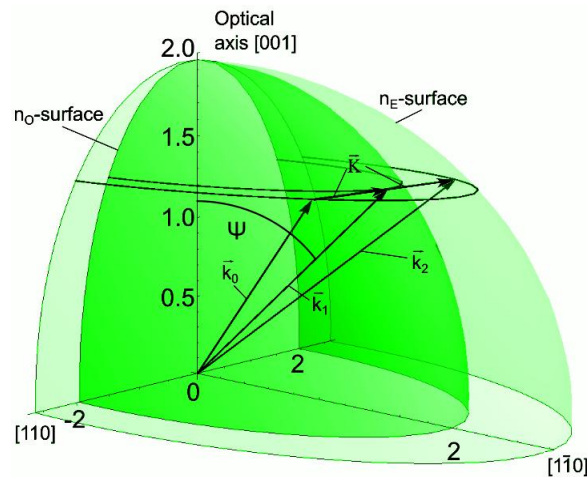


Fig. 3.8. The vector diagram for two-phonon light scattering in calomel where ψ is the tilt angle.

Now, keeping in mind requirements of the best achievable spectral resolution and resolving power, the detailed analysis can be performed proceeding from the optical aperture D of the AOC, restricted by an available sample of the chosen crystalline material with the given factor Γ of acoustic attenuation. Taking the above-motivated value B dB/aperture, one can find the

central frequency for a two-phonon light scattering as $f_0 = \sqrt{B/(\Gamma D)}$. Then, the chosen calomel crystal gives the fixed acoustic velocity $V = 0.347 \times 10^5$ cm/s and the main refractive indices $N_E(\lambda)$ and $N_O(\lambda)$. The dispersion of main indices in calomel is given by [3.18]

$$\text{a) } N_O = \sqrt{1 + \frac{2.595 \cdot \lambda^2}{\lambda^2 - 0.03648}}, \quad \text{b) } N_E = \sqrt{1 + \frac{2.490 \cdot \lambda^2}{\lambda^2 - 0.08237} + \frac{2.479 \cdot \lambda^2}{\lambda^2 - 0.03803}}, \quad (3.25)$$

where λ must be expressed in micrometers. These indices should be substituted in Eq.(3.24) to explain the current (local) refractive indices n_O and n_E as well as the tilt angle ψ mentioned above at the chosen central frequency f_0 . After that, one has to note that now $b(\lambda) = \sqrt{n_E^2(\lambda) - n_O^2(\lambda)}$, as well as this factor includes the dependence on the frequency f_0 . Using these details, one can come back to estimating the RP as function of aforementioned limitations.

The length L and central frequency f_0 of Bragg acousto-optical interaction in a crystal are restricted by the following well-known inequality for Klein-Cook parameter $Q = 2\pi\lambda L f_0^2 / (n_0 V^2) \gg 1$ [3.19]. In calomel, for the slow shear mode passing along the [110]-axis with $V = 0.347 \times 10^5$ cm/s, and $n_0 = 2.0826$ at $\lambda = 405$ nm, one can find $f_0 = \sqrt{B/(D\Gamma)} \approx 50$ MHz and $L_{\min} \gg 0.0038 Q$ cm. Taking the limiting value $Q = 4\pi$, as it had been recommended in Ref. [19], one yields $L_{\min} \geq 0.05$ cm and can take, for example, $L_{\min} \approx 0.2$ cm with a safety margin. Consequently, with $L \approx 0.2$ cm the central acoustic frequencies $f_0 \geq 50$ MHz can be chosen without any doubts in Bragg character of light scattering.

With choosing $B = 4, 6,$ and 8 dB, one can calculate $f_0 \approx 57.8, 71.0,$ and 82.6 MHz, respectively, from the above-noted formulas for the aperture $D = 5.2$ cm. Then, using Eq.(3.24) together with Eq.(3.25), one can find the magnitudes for $\tan \psi = T(\lambda_0, f_0)$ in calomel; namely, $T(405 \text{ nm}, 57.8 \text{ MHz}) \approx 0.0445$, $T(405 \text{ nm}, 71.0) \approx 0.0546$, $T(405 \text{ nm}, 82.6 \text{ MHz}) \approx 0.0636$, $T(633 \text{ nm}, 57.8 \text{ MHz}) \approx 0.0812$, $T(633 \text{ nm}, 71.0) \approx 0.0995$, and $T(633 \text{ nm}, 82.6 \text{ MHz}) \approx 0.1162$. With these data, one can numerically estimate the limitations restricting the RP for the calomel-based AOC. Applying Eqs.(3.23), one can obtain the frequency dependences presented in Fig. 3.9.

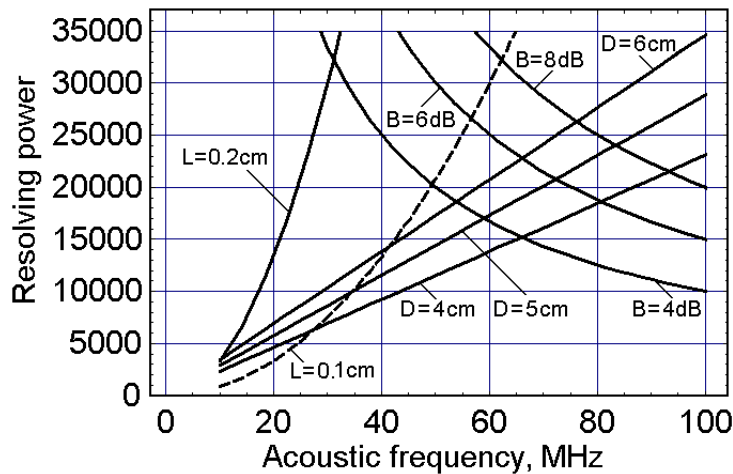


Fig. 3.9. Resolving power of the calomel-based AOC vs. the optical aperture D , the length of acousto-optical interaction L , and the acoustic attenuation parameter B .

It is seen from the plots in Fig. 3.9 that one can expect for the RP the following theoretical estimations: $R(B = 4 \text{ dB}, 57.8 \text{ MHz}) \approx 17000$, $R(B = 6 \text{ dB}, 71 \text{ MHz}) \approx 20000$, and $R(B = 8 \text{ dB}, 82.6 \text{ MHz}) \approx 25000$. Hence, at $\lambda_0 = 405$ nm one yields $\delta\lambda_0 \approx 0.238 \text{ \AA}$ with $B = 4$ dB, $\delta\lambda_0 \approx 0.2025 \text{ \AA}$ with $B = 6$ dB, and $\delta\lambda_0 \approx 0.162 \text{ \AA}$ with $B = 8$ dB, respectively.

3.4 Local analysis of the Two-phonon acousto-optical interaction

3.4.1 First maxima

Within linear acousto-optics, one can use standard approach to estimating the action of linear acoustic attenuation using the Fourier transformation of exponentially falling down distribution at the AOC's output facet. The Fourier transformed signal gives a resolvable spot profile in the focal plane of the integrating lens within classical scheme of spectrum analyzer [3.11]. In so doing, the light intensity profile of a spot gives the main lobe width and level of side lobes characterizing both the resolution and the dynamic range of an optical system. In our case, one should estimate the combined effect provided by acousto-optical nonlinearity and linear acoustic losses in AOC. For this purpose, we compare with one another light distributions $C_2(x, \alpha)$ along coordinate σx in the vicinity of various points $(\sigma x)_1$ peculiar to the first unit-level maxima for a few magnitudes of α . The preliminary analysis has shown that similar light distributions are significantly non-uniform along AOC's aperture, so that the final Fourier transformed signals are not optimal in the focal plane of a lens. This is why those values $(\sigma x)_1$ had been somewhat exceeded with the purpose of making an optimization. The goal of such an optimization consists in achieving as much as possible more symmetrical light distributions at the output facet of an AOC. However, local maximum for each of these output light distributions is slightly shifted from a point corresponding to the middle between two falling down wings of the corresponding distribution.

To make more concrete our consideration an appropriate acousto-optical crystalline material has to be selected for the further analysis. During the selection of a material, a few possibilities of exploiting either longitudinal or shear elastic modes, passing along various crystallographic directions, had been estimated. The analysis has shown that one of the best options for performing experiments, motivated by very high efficiency of scattering and not too high acoustic frequency for excitation, is the calomel (α - Hg_2Cl_2) single crystal. This crystal belongs to the 4/mmm – tetragonal symmetry group. It has spectral transmission band $\Delta\lambda = 0.38 - 28 \mu\text{m}$ and a pair of dispersive refractive indices, whose main values are $N_O = 1.9634$ and $N_E = 2.6217$ at the wavelength $\lambda = 633 \text{ nm}$; its material density is equal to $\rho \approx 7.2 \text{ g/cm}^3$ [3.13]. This crystal is potentially suitable for effective non-collinear two-phonon light scattering and allows pure slow-shear elastic mode with the wave vector $\vec{K} \parallel [110]$, the displacement vector $\vec{u} \parallel [1\bar{1}0]$, the phase velocity $V_s \approx 0.347 \cdot 10^5 \text{ cm/s}$, and the acoustic wave attenuation factor $\Gamma \approx 230 \text{ dB/(cm GHz}^2)$, which gives the amplitude factor α in the form of $\alpha (\text{cm}^{-1}) = 0.1152 \Gamma f^2$.

At this point we will not motivate in detail our selection of the level B for total linear acoustic losses per optical aperture D of the calomel-made AOC. Nevertheless, together with traditionally exploited value $B = 4 \text{ dB}$ [20], the values $B = 6$ and 8 dB will be taken as well in a view of principle possibility to correct them later by the needed apodization. Choosing $B = 4, 6$ or 8 dB allows us to avoid unnecessarily strong limitations for this stage of studies. More detailed analysis can be started proceeding from the optical aperture $D = 5.2 \text{ cm}$ of the AOC, restricted by an available sample of the chosen crystalline material. Taking the above-mentioned levels of losses B per optical aperture, one can find the central frequencies for a two-phonon light scattering as $f_0 = \sqrt{B/(\Gamma D)}$, so that one yields $f_0 \approx 57.8, 71.0, \text{ and } 82.6 \text{ MHz}$ as well as $\alpha \approx 0.8851, 0.1336, \text{ and } 0.1808 \text{ cm}^{-1}$, respectively. For this triplet of the central acoustic frequencies, the first unit level maxima are placed at $(\sigma x)_1 = 2.427, 2.539, \text{ and } 2.662$.

After performing the above-proposed optimization, one can take $(\sigma x)_{1,\text{opt}} = 2.785, 2.965, \text{ and } 3.200$, which provide more symmetric distributions presented in Fig. 3.10. With $D = 5.2 \text{ cm}$, the desirable new maxima are located at the points $z_{\text{max}} \approx 2.308, 2.162, \text{ and } 2.019 \text{ cm}$, respectively. An example of the corresponding 3D-distribution with the $f_0 = 71.0 \text{ MHz}$ is presented in Fig. 3.11. Looking at these plots, one can find that the combined influence provided by acousto-

optical nonlinearity and linear acoustic losses leads to the some equivalent apodization of initially flat incident light beam, see solid lines in Fig. 3.10.

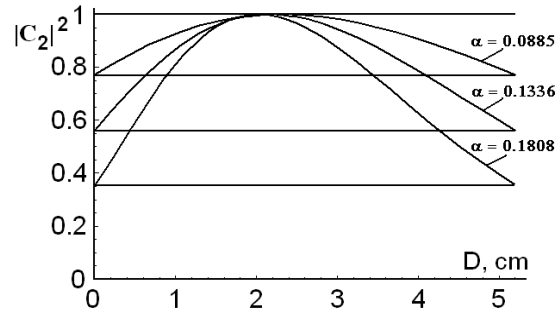


Fig. 3.10. Optimized 2D-profiles of the light distributions at the output facet of the calomel-made AOC at $f_0 \approx 57.8, 71.0,$ and 82.6 MHz with $\alpha \approx 0.8851, 0.1336,$ and 0.1808 cm^{-1} .

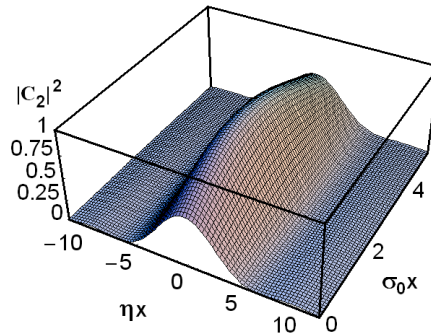


Fig. 3.11. An example of an optimized 3D-profile of the issuing light distribution with $f_0 = 71.0$ MHz and $\alpha \approx 0.1336 \text{ cm}^{-1}$.

To describe the Gaussian apodization for a flat incoming light beam with the field amplitude A_0 we take the origin of the physical coordinate z across that beam so that the point $z = 0$ is associated with the plane of piezoelectric transducer in an AOC. Then, one can introduce $y = z / D$ as the normalized dimensionless coordinate along the physical aperture D (measured in centimeters) of an AOC. Thus, $y \in \{0,1\}$ and one can write

$$A = A_0 \exp[-\chi(z-0.5D)^2] = A_0 \exp[-\beta(y-0.5)^2],$$

$$I(y) = |A_0|^2 \exp[-2\beta(y-0.5)^2]. \quad (3.26)$$

Here, χ and $\beta = \chi D^2$ are physical and dimensionless profile parameters for the apodizing Gaussian function; possible variations of $I(y)$ are governed by the profile parameter β . In particular, for the plots presented in Fig. 3.10, one can suggest the centered approximations with $\beta = 0.50, 1.15,$ and 2.10 , see Fig. 3.12, to avoid unnecessary strong consideration at this stage of studies. The shape of light field distribution $A(u)$ peculiar to an individual resolvable spot in the Fourier-transform plane, i.e. in a focal plane of the integrating lens, can be estimated analytically as

$$\text{a) } A(u) = \int_0^1 \exp[-\beta(y-0.5)^2] \exp(-2i\pi u y) dy, \quad \text{b) } A(u=0) = \sqrt{\frac{\pi}{\beta}} \text{Erf} (0.5 \sqrt{\beta}). \quad (3.27)$$

The spatial dimensionless coordinate u is centered on a maximum of that distribution, and $u = w D / \lambda F$, where w is the physical spatial coordinate in the focal plane and F is the focal distance of the integrating lens. Using Eqs.(3.8), the normalized distribution $I(u)$ of light intensity peculiar to an individual resolvable spot in the focal plane of the integrating lens can be written as $I(u) = A(u) A^*(u) A^{-2}(u=0)$ i.e.

$$I(u) = -\frac{1}{4} \operatorname{Erf}^{-2} \left(\frac{\sqrt{\beta}}{2} \right) \exp \left[-\frac{2\pi^2 u^2}{\beta} \right] \left\{ \operatorname{Erfi} \left[\frac{2\pi u - i\beta}{2\sqrt{\beta}} \right] - \operatorname{Erfi} \left[\frac{2\pi u + i\beta}{2\sqrt{\beta}} \right] \right\}^2. \quad (3.28)$$

In the case of $\beta \approx 0$, an ideal normalized profile of a resolvable spot has full width equal to unity in terms of the dimensionless coordinate u at the intensity level 0.405. The required corrections to theoretical width of a resolvable spot, conditioned by the presence of linear acoustic losses when $\beta \neq 0$, can be made using the correction factor κ of apodization. The needed values of this factor are: $\kappa \approx 1.019, 1.043, \text{ and } 1.080$, i.e. the main lobe has broadening by about 1.9, 4.3, and 8.0% due to the effect of linear acoustic losses for $\beta = 0.50, 1.15, \text{ and } 2.10$, respectively. Thus, the performed apodizations, provided by properties of an AOC near the first maximum, are not deep enough (they equal to $-14 \div -17$ dB for the first side lobe) to improve significantly the dynamic range of potential optical spectrum analysis, see Fig. 3.13.

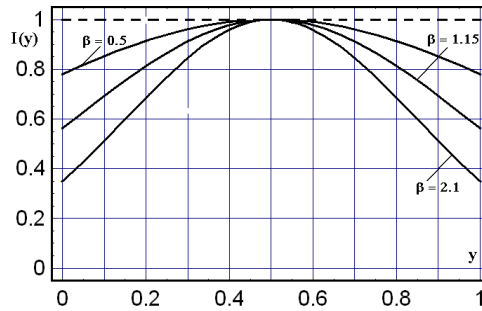


Fig. 3.12. Theoretical profiles for the Gaussian centered approximations with the dimensionless apodization parameters $\beta = 0.50, 1.15, 2.10$.

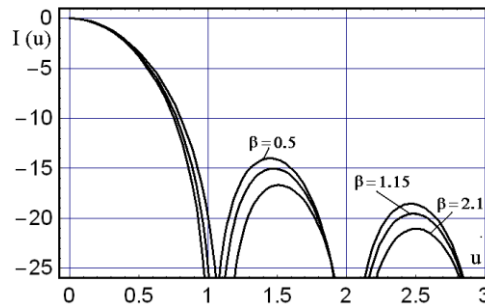


Fig. 3.13. Theoretical logarithmic profiles of resolvable spots with the dimensionless apodization parameters $\beta = 0.50, 1.15, 2.10$.

3.4.2 Second maxima

Within linear acousto-optics, one can use standard approach to estimating the action of linear acoustic attenuation using the Fourier transformation of exponentially falling down distribution at the AO cell's output facet. The Fourier transformed signal gives a resolvable spot profile in the focal plane of the integrating lens within classical scheme of spectrum analyzer [3.11]. In so doing, the light intensity profile of a spot gives the main lobe width and level of side lobes characterizing both the resolution and the dynamic range of an optical system. In our case, one should estimate the combined effect provided by acousto-optical nonlinearity and linear acoustic losses in AO cell. For this purpose, we compare with one another light distributions $C_2(x, z)$ along coordinate σx in the vicinity of various points $(\sigma x)_2$ peculiar to the second unit-level maxima for a few magnitudes of α . The preliminary analysis has shown that similar light distributions are significantly non-uniform along AO cell's aperture, so that the final Fourier transformed signals are not optimal in the focal plane of a lens. This is why those values $(\sigma x)_2$ had been somewhat exceeded with the purpose of making an optimization. The goal of such an optimization consists in achieving as much as possible more symmetrical light distributions at

the output facet of an AO cell. However, local maximum for each of these output light distributions is shifted from a point corresponding to the middle between two falling down wings of the corresponding distribution.

To make more concrete our consideration an appropriate acousto-optical crystalline material has to be selected for the further analysis. During the selection of a material, a few possibilities of exploiting either longitudinal or shear elastic modes, passing along various crystallographic directions, had been estimated. The analysis has shown that one of the best options for performing experiments, motivated by very high efficiency of scattering and not too high acoustic frequency for excitation, is the calomel (α -Hg₂Cl₂) single crystal. This crystal belongs to the 4/mmm – tetragonal symmetry group. It has spectral transmission band $\Delta\lambda = 0.38 - 28 \mu\text{m}$ and a pair of dispersive refractive indices, whose main values are $N_O = 1.9634$ and $N_E = 2.6217$ at the wavelength $\lambda = 633 \text{ nm}$; its material density is equal to $\rho \approx 7.2 \text{ g/cm}^3$ [3.13]. This crystal is potentially suitable for effective non-collinear two-phonon light scattering and allows pure slow-shear elastic mode with the wave vector $\vec{K} \parallel [110]$, the displacement vector $\vec{u} \parallel [1\bar{1}0]$, the phase velocity $V_s \approx 0.347 \cdot 10^5 \text{ cm/s}$, and the acoustic wave attenuation factor $\Gamma \approx 230 \text{ dB/(cm GHz}^2)$, which gives the amplitude factor α in the form of $\alpha(\text{cm}^{-1}) = 0.1152 \Gamma \text{ f}^2$.

At this point we will not motivate in detail our selection of the level B for linear acoustic losses per optical aperture D of the calomel-made AO cell. Nevertheless, together with traditionally exploited value $B = 4 \text{ dB}$ [3.20], the values $B = 3$ and 5 dB will be taken as well in a view of principle possibility to correct them later by the needed apodization. Choosing $B = 3, 4$ or 5 dB allows us to avoid unnecessarily strong limitations for this stage of studies. More detailed analysis can be started proceeding from the optical aperture $D = 5.2 \text{ cm}$ of the AO cell restricted by an available sample of the chosen crystalline material. Taking the above-mentioned levels of losses B per optical aperture, one can find the central frequencies for a two-phonon light scattering as $f_0 = \sqrt{B/(\Gamma D)}$ [3.21], so that one yields $f_0 \approx 50.1, 57.6$ and 64.66 MHz as well as $\alpha \approx 0.0665, 0.0885,$ and 0.1108 cm^{-1} , respectively. For this triplet of the central acoustic frequencies, the second unit level maxima are placed at $(\sigma x)_2 = 7.123, 7.281,$ and 7.445 when $z = 1 \text{ cm}$.

After performing the above-proposed optimization, one can take $(\sigma x)_{2, \text{Opt}} = 7.815, 8.21,$ and 8.56 , which provide more symmetric distributions presented in Fig. 3.14. With $D = 5.2 \text{ cm}$, the desirable new maxima are located at the points $z_{2, \text{max}} \approx 2.395, 2.357$ and 2.259 cm , respectively. An example of the corresponding 3D-distribution with the $f_0 = 57.8 \text{ MHz}$ is presented in Fig. 3.15. Looking at these plots, one can find that the combined influence provided by AO nonlinearity and linear acoustic losses leads to the some equivalent apodization of initially flat incident light beam, see profiles in Fig. 3.14.

Using the approach developed above, let us consider the second maxima for the same triplet of acoustic frequencies. As it seen from Figs. 3.14 and 3.15, initially one has $(\sigma x)_2 = 7.123, 7.281,$ and 7.445 for the acoustic frequencies $f_0 \approx 50.1, 57.6$ and 64.66 MHz with $\alpha \approx 0.0665, 0.0885,$ and 0.1108 cm^{-1} , respectively, while after the optimization one can take $(\sigma x)_{2, \text{Opt}} = 7.815, 8.21,$ and 8.56 , which provide more symmetric distributions presented in Fig. 3.14. With $D = 5.2 \text{ cm}$, the desirable new maxima are located at the points $z_{2, \text{max}} \approx 2.395, 2.357$ and 2.259 cm , respectively. The corresponding 3D-distributions with the same magnitudes of all the parameters can be found, and an example is presented in Fig. 3.15. Looking at these plots, one can find that the combined influence provided by acousto-optical nonlinearity and linear acoustic losses leads to the some equivalent apodization of initially flat incident light beam.

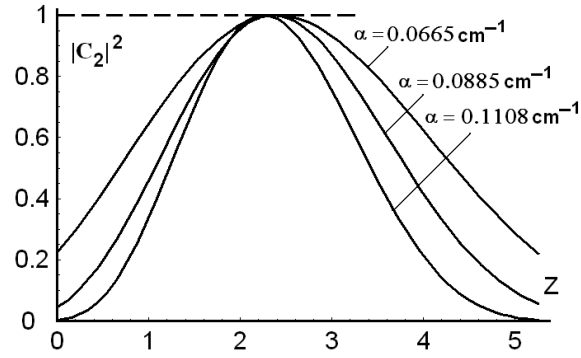


Fig. 3.14. Optimized 2D-profiles of the light distributions at the output facet of the calomel-made AO cell at $f_0 \approx 50.1, 57.6$ and 64.66 MHz with $\alpha \approx 0.0665, 0.0885,$ and 0.1108 cm^{-1} .

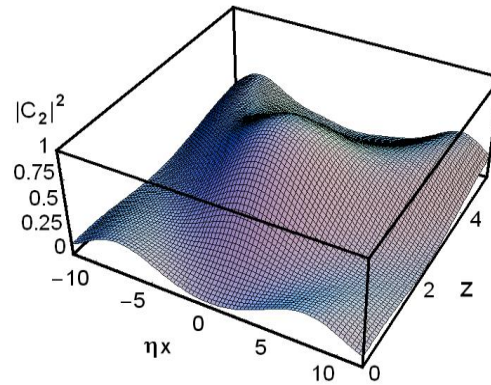


Fig. 3.15. An example of the optimized 3D-profiles for the issuing light distributions at $f_0 \approx 57.8$ MHz with $\alpha \approx 0.885 \text{ cm}^{-1}$.

To describe the Gaussian apodization for a flat incoming light beam with the field amplitude A_0 we take the origin of the physical coordinate z across that beam so that the point $z = 0$ is associated with the plane of piezoelectric transducer in an AO cell. Then, one can introduce $y = z / D$ as the normalized dimensionless coordinate along the physical aperture D (measured in centimeters) of an AO cell. Thus, $y \in \{0, 1\}$ and one can write

$$I(y) = |A_0|^2 \exp[-2\beta(y-0.5)^2] \quad (3.29)$$

for the apodizing Gaussian function; possible variations of $I(y)$ are governed by the profile parameter β . In particular, for the plots presented in Fig. 3.14, one can suggest the centered approximations with $\beta = 3.1, 6.0,$ and 9.0 , see Fig. 3.16, to avoid unnecessary strong consideration at this stage of studies.

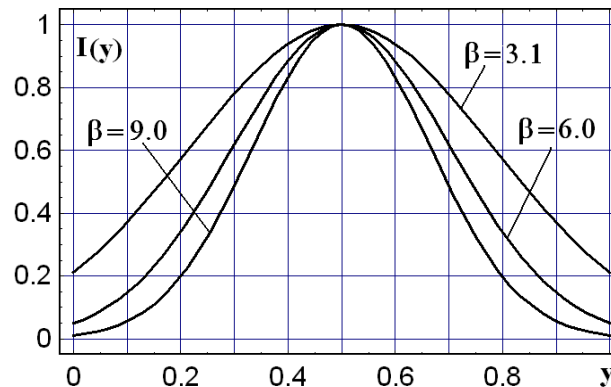


Fig. 3.16. Theoretical profiles for the Gaussian centered approximations with the dimensionless apodization parameters $\beta = 3.1, 6.0,$ and 9.0 .

In the case of Gaussian apodization, the normalized distribution $I(u)$ of light intensity peculiar to an individual resolvable spot in the focal plane of the integrating lens can be written as

$$I(u) = -\frac{1}{4} \operatorname{Erf}^{-2} \left(\frac{\sqrt{\beta}}{2} \right) \exp \left[-\frac{2\pi^2 u^2}{\beta} \right] \left\{ \operatorname{Erfi} \left[\frac{2\pi u - i\beta}{2\sqrt{\beta}} \right] - \operatorname{Erfi} \left[\frac{2\pi u + i\beta}{2\sqrt{\beta}} \right] \right\}^2. \quad (3.30)$$

The spatial dimensionless coordinate u is centered on a maximum of that distribution; then, $u = w D / \lambda F$, where w is the physical spatial coordinate in the focal plane and F is the focal distance of the integrating lens. The corresponding profiles of resolvable spots in linear scale are shown in Fig. 3.17.

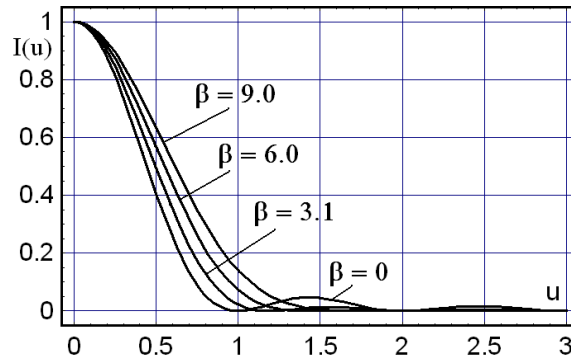


Fig. 3.17. Theoretical profiles of resolvable spots with the broadening parameters $\kappa \approx 1.121, 1.248,$ and 1.391 for the same dimensionless apodization parameters $\beta = 0, 3.1, 6.0,$ and 9.0 .

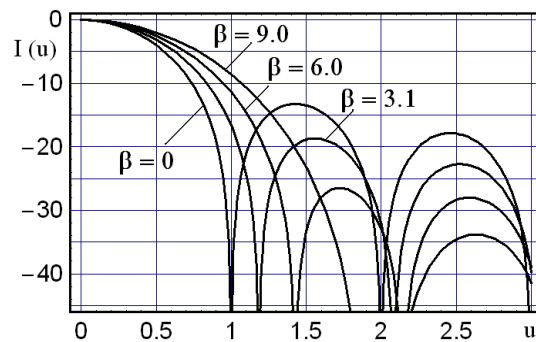


Fig. 3.18. Theoretical logarithmic profiles of resolvable spots with the dimensionless apodization parameters $\beta = 0, 3.1, 6.0,$ and 9.0 .

Thus, the performed apodizations, provided by properties of an AO cell near the second maximum, are relatively deep (they equal to $-13, -18, -27,$ and -32 dB for the first side lobe with $\beta = 0, 3.1, 6.0,$ and 9.0) to improve significantly the dynamic range of potential optical spectrum analysis, see Fig. 3.18.

3.5 Theoretical estimations of a dispersive component based on the calomel-made crystalline AOC

3.5.1 Effect of the acoustic beam divergence

The angular divergence of the acoustic beam can be considered via estimating the length X of Fresnel acoustic zone when the unknown radiating acoustic aperture is equal to R . These values are connected with one another as $X = R^2 f / (2V)$ [3.22]. If it is granted that the acoustic beam belongs to Fresnel acoustic zone and $X = 10$ cm, one find for $\alpha\text{-Hg}_2\text{Cl}_2$ that $R \approx \sqrt{2V_S X / f_S} = \sqrt{2V_L X / f_L} \approx 0.12$ cm. Thus with $R \geq 0.15$ cm, which lies in frames of

the above-agreed value and is rather typical value in practice, one can say that potential angular divergence of acoustic beam is small enough to be definitely omitted, so that the plane-wave approximation is rather close to the reality.

3.5.2 General estimations for the calomel-made AOC

At first, let us perform theoretical estimations for the calomel-made AOC with $D = 10$ cm and $L_{\min} \approx 0.2$ cm. The summary of similar estimations is presented in Tables 3.1 and 3.2. One can see from these tables that the highest spectral resolution and the largest number of resolvable spots within the widest spectral range can be achieved in calomel with the exploitation of the pure slow shear elastic mode.

To compare these results with the collinear AOF based on a long-aperture $L = 10$ cm lithium niobate (LiNbO_3) crystal, for example, at $\lambda = 633$ nm. We choose this wavelength to avoid well-known possible problems with the effect of photorefraction in this crystal, which has $N_O = 2.28646$, $N_E \approx 2.20222$, and $|\Delta n| \approx 0.08424$ at $\lambda = 633$ nm. Then, one has to take into account that the collinear AOI does not exhibit the above-discussed degree of freedom given by Eq.(3.1). As a result, it is able to give exactly one resolvable spot, i.e. to provide only sequential optical spectrum analysis. Within the collinear interaction, the optical wavelength λ and the corresponding acoustic wave frequency are unambiguously connected. Therefore for $\lambda = 633$ nm, it requires $f = |\Delta n|V / \lambda \approx 0.8743$ GHz for pure longitudinal elastic mode with $\vec{K} \parallel [100]$ in the lithium niobate crystal has $V_L \approx 6.57 \times 10^5$ cm/s and $\Gamma \approx 0.15$ dB / (cm GHz²) [3.1]. This is why one can find that optical aperture or, equivalently in the collinear case, the length of AOI is $L = B / (\Gamma f_0^2) \approx 40$ cm with $B = 6$ dB / aperture. Of course, such a length of a crystal is unachievable in practice, due to technological limitations; and one has to take $L \leq 10$ cm. In this case, one can estimate that $|\Delta n|L \approx 0.842$ cm and $\delta\lambda^{(L)} = \lambda^2 / (|\Delta n|L) \approx 0.473$ Å. This result can be marked like an individual level (or a point) on both the diagrams in Figs.6 and 7. By the way, this comparison shows that developing a new approach to optical spectrum analysis is possible. Thus we propose a parallel algorithm of signal processing with an appreciably improved spectral resolution.

Table 3.1. Theoretical estimations; here, $\delta f = V / 2 D$ and $\delta\lambda = \delta f \lambda / f_0$ are frequency and spectral resolutions, $f_0 = \sqrt{B/(D\Gamma)}$ is the central acoustic frequency, and the product $2 b D = \lambda^2 / \delta\lambda$ includes the birefringence factor

Wavelength λ , nm	n_o	Elastic mode	V , 10^5 cm/s	Γ , dB/(cm GHz ²)	δf , kHz	f_0 , MHz	$\delta\lambda$, Å	$2 b D$, cm
405	2.0826	S[110]	0.347	230	1.735	51.08	0.1376	1.192
		L[100]	1.622	12.5	8.11	219.1	0.150	1.0935
633	1.9634	S[110]	0.347	230	1.735	51.08	0.2151	1.863
		L[100]	1.622	12.5	8.11	219.1	0.234	1.7094

Table 3.2. Practical estimations; here, $\Delta f = 2 |f - f_0| \approx n_o V^2 / (\lambda L f_0)$ and $\Delta\lambda = \Delta f \lambda / f_0$ are frequency and spectral bandwidths, while $N = \Delta f / \delta f = \Delta\lambda / \delta\lambda$ is the number of resolvable spots.

Wavelength λ , nm	n_o	Elastic mode	Δf , MHz	$\Delta\lambda$, Å	N , spots
405	2.0826	S[110]	6.07	482	3500
		L[100]	30.877	571	3807
633	1.9634	S[110]	3.66	454	2110
		L[100]	18.630	538	2300

3.5.3 Figure of acousto-optical merit for the non-collinear two-phonon light scattering in calomel crystal

Generally, estimating the figure of acousto-optical merit M_2 for the above-chosen geometry in $\alpha\text{-Hg}_2\text{Cl}_2$ single crystal and the slow shear acoustic mode with the normalized displacement

vector $\vec{u} = (1, -1, 0) / \sqrt{2}$, the acoustic wave vector $\vec{K} \parallel [110]$, and the deformation tensor γ had been recently performed [3.17]. Therefore, it is known that the effective photo-elastic constant p_{eff} is given by

$$p_{\text{eff}} = \vec{e}_1 (p\gamma) \vec{e}_0 = 0.5 (p_{11} - p_{12}) \approx 0.055, \quad (3.31)$$

where the vectors \vec{e}_0 and \vec{e}_1 describe the polarization states of incident and scattered light beams, respectively. Within the anomalous non-collinear acousto-optical interaction, the eigen polarization vectors \vec{e}_0 and \vec{e}_1 of the incident and scattered light beams should be orthogonal to one another $\vec{e}_0 \perp \vec{e}_1$, and they both have to be lying in the same plane as the wave vector $\vec{K} \parallel [110]$. For the sake of simplicity, in this case, one can take $\vec{e}_0 \parallel \vec{K}$ and $\vec{e}_1 \parallel \vec{u}$, i.e. $\vec{e}_0 = (1, 1, 0) / \sqrt{2}$ and $\vec{e}_1 = (1, -1, 0) / \sqrt{2}$. Then, the magnitude of $M_2 = n_0^3 n_E^3 (p_{\text{eff}})^2 / (\rho V^3)$ includes also the material density $\rho = 7.2 \text{ g/cm}^3$ and a pair of rather dispersive refractive indices n_0 and n_E . The last two parameters should be taken exactly at the wavelength λ exploited under condition that the correct tilt angle ψ is taken into account, see Table 3.2. These values of M_2 demonstrate that the anomalous light scattering, governed by the pure slow shear acoustic mode in the calomel are sufficiently efficient and this crystal is able to provide effective two-phonon light scattering.

Then, the above-chosen first maxima in light distribution require the following optimized power parameters $(\sigma x)_{1,\text{Opt}} = 2.785, 2.965$ and 3.200 at $f_0 \approx 57.8, 71.0$ and 82.6 MHz when $\alpha = 0.8851, 0.1336, 0.1808 \text{ cm}^{-1}$ and the correction factor of apodization $\kappa \approx 1.019, 1.043, 1.080$, respectively. With $x \equiv L$ and $L = 0.2 \text{ cm}$, one can find $\sigma_{1,\text{Opt}} = 13.925, 14.825, \text{ and } 16.000 \text{ cm}^{-1}$. Now, the standard determination for σ [3.23] with $\cos \theta \approx 1$ can be re-written specifically to the acoustic power density P_1 needed for the first maxima as

$$P_1 \approx \frac{2\lambda^2 \sigma_{1,\text{Opt}}^2}{\pi^2 M_2}. \quad (3.32)$$

Thus, for example at $\lambda = 405 \text{ nm}$ and $f_0 \approx 82.6 \text{ MHz}$, Eq.(3.32) gives the optimized value of $P_1 \approx 10^3 \text{ mW/mm}^2$, see Table 3.3. Additionally, one has to find the Bragg angles of light incidence for the two-phonon regime as $\theta \approx K / k = f_0 \lambda / V$.

Table 3.3. Pre-experimental estimations; here, $d_s = \kappa \lambda F / D$ is an ideal spot size in the approximation of geometric optics with the correction factor of apodization $\kappa \approx 1.019, 1.043, \text{ and } 1.080$, $F = 85 \text{ cm}$, and $D = 5.2 \text{ cm}$.

$\lambda, \text{ nm}$	$f_0, \text{ MHz}$	$\psi, \text{ rad}$	n_0	n_E	$\theta, \text{ rad}$	$d_s, \mu\text{m}$	$M_2, \text{ s}^3/\text{g}$	$P_1, \text{ mW/mm}^2$
405	57.8	0.044	2.0826	2.0837	0.068	6.746	821.7×10^{-18}	78
	71.0	0.055	2.0826	2.0843	0.083	6.905	822.4×10^{-18}	89
	82.6	0.064	2.0826	2.0848	0.096	7.149	823.1×10^{-18}	103
633	57.8	0.081	1.9634	1.9662	0.105	10.543	578.5×10^{-18}	272
	71.0	0.100	1.9634	1.9677	0.129	10.792	579.8×10^{-18}	307
	82.6	0.116	1.9634	1.9692	0.151	11.175	581.1×10^{-18}	358

3.6 Proof of principal experimental data

3.6.1 Experiment arrangement

3.6.1.1 First Maxima

First, one can estimate the potential contributions of the acoustic losses. For the chosen slow shear elastic mode passing along the $[110]$ -axis, whose displacement vector is oriented along the $[11, \bar{0}]$ -axis. The coefficient of linear attenuation is $\Gamma \approx 230 \text{ dB}/(\text{cm GHz}^2)$ in a calomel

single crystal [15]. The factor $\alpha[\text{cm}^{-1}]$ of the amplitude acoustic losses is $\alpha[\text{cm}^{-1}] = 0.1152 \Gamma[\text{dB}/(\text{cm GHz}^2)] f^2[\text{GHz}]$. The carrier frequency, peculiar to the non-collinear two-phonon AOI in calomel, can be calculated as $f_0 \approx 71$ MHz at the above-chosen light wavelength 405 nm. Consequently, one can estimate the amplitude factors for acoustic losses by $\gamma = \Gamma f_0^2 \approx 1.16$ dB/cm and $\alpha = 0.134 \text{ cm}^{-1}$.

The angular divergence of the acoustic beam in the calomel non-collinear AOC at the frequency $f_0 \approx 71$ MHz can be estimated as well. A reliable spatial size of the initial acoustic beam aperture that we will consider is close to $L \approx 0.2$ cm. With $V_{SS} = 0.347 \times 10^5$ cm/s, one can calculate the corresponding acoustic wavelength $\Lambda = V / f_0 = 0.489 \times 10^{-3}$ cm and the angle of acoustic beam divergence $\varphi = \Lambda / L \approx 0.244 \times 10^{-2}$ rad $\approx 0.14^\circ$ to conclude that the angular divergence of the acoustic beam can be omitted.

Now, we are ready to perform the few important numerical estimations inherent in the non-collinear interaction at the light wavelength of $\lambda = 405$ nm in the calomel crystalline cell with $M_2 \approx 2546 \times 10^{-18} \text{ s}^3 / \text{g}$ and $L = 0.2$ cm. The periodicity of the unit-level AOI maxima (see Fig. 3.3) gives us an opportunity to choose the second maximum with one of the widest bandshape at $(\sigma x)_2 \approx 6.667$, so that putting $x \equiv L$, one can find $\sigma_2 \approx 33.3 \text{ cm}^{-1}$. Using the standard determination for σ [3.23] with $\cos \theta \approx 1$, one can write

$$P \approx \frac{2\lambda^2 \sigma^2}{\pi^2 M_2} . \quad (3.33)$$

Consequently, at $\lambda = 405$ nm Eq.(3.33) gives $P_2 \approx 145 \text{ mW/mm}^2$ for the second maximum. Additionally, one has to take into account the losses needed for converting the electronic signal into an acoustic one, which are in practice close to 2 – 3 dB as the case requires. Usually, we have to restrict ourselves to a maximum level $P \leq 0.5 \text{ W/mm}^2$ of acoustic power density. This requires the absolute acoustic power magnitude of about 2 W and the acoustic beam cross section of about 4 mm^2 in the AOC under consideration. The produced estimations demonstrate that the above-obtained level for P_2 lies in the ranges of accessible value, while similar parameters P_2 and σ_2 for the second unit-level AOI maximum are beyond these frames. One can see from Fig. 3 that reaching the next maximum needs a much higher acoustic power density in comparison with the second one. This looks rather conjectural from the viewpoint of requirements for the electric strength inherent in the available piezoelectric transducer. After that, pre-experimental estimations for the calomel-made AOC with $D = 5.2$ cm and $L_{\min} \approx 0.2$ cm can be summarized in Table 3.4. These estimations exploit the pure slow shear elastic mode with the acoustic velocity $V_{SS} = 0.347 \times 10^5$ cm/s in the scheme of the standard acousto-optical spectrum analyzer with the integrating lens of the focal distance $F = 85$ cm.

The design of the calomel crystalline AOC under consideration, operating in the regime of the non-collinear two-phonon AOI, is presented in detail in Fig. 3.19. The piezoelectric transducer represented by a thin plate made of the 163° Y-cut LiNbO_3 single crystal had been placed on the (110) crystallographic plane of the calomel crystal and provided the slow shear mode acoustic beam cross section of about 4 mm^2 at the length $L = 0.2$ cm of AOI in calomel.

At $\lambda = 405$ nm and the above-estimated acoustic wavelength $\Lambda = 0.489 \times 10^{-3}$ cm, one can find the Bragg angle θ_0 (see Fig. 3.19a) needed for the non-collinear two-phonon AOI as $\theta_0 \approx 0.0414$ rad $\approx 2.37^\circ$. Together with this, the tilt angle ψ needed for $D = 5.2$ cm and $f_0 \approx 71$ MHz (see Fig. 19b) can be estimated from Eq.(9) by the value $\psi \approx 0.0546$ rad $\approx 3.13^\circ$ with $\lambda = 405$ nm, $V_{SS} = 0.347 \times 10^5$ cm/s, $N_O = 2.0826$, and $N_E = 3.03794$ in calomel.

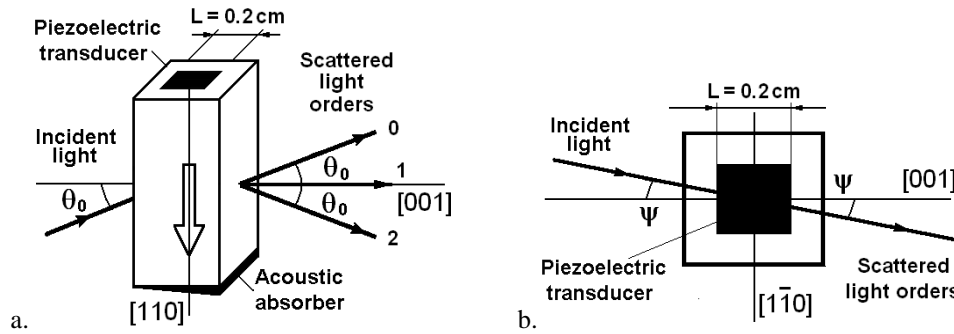


Fig. 3.19. The design of the calomel AOC: (a) depicts the general view with the Bragg angles of incidence and scattering in three orders, while (b) shows the top view with the needed tilt angle ψ .

Our proof-of-principal experiments had been performed with the specially designed wide-aperture AOC based on the unique calomel single crystal. This pioneer AOC works at optical wavelength $\lambda = 405$ nm, which combines the convenience of operating in just the visible range with the best-expected optical performances inherent in this AOC with violet light, from the single frequency solid-state laser CL-405-050--S (CrystaLaser). Theoretically (see section 5), the calomel-based AOC could be governed by the radio-wave signals whose the best acoustic performances were expected at the central frequency about 71 MHz, frequency bandwidth $\Delta f \approx 4.36$ MHz, and frequency resolution $\delta f \approx 3.337$ KHz providing the number $N \approx 1307$ of resolvable spots. The experiments included a Glan-Thompson linear polarizer and a four-prism beam expander, which operated with the light beam polarized in the plane of expanding and provided rather flat (non-uniformity $\sim 11\%$) optical beam profile. During the experiments with the beam shaper rather accurate angular adjusting of the incident light beam had been achieved. By this it means that both the correct Bragg angle of incidence and the needed tilt angle had been optimized. The 3-inch achromatic doublet lens (#30-976, Edmund Optics) with the focal length of about 85 cm had been used as the integrating lens, and the multi-pixel CCD-linear array consisting of $4.7 \mu\text{m}$ pixels was playing the role of a photo-detector. The layout of the optical scheme of the experiments is presented in Fig. 3.20.

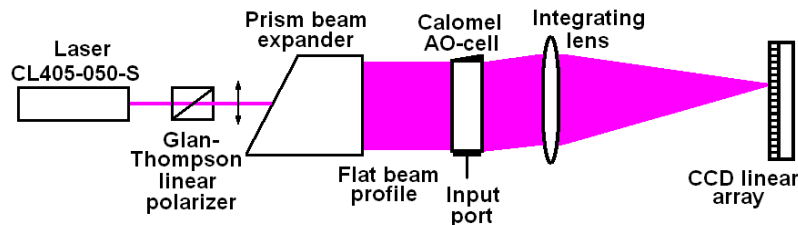


Fig. 3.20. The layout of the optical scheme; only the 2-nd order of a two-phonon AOI is shown.

Table 3.4. Pre-experimental estimations; here, $d_s = \lambda F / D$ is an ideal spot size in the approximation of geometric frequency, M_2 is the figure of acousto-optical merit, and P_2 is the acoustic power density needed for the second maxima.

λ , nm	n_O	n_E	d_s , μm	δf , kHz	M_2 , s^3/g	$\delta\lambda$, \AA	$2 b D$, cm	P_2 , mW/mm^2
405	2.0826	3.0379	6.620	3.337	2.5×10^{-15}	0.190	0.862	145
633	1.9634	2.6217	10.347	3.337	1.4×10^{-15}	0.368	1.347	657

Previously, we had to restrict ourselves by a maximum level $P \leq 0.5 \text{ W}/\text{mm}^2$ of acoustic power density. However, a design of the damped piezoelectric transducer admits the acoustic power density by a magnitude of about $P_1 \leq 3.5 \text{ W}/\text{mm}^2$ for the acoustic beam cross section of about 4 mm^2 in the AOC under consideration. The produced estimations demonstrate that the above-required levels of the parameters P_1 and $\sigma_{1,\text{opt}}$ for the first unit-level maxima lie in the ranges of accessible values. One can find from Eq.(3.32) that reaching the next maxima [3.17] need much higher acoustic power densities in comparison with the first ones. This looks rather conjectural from the viewpoint of requirements for the electric strength inherent in the available piezoelectric transducer. After that, pre-experimental estimations for the calomel-made AOC

with $D = 5.2$ cm and $L_{\min} \approx 0.2$ cm can be summarized in Table 3.4. These estimations imply exploiting the pure slow shear elastic mode with the acoustic velocity $V = 0.347 \times 10^5$ cm/s in the scheme of the standard acousto-optical spectrum analyzer with the integrating lens of the focal distance $F = 85$ cm.

The design of the calomel crystalline AOC under consideration, operating in the regime of the non-collinear two-phonon light scattering, is presented in detail in Fig. 3.21. The piezoelectric transducer represented by a thin plate made of the 163° Y-cut LiNbO_3 single crystal had been placed on the (110) crystallographic plane of the calomel crystal. It provided the excitation of a slow-shear mode acoustic beam with the cross section of about 4 mm^2 and the length $L = 0.2$ cm of interaction in calomel. The needed Bragg and tilt angles, whose orientations are depicted in Fig. 3.21, are enumerated in Table 3.2.

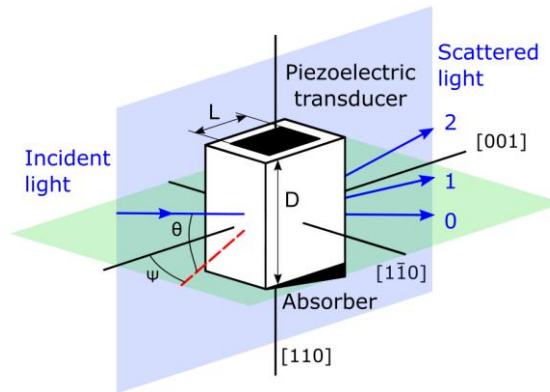


Fig. 3.21. The design of the calomel AOC.

3.6.1.2 Second Maxima

First, one can estimate the potential contributions of the acoustic losses for the chosen slow shear elastic mode passing along the $[110]$ -axis, whose displacement vector is oriented along the $[1\bar{1}0]$ -axis. Because of the coefficient of linear attenuation is $\Gamma \approx 230 \text{ dB}/(\text{cm GHz}^2)$ in a calomel single crystal [3.13], the factor α [cm^{-1}] of the amplitude acoustic losses is determined as α [cm^{-1}] = 0.1152Γ [$\text{dB}/(\text{cm GHz}^2)$] f^2 [GHz]. The carrier frequencies $f_0 \approx 50.1, 57.8,$ and 64.66 MHz at the light wavelengths 405 and 442 nm, peculiar to the non-collinear two-phonon light scattering in calomel, had been chosen above. Consequently, one can estimate the amplitude factors for linear acoustic losses by γ [dB/cm] = Γf_0^2 , which gives $\gamma = 0.575 \text{ dB}/\text{cm}$, $\alpha = 0.0665 \text{ cm}^{-1}$; $\gamma = 0.768 \text{ dB}/\text{cm}$, $\alpha = 0.0885 \text{ cm}^{-1}$; and $\gamma = 0.962 \text{ dB}/\text{cm}$; $\alpha = 0.1108 \text{ cm}^{-1}$, respectively, for those frequencies.

Additionally, one has to take into account the losses needed for converting the input electronic signal into an acoustic one, which are usually slightly exceeding 2 dB. However within these our experiments, we had decided to modify the piezoelectric transducer. The practically important problem is connected with relatively narrow frequency and spectral bandwidth of the AO cell exploiting the non-collinear two-phonon light scattering. The matter is that calomel is sufficiently effective acousto-optical material, so that the band-shape width of the calomel-made AO cell can be expanded at the cost of decreasing the efficiency of that AO cell. In so doing, the thickness of upper electrode, placed over piezoelectric material, had been a little bit increased to implement the effect of oscillation damping. The goal of such a low damping was to decrease the quality factor of acoustic resonance inherent in that piezoelectric transducer. Our experimental estimations have demonstrated that such a damping grew the losses for converting the electronic signal into an acoustic one up to 3.0 – 3.5 dB, while the acoustic resonance curve of that piezoelectric transducer showed a broader maximum and leads to a broader band-shape of AO cell.

Previously, we had to restrict ourselves by a maximum level $P \leq 0.5 \text{ W/mm}^2$ of acoustic power density. However, novel design of the damped piezoelectric transducer admits the acoustic power density by a magnitude of about $P_2 \leq 3.0 \text{ W/mm}^2$ for the acoustic beam cross section of about 4 mm^2 in the AO cell under consideration. The produced estimations demonstrate that the above-required levels of the parameters P_2 and $\sigma_{2,\text{Opt}}$ for the second unit-level maxima lie in the ranges of accessible values. One can find from Eq. (3.7) that reaching the next maxima [3.17] need much higher acoustic power densities in comparison with the first ones. This looks rather conjectural from the viewpoint of requirements for the electric strength inherent in the available piezoelectric transducer. After that, pre-experimental estimations for the calomel-made AO cell with $D = 5.2 \text{ cm}$ and $L_{\text{min}} \approx 0.2 \text{ cm}$ can be summarized in Table 3.4. These estimations imply exploiting the pure slow shear elastic mode with the acoustic velocity $V = 0.347 \times 10^5 \text{ cm/s}$ in the scheme of the standard acousto-optical spectrum analyzer with the integrating lens of the focal distance $F = 85 \text{ cm}$.

The design of the calomel crystalline AO cell under consideration, operating in the regime of the non-collinear two-phonon light scattering, is presented in detail in Fig. 3.22. The piezoelectric transducer represented by a thin plate made of the 163° Y-cut LiNbO_3 single crystal had been placed on the (110) crystallographic plane of the calomel crystal. It provided the excitation of a slow-shear mode acoustic beam with the cross section of about 4 mm^2 and the length $L = 0.2 \text{ cm}$ of interaction in calomel. The needed Bragg and tilt angles, whose orientations are depicted in Fig. 3.22, are enumerated in Table 3.2.

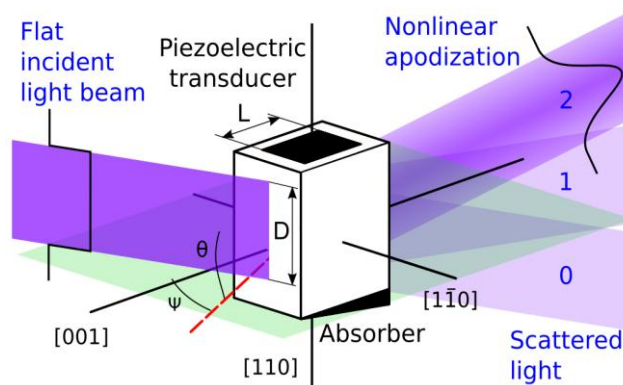


Fig. 22. Design of the calomel AO cell .

3.6.2 Experimental results

3.6.2.1 First Maxima

Experimental verification of the optical spectrum analysis under proposal had been carried out with the Bragg cell, made of a unique calomel ($\alpha\text{-Hg}_2\text{Cl}_2$) single crystal, which had an active optical aperture of about $52 \times 2 \text{ mm}$, see Fig. 3.19. While operating at the optical wavelengths of 405 nm with linear state of the incident light polarization oriented along the crystallographic axis $[110]$ on the central acoustic frequency of about 71 MHz , this cell allowed a maximum input acoustic power of about 1.5 W .

The experiments consisted of two parts. The first part included measuring the bandwidth of the Bragg non-collinear two-phonon AOI. The second part of our experiments was related to estimating possible spectral resolution within involving this AOC into the optical spectrum analysis via measurements of the light intensity distributions peculiar to an individual spots in the focal plane of the integrating lens for light deflected by that calomel AOC into the second order. Fig. 3.23 shows the experimental plot for the frequency bandshape inherent in the calomel cell. One can observe the characteristic variations of efficiency at the top of the

experimental plot. The total experimental frequency bandwidth at a -3 dB-level has been estimated by $\Delta f_{\text{exp}} \approx 5.1$ MHz.

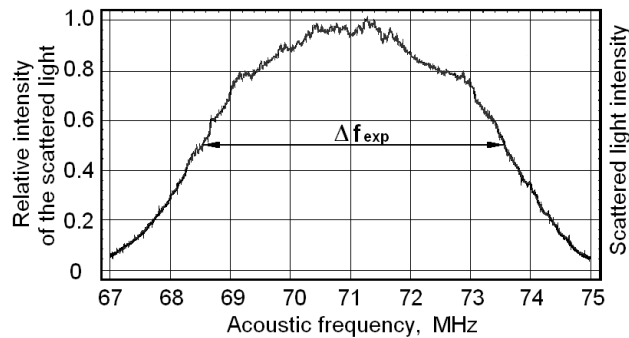


Fig. 3.23. Experimentally obtained frequency bandshape for the AOC made of calomel. The full width at the half-maximum level can be estimated by about of $\Delta f_{\text{exp}} \approx 5.1$ MHz.

The calomel crystal is very effective, but rather specific material whose transmission optical range is starting from 380 nm, while its main refractive indices are high enough and equal to about $n_o = 2.083$ and $n_e = 3.038$ at 405 nm. By this it means that one can expect remarkable optical losses and reflections with operating at 405 nm. Consequently, to optimize the experimental conditions both the input and output facets of the calomel-made acousto-optical cell should have anti-reflection coating. However, during our proof-of-principle experiments the cell had not been coated. This is why the diffraction efficiency had been estimated in terms of the transmitted light, i.e. at the output facet of the calomel-made acousto-optical cell. By this it means that the measured light intensity, transmitted through the cell without any input electronic signal at the piezoelectric transducer, had been taken to be the unity. When the input signal is applied to the piezoelectric transducer, one can measure the portion of light intensity scattered into the second order and estimate its ratio to the initially measured transmitted light intensity. Just this ratio, completely caused by an external signal, we consider as the measure of the “diffraction efficiency”. This experimentally obtained maximal ratio (i.e. the diffraction efficiency) at the optimal acoustic frequency about 71 MHz had been estimated by the value ~ 0.94 when the applied electronic signal power was about 1.2 W providing the acoustic power density ≤ 150 mW/mm².

Precise optical measurements had been performed at the wavelength 405 nm to obtain sufficiently reliable estimations for the frequency resolution providing by the α -Hg₂Cl₂-cell together with the above-described optical system, including the CCD linear array. The realized measurement had been done in the regime of the so-called “hot cell”, i.e. with a radio-wave signal applied at the input port of the α -Hg₂Cl₂-cell. Figure 24 depicts the light intensity profile with the spot size of about 8.2 microns and the side lobe level of about 6.2%, which includes affecting the light distribution in a spot by the acoustic losses of 6 dB / aperture. This plot is a result of the standard computer processing realized by the CCD-camera. The produced measurements showed that the main lobe of a partial optical beam gave the spot size lighting almost two pixels of the CCD-row that provided rather acceptable resolution of a pattern from viewpoint of the sampling theorem.

As it had been noted, our experimental results have been obtained using the integrating lens with $F = 85$ cm at the wavelength 405 nm, so that theoretically the spot size is $d_s = \lambda F / D \approx 6.62$ μm . Together with this, the plot in Fig. 3.24 exhibits the experimental spot size $d_T = \lambda F / D_T \approx 8.2$ μm that corresponds to the aberration factor $\zeta_T \approx 1.2375$ (which includes, of course, optical imperfectness of the system), and consequently, to the effective aperture $D_T \approx 4.202$ cm for the AOC. The last data show that about 20% of the active optical aperture of the AOC is lost due to imperfectness of the lens and cell’s material. Therefore, instead of theoretical limit of the frequency resolution $\delta f = V / 2D \approx 3.337$ kHz, one yields the measured value $\delta f_T = V / 2D_T \approx 4.13$ kHz. Then, $\Delta \lambda_T = \Delta f_T \lambda / f_0 \approx 291$ \AA (instead of the theoretical value $\Delta \lambda \approx 248.7$ \AA) with

$\delta\lambda_T = \lambda \delta f_T / f_0 \approx 0.235 \text{ \AA}$. Thus the experimentally obtained number of resolvable spots is $N_T = \Delta f_T / \delta f_T = \Delta\lambda_T / \delta\lambda_T \approx 1235$ spots, which is rather close to the obtained theoretical estimation. Finally, the expected lighted length in the focal plane of the integrating lens is $L_{CE} = d_T N_T \approx 10.12 \text{ mm}$, i.e. capabilities of the experimental optical system lie in the frames of the exploited multi-pixel CCD-array.

The obtained results with calomel AOF (the spectral resolution $\delta\lambda \approx 0.235 \text{ \AA}$ at 405 nm, which gives the resolving power $R \approx 17,200$) can be compared with the most advanced to our knowledge, acousto-optical spectrometers for space or airborne operations of the twenty-first century. For example, one can mention astrophysically oriented acousto-optical spectrophotometer, exploiting a TeO_2 based AOF, exhibited the spectral resolution $\delta\lambda \approx 12 \text{ \AA}$ at $\lambda = 636.5 \text{ nm}$ [3.24], then the acousto-optical spectrometers used onboard space mission Mars Express with $\delta\lambda \approx 5 \text{ \AA}$ at $\lambda \approx 1000 \text{ nm}$ [3.25] and space mission Venus Express with $\delta\lambda \approx 4.2 \text{ \AA}$ at $\lambda \approx 650 \text{ nm}$ [3.26]. Also, we can compare our results with previously mentioned KDP AOF, which exhibits a high spectral resolution $\delta\lambda \approx 0.625 \text{ \AA}$ at $\lambda \approx 325 \text{ nm}$ giving the resolving power $R \approx 5,200$ [3.5]. Together with this, one can take the other data from our introduction. By this it means that our results with calomel AOF can be considered like the best we can mention at the moment.

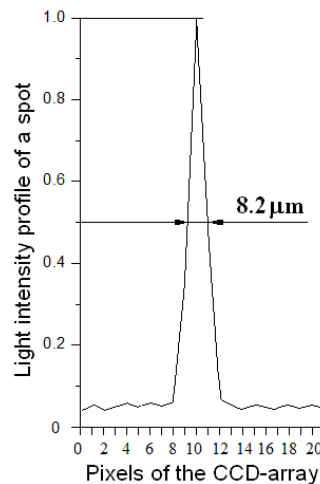


Fig. 3.24. Light intensity profile of an individual resolvable spot observed in the 2nd order of scattering. It is a result of the standard processing provided by the CCD-camera. The full width at the half-maximum of the main lobe can be estimated by about of 8.2 microns.

The experiments consisted of two parts. The first of them included detecting the frequency bandshape with a low oscillation damping, i.e. determining the effective bandwidth of the Bragg non-collinear two-phonon light scattering at a 0.405-level of light intensity. The second part of those experiments was related to estimating possible spectral resolution within involving this AOC into the optical spectrum analysis. It was done via measurements of individual resolvable spots in the focal plane of the integrating lens for the light deflected by into the second order of scattering. Figure 3.25 shows an example of the experimental trace for the frequency bandshape inherent in the calomel AOC with the damped piezoelectric transducer at the central frequency about 82.6 MHz, which had been detected under lighting by the coherent violet light $\lambda = 405 \text{ nm}$. The total experimental frequency bandwidth at a 0.405-level of light intensity has been estimated by $\Delta f_M \approx 2.856 \text{ MHz}$. Precise optical measurements had been performed at two wavelengths 405 and 633 nm to obtain sufficiently reliable estimations for the frequency resolution provided by the calomel AOC together with the above-described optical system, including the CCD linear array. The performed measurements had been done in the regime of the so-called “hot cell”, i.e. with a radio-wave signal applied at the input port of the $\alpha\text{-Hg}_2\text{Cl}_2$ -cell. Figure 3.26 depicts the intensity profile with the spot size of about 8.3 microns with the side lobe level of about 6.6 %, which include affecting the light distribution in a spot by the acoustic losses of 8 dB / aperture. The measurements showed that the main lobe of a spot gave

lighting about two pixels of the CCD-row that provided acceptable resolution of a pattern from viewpoint of the sampling theorem.

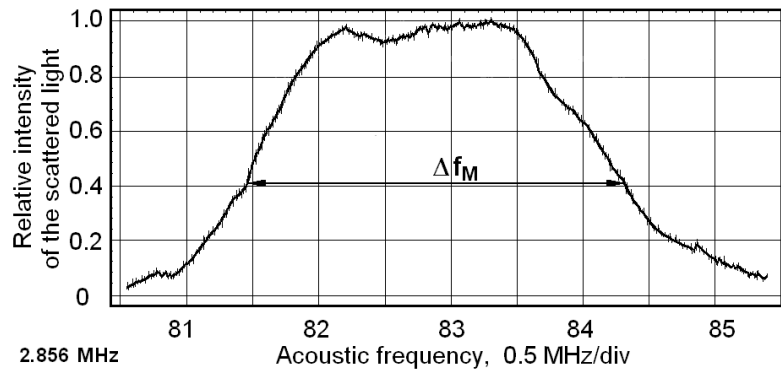


Fig. 3.25. Experimentally obtained frequency bandshape of the calomel-made AOC at $f_0 \approx 82.6$ MHz and $\lambda = 405$ nm.

As it had been noted, our experimental results have been obtained using the integrating lens with $F = 85$ cm at the wavelength 405 nm, so that theoretically the spot size is $d_s = \kappa \lambda F / D \approx 7.149 \mu\text{m}$. Together with this, the plot in Fig. 3.26 exhibits the experimental spot size $d_M = \kappa \lambda F / D_M \approx 8.3 \mu\text{m}$ that corresponds to the effective aperture $D_M \approx 4.151$ cm for the AOC.

The calomel crystal has rather high refractive indices. For example, the main ones are about $N_O = 2.083$ and $N_E = 3.038$ at $\lambda = 405$ nm used during the experiments. This is why one can expect significant optical attenuation inside the crystal and remarkable reflections from the facets of calomel-based AOC. Undoubtedly, to minimize potential optical losses the facets of similar AOC ought to have anti-reflection coating as it had been noted in the introduction. Nevertheless, we had performed our proof-of-principle experiments with the AOC that had not been coated. Therefore, the relative efficiency of light scattering into the second order had been first experimentally estimated and then measured at the output facet of the AOC. In so doing, the light intensity detected at the output facet, transmitted through the cell in the absence of an external UHF electronic excitation, had been counted as the unity. The light intensity scattered into the second order in the presence of that electronic signal and measured at the output facet had been considered as the usable optical signal caused by UHF electronic signal. The ratio of this usable optical signal to the initially transmitted light intensity (both are measured at the output facet of that AOC), one can consider as the relative efficiency of light scattering. Thus the relative efficiency, determined as it has been described above, had been measured at the optimal acoustic frequencies about $f_0 \approx 57.8$, 71.0, and 82.6 MHz as well as at $\lambda = 405$ and 633 nm. The maximum relative efficiency at the optimal acoustic frequency about 82.6 MHz and $\lambda = 405$ nm had been experimentally estimated by the value ~ 0.93 .

Figure 3.26 demonstrates the light intensity profile of a resolvable spot, which is a result of the standard processing provided by computer software accompanying the CCD-camera. One can see in Fig. 3.26 that full width at a 0.405-level of maximum of the main lobe can be estimated by about of 8.3 microns.

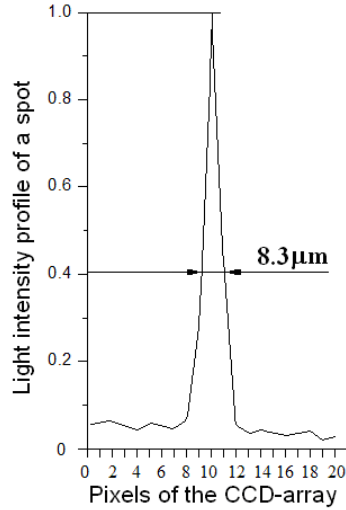


Fig. 3.26 Light intensity profile of an individual resolvable spot for the calomel-based AOC at $\lambda = 405$ nm.

The last data show that about 20% of the active optical aperture of the AOC is lost due to imperfectness of the lens and AOC's crystalline material together with the total effect of linear acoustic losses $B = 8$ dB per aperture. Therefore, instead of theoretical limit of the frequency resolution $\delta f_{Th} = V / 2D \approx 3.337$ kHz, one yields the measured value $\delta f_M = V / 2D_M \approx 4.18$ kHz, which leads to the experimentally obtained spectral resolution $\delta \lambda_M = \lambda \delta f_M / f_0 \approx 0.205$ Å. at $\lambda = 405$ nm. Then, $\Delta \lambda_M = \Delta f_M \lambda / f_0 \approx 140.0$ Å (instead of the theoretical value $\Delta \lambda_{Th} \approx 104.47$ Å because of damping the piezoelectric transducer). Thus the experimentally obtained number of resolvable spots is $N_M = \Delta f_M / \delta f_M = \Delta \lambda_M / \delta \lambda_M \approx 683$ spots.

In Table 3.5, the comparison of theoretical and experimental results is presented. One can see that some experimentally obtained data, namely, the frequency and spectral bandwidths as well as the numbers of resolvable spots exhibit general tendency to exceed the above-calculated theoretical values. This tendency takes place despite the presence of natural imperfectness peculiar to all the optical components in our experimental set-up. Similar results can be attributed to the use of damping the piezoelectric transducers in the developed AOC.

Table 3.5. Comparison of theoretical and experimental data; $\delta f_{Th} \approx 3.337$ kHz and $\delta f_M \approx 4.18$ kHz.

λ , nm	f_0 , MHz	Δf_{Th} , MHz	Δf_M , MHz	$\Delta \lambda_{Th}$, Å	$\Delta \lambda_M$, Å	$\delta \lambda_{Th}$, Å	$\delta \lambda_M$, Å	N_{Th}	N_M
405	57.8	3.045	4.129	213.36	289.3	0.23375	0.2929	913	988
	71.0	2.479	3.290	141.40	187.6	0.19035	0.2384	743	787
	82.6	2.131	2.856	104.47	140.0	0.16357	0.2049	639	683
633	57.8	1.837	2.605	201.15	285.3	0.36533	0.4578	571	623
	71.0	1.495	2.084	133.31	185.8	0.29751	0.3727	448	498
	82.6	1.285	1.796	98.49	137.6	0.25557	0.3203	385	430

Finally, the maximal expected lighted length in the focal plane of the integrating lens is $L_{CE} = d_M N_M < 9.0$ mm, i.e. capabilities of the experimental optical system lie in the frames of the exploited multi-pixel CCD-array. The obtained results with the developed calomel AOC (the spectral resolution $\delta \lambda_M \approx 0.205$ Å at 405 nm, which gives the resolving power exceeding $R_M = 19,800$ with the spectral bandwidth $\Delta \lambda_M \approx 140.0$ Å) have a gain compared with the most advanced to our knowledge, acousto-optical spectrometers for space or airborne operations of the twenty-first century [3.24-3.26]. Furthermore, one can take the other data from the recently obtained results [17] with calomel AOF (the spectral resolution was $\delta \lambda \approx 0.235$ Å at 405 nm, which gives the resolving power $R \approx 17,200$). By this it means that our new experimental result for the above-described calomel AOC (with the increased operation frequency and higher acceptable acoustic losses per optical aperture) can be considered as the best one can mention at the moment.

3.6.2.2 Second Maxima

Our proof-of-principal experiments had been performed with a wide-aperture Bragg AO cell based on the unique calomel ($\alpha\text{-Hg}_2\text{Cl}_2$) single crystal, which had an active optical aperture of about 52×2 mm, see Fig. 3.27. This pioneer AO cell allowed a maximum input acoustic power of about 20 W. It was able to operate over all the visible range starting from the optical wavelength $\lambda = 405$ nm, which combines the convenience of operating in just the visible range with the best-expected performances inherent in this AO cell. Practically, we used optical wavelengths $\lambda = 405$ and 442 nm from the single frequency solid-state lasers DPSS-405-SLM and DPSS-442-SLM (CrystaLaser). The CW-light radiation had linear state of the incident light polarization oriented almost along the crystallographic axis [110] of that AO cell. First, the calomel-based AO cell was prepared to be governed by the radio-wave signals at the central frequency $f_0 \approx 50.1$ MHz and then, after re-polishing and re-arranging the piezoelectric transducer, at the central frequencies $f_0 \approx 57.8$ and 64.66 MHz. A set of electronic equipment for both generating and registering the corresponding electric ultra-high-frequency (UHF) radio-wave signals had been exploited. Initially, the tunable UHF-signal was applied to the electronic input port of the AO cell through a wide-band UHF-amplifier HD19152 (0.15 – 230 MHz, 20 W) and the corresponding impedance-matching electronic circuits, see Fig. 3.27.

The optical part of our experiments included a 15-mm Glan-Taylor linear polarizer (the extinction ratio $\sim 10^5$, Thorlabs) and a four-prism (Edmund Optics) beam expander, which operated with the coherent light beams polarized in the plane of expanding and provided rather flat (non-uniformities were better than $\sim 10\%$) optical beam profiles. During the experiments with the beam shaper rather accurate angular adjusting of the incident light beams had been achieved. By this it means that both the correct Bragg angles of incidence and the needed tilt angles had been optimized. The 3-inch achromatic doublet lens (Edmund Optics) with the focal length of about 85 cm had been used as the integrating lens, and the multi-pixel CCD-linear array (Toshiba) consisting of $4.7 \mu\text{m}$ pixels was playing the role of a photo-detector. The layout of the experimental set-up is presented in Fig. 3.27, where only the 2-nd order of light scattering pattern is shown.

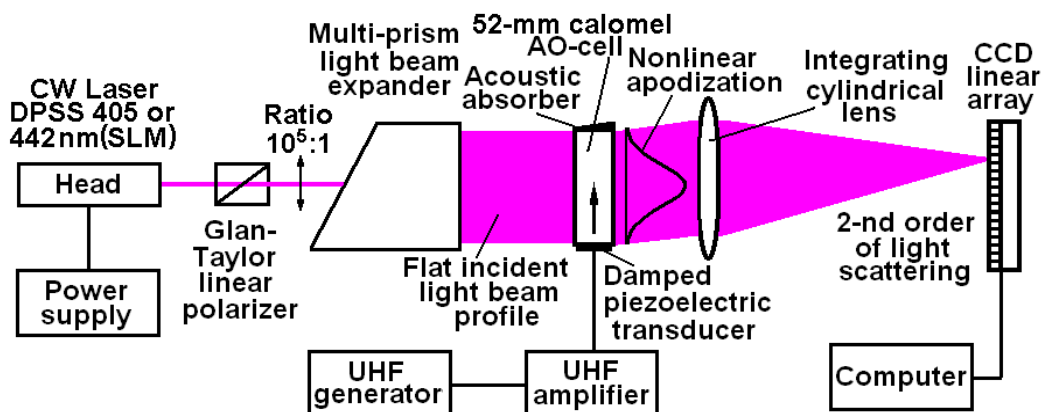


Fig. 3.27. A layout of the experimental set-up; only the 2-nd order of light scattering is depicted.

The optical part of our experiments included a 15-mm Glan-Taylor linear polarizer (the extinction ratio $\sim 10^5$, Thorlabs) and a four-prism (Edmund Optics) beam expander, which operated with the coherent light beams polarized in the plane of expanding and provided rather flat (non-uniformities were better than $\sim 10\%$) optical beam profiles. During the experiments with the beam shaper rather accurate angular adjusting of the incident light beams had been achieved. By this it means that both the correct Bragg angles of incidence and the needed tilt angles had been optimized. The 3-inch achromatic doublet lens (Edmund Optics) with the focal length of about 85 cm had been used as the integrating lens, and the multi-pixel CCD-linear array (Toshiba) consisting of $4.7 \mu\text{m}$ pixels was playing the role of a photo-detector. The layout

of the experimental set-up is presented in Fig. 3.27, where only the 2-nd order of light scattering pattern is shown.

The experiments consisted of two parts. The first of them included detecting the frequency band-shape with a low oscillation damping, i.e. determining the effective bandwidth of the Bragg non-collinear two-phonon light scattering at a 0.405-level of light intensity. The second part of those experiments was related to estimating possible spectral resolution within involving this AO cell into the optical spectrum analysis.

It was done via measurements of individual resolvable spots in the focal plane of the integrating lens for the light deflected by into the second order of scattering. Figure 3.28 shows an example of the experimental trace for the frequency band-shape inherent in the calomel AO cell with the damped piezoelectric transducer at the central frequency about 57.8 MHz (the acoustic losses of 4 dB/aperture), which had been detected under lighting by the coherent violet light $\lambda = 405$ nm. The total experimental frequency bandwidth at a 0.405-level of light intensity has been estimated by $\Delta f_M \approx 6.815$ MHz.

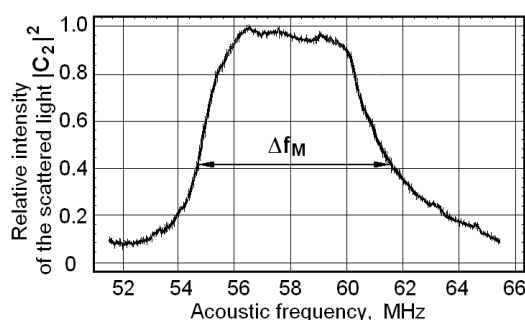


Fig. 3.28. Experimentally obtained frequency band-shape of the calomel-made AO cell at $f_0 \approx 57.8$ MHz and $\lambda = 405$ nm.

Precise optical measurements had been performed at two wavelengths 405 and 442 nm to obtain sufficiently reliable estimations for the frequency resolution provided by the calomel AO cell together with the above-described optical system, including the CCD linear array. The performed measurements had been done in the regime of the so-called “hot cell”, i.e. with a radio-wave signal applied at the input port of the α - Hg_2Cl_2 -cell. Figure 3.29 depicts the intensity profile with the spot size of about 9.98 microns, which include suppressing side lobes (theoretically) down to about -27 dB due to the effect of non-linear apodization with $\beta \approx 6$. The measurements showed that the main lobe of a spot gave lighting about two pixels of the CCD-row that provided acceptable resolution of a pattern from viewpoint of the sampling theorem.

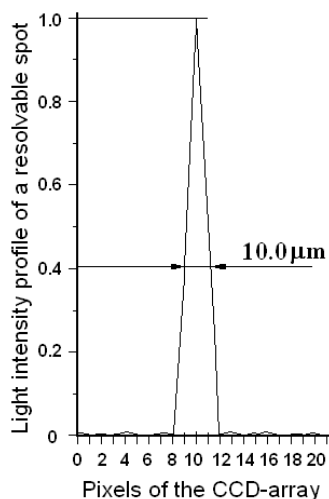


Fig. 3.29. Light intensity profile of an individual resolvable spot for the calomel-based AO cell at $\lambda = 405$ nm.

As it had been noted, our experimental results have been obtained using the integrating lens with $F = 85$ cm at the wavelength 405 nm, so that theoretically the spot size is $d_T = \kappa \lambda F / D \approx 8.262 \mu\text{m}$ with $\kappa \approx 1.248$. Together with this, the plot in Fig. 18 exhibits the experimental spot size $d_M = \lambda F / D_M \approx 9.980 \mu\text{m}$ that corresponds to the aberration factor $\zeta_M \approx 1.208$ (which includes various optical demerits of the system), and consequently, to the effective aperture $D_M = \lambda F / d_M \approx 3.45$ cm for the AO cell.

The calomel crystal has rather high refractive indices. For example, the main ones are about $N_O = 2.083$ and $N_E = 3.038$ at $\lambda = 405$ nm used during the experiments. This is why one can expect significant optical attenuation inside the crystal and remarkable reflections from the facets of calomel-based AO cell. Undoubtedly, to minimize potential optical losses the facets of similar AO cell ought to have anti-reflection coating as it had been noted in the introduction. Nevertheless, we had performed our proof-of-principle experiments with the AO cell that had not been coated. Therefore, the relative efficiency of light scattering into the second order had been first experimentally estimated and then measured at the output facet of the AO cell. In so doing, the light intensity detected at the output facet, transmitted through the cell in the absence of an external UHF electronic excitation, had been counted as the unity. The light intensity scattered into the second order in the presence of that electronic signal and measured at the output facet had been considered as the usable optical signal caused by UHF electronic signal. The ratio of this usable optical signal to the initially transmitted light intensity (both are measured at the output facet of that AO cell), one can consider as the relative efficiency of light scattering. Thus the relative efficiency, determined as it has been described above, had been measured at the optimal acoustic frequencies about $f_0 \approx 50.1, 57.8,$ and 64.66 MHz as well as at $\lambda = 405$ and 442 nm. The maximum relative efficiency at the optimal acoustic frequency about 57.8 MHz and $\lambda = 405$ nm had been experimentally estimated by the value ~ 0.91 .

As it had been noted before, the effect of acoustic losses in a medium leads only to scaling the nonlinear distributions along the dimensionless coordinate σx . Equation (3.2) describes a regular sequence of the unit-level maxima whose periodicity depends on the parameter $a = \alpha z$, and it can be applied to the case of using the acoustic frequency $f_0 \approx 57.8$ MHz, which leads to a regime with $a \geq 0$. Experimentally the distribution for the unit-level maxima has been registered at the constant central frequency $f_0 \approx 57.8$ MHz ($\alpha = 0.0885 \text{ cm}^{-1}$) with the fixed length $L = 0.2$ cm of interaction in the two different points of the AO cell's optical aperture. These points were related to the points $z_A \approx 2$ cm $z_B \approx 4$ cm. Varying the acoustic power parameter σ via variations of the applied electronic and acoustic power, one had obtained the needed magnitudes of σx . Even with $\sigma x = 10$ and $\sigma = 50 \text{ cm}^{-1}$ one has $P_2 \leq 1.12 \text{ W/mm}^2$. The corresponding plots combining theoretically calculated from Eq.(3.2) plots with the experimental points are presented in Fig. 3.30. The theoretical positions for all these unit-level maxima are determined by Eq.(3.3).

Figure 3.29 demonstrates the light intensity profile of a resolvable spot, which is a result of the standard processing provided by computer software accompanying the CCD-camera. One can see in Fig. 3.29 that full width at a 405-level of maximum of the main lobe can be estimated by about of ~ 10.0 (in fact 9.98) microns.

The last data show that about $1/3$ of the active optical aperture of the AO cell is lost due to imperfectness of the lens and AO cell's crystalline material together with the total effect of linear acoustic losses $B = 4$ dB per aperture. Therefore, instead of theoretical estimations of the frequency resolution $\kappa \delta f_{Th} = \kappa V / 2D \approx 4.1646$ kHz, one yields the measured value $\delta f_M = V / 2D_M \approx 5.031$ kHz, which leads to the experimentally obtained spectral resolution $\delta \lambda_M = \lambda \delta f_M / f_0 \approx 0.3525 \text{ \AA}$. at $\lambda = 405$ nm. Then, $\Delta \lambda_M = \Delta f_M \lambda / f_0 \approx 426.9 \text{ \AA}$. Thus the experimentally obtained number of resolvable spots is $N_M = \Delta f_M / \delta f_M = \Delta \lambda_M / \delta \lambda_M \approx 1211$ spots.

In Table 3.6, the comparison of theoretical and experimental results with the presence of nonlinear apodization is presented. One can see that some experimentally obtained data,

namely, the frequency and spectral bandwidths as well as the numbers of resolvable spots exhibit general tendency to exceed the above-calculated theoretical values. This tendency takes place despite the presence of natural imperfectness peculiar to all the optical components in our experimental set-up. Similar results can be attributed to the use of damping the piezoelectric transducers in the developed AO cell.

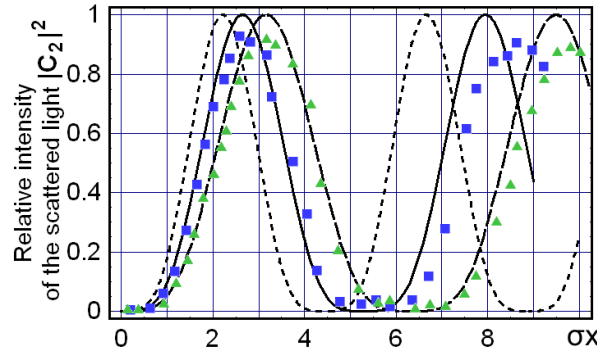


Fig. 3.30. Unit-level maxima vs. the dimensionless acoustic power parameter σx at $f_0 \approx 57.8$ MHz and $\eta x = 0$: dotted line (theory) is for $a = 0$; solid line (theory) and squares (experiment) are for $z_A \approx 2$ cm, $a = 0.177$; while dashed line (theory) and triangles (experiment) are for $z_B \approx 4$ cm, $a = 0.354$.

The obtained results with the developed regime in presence of nonlinear apodization with the calomel AO cell (the spectral resolution $\delta\lambda_M \approx 0.35$ Å at 405 nm, which gives the resolving power exceeding $R_M = 11,570$ with the spectral bandwidth $\Delta\lambda_M \approx 427$ Å and the number of resolvable spots $N_M \approx 1211$) have no formal gain in comparison with our previous data [3.27]. However, now we have much clearer understanding the details of physical processes within the phenomenon under consideration, which is accompanied by an important technical result. Namely, the obtained data include the nonlinear apodization, which reduce the first side lobes down to the level of about -27dB, i.e. exactly this level exhibits the initially achieved dynamic range of potential system for optical spectrum analysis without any additional facilities. The presented findings can be characterized as an updated and physically refined interpretation of recently presented data [3.27], which allows us to go to the heart of the matter under consideration.

Table 3.6. Theoretical and experimental data with nonlinear apodization for: $\delta f_{Th} \approx 3.337$ kHz with $\kappa \approx \{1.121, 1.248, 1.391\}$.

λ , nm	f_0 , MHz	Δf_{Th} , MHz	Δf_M , MHz	$\Delta\lambda_{Th}$, Å	$\Delta\lambda_M$, Å	$\kappa \frac{\delta\lambda_{Th}}{\text{Å}}$	$\delta\lambda_M$, Å	N_{Th}	N_M
405	50.1	6.934	7.813	560.5	631.7	0.3022	0.3651	1854	1730
	57.8	6.010	6.815	421.2	426.9	0.2918	0.3525	1443	1211
	64.66	5.372	6.070	336.5	380.2	0.2907	0.3512	1157	1083
442	50.1	6.028	6.878	529.4	606.8	0.3286	0.3969	1806	1529
	57.8	5.197	5.919	395.2	452.6	0.3170	0.3829	1557	1182
	64.66	4.607	5.238	314.5	358.1	0.3159	0.3816	1380	938

3.7 Conclusion

We have revealed novel physical aspects peculiar to square-law nonlinearity of the non-collinear two-phonon AOI governed by elastic waves of finite amplitude in birefringent crystals. This phenomenon manifests rather specific parametric nonlinearity within AOI, which can be observed at reasonable level of acoustic power density in some anisotropic materials exhibiting moderate linear acoustic losses. First, strongly nonlinear behavior of both the transmitted light intensity and the angular-frequency mismatch had been distinguished. Then, these characteristics had been studied theoretically. A sequence of the local unit-level maxima and a variety of the transfer function profiles peculiar to these maxima in the distribution of light scattered into the second order had been identified and considered. As a result, the second unit-level maximum, providing one of the widest profiles for the transfer function, had been selected.

Potential application of this profile is related to a unique option for the precise spectrum analysis of optical signals. Then, we have found, identified, and characterized an additional degree of freedom related to the non-collinear two-phonon AOI, which means the following possibility. Namely, the two-phonon processes allow close to 100% efficiency with the fixed optical wavelength for various acoustic frequencies as well as with the fixed acoustic frequency for various optical wavelengths due to existence of an additional dispersive birefringence factor inherent in this phenomenon, see Fig. 3.5. Because of the interplay between the scattered light waves and the incident ones is linear in behavior in spite of strong acousto-optical non-linearity peculiar to the non-collinear two-phonon AOI, we have chosen this effect to apply it to realize an advanced optical spectrum analysis with the doubled accuracy. By this it means that the second possibility, namely, the case with the fixed acoustic frequency for various optical wavelengths, had been taken in a view of developing a new approach to the parallel spectrum analysis of optical signals. Moreover, due to two-phonon processes give doubling the spectral resolution in the acousto-optics, the spectrum analysis of optical signals with the significantly improved resolution has been obtained as well.

Usually, the spectral resolution of, for example, collinear tunable acousto-optical filter depends on the birefringence of the exploited crystal, which is fixed as a basic parameter of the chosen material. The approach under proposal makes it possible to replace that physically limited and the fixed birefringence of a crystal by the new relatively larger birefringence factor, inherent in square-law nonlinearity of the non-collinear two-phonon AOI. Moreover, this factor of birefringence can be varied through choosing the above-described tilt angle whose acceptability depends on the symmetry of a crystal. In these circumstances, already only the acoustic attenuation plays the role of a limiting factor, which restricts potential performances of spectrum analysis. In our case, a 6-dB level of the acoustical losses per optical aperture of the AOC had been motivated and taken to avoid unnecessary strong limitations during the current stage of investigations.

To demonstrate the details of our analysis and to realize possible experiments the crystals of tetragonal symmetry had been considered as examples. Then, very effective acousto-optical material, i.e. the calomel (α -Hg₂Cl₂) single crystal had been selected as one of the best options for our goals. The needed theoretical, practical, and pre-experimental estimations had been performed to design a really unique wide-aperture AOC based on the calomel crystal. The experiment had been carried out at $\lambda = 405$ nm with a 5.2 cm aperture AOC made of calomel exited by the slow shear acoustic mode along the [110]-axis. Along with this, we had explored the use of rather specific directions for the optical waves in order to select adequate refractive indices within the AOI. The results of the performed proof-of-principal experiments with this AOC, governed by elastic waves of finite amplitude, confirm in general the previously developed theoretical analysis and numerical estimations. Moreover, these results open the way to the application of the proposed innovative technique to an advanced optical spectrum analysis with the radically improved spectral resolution.

Then, we have made a new step in characterizing an advanced nonlinear regime of the non-collinear two-phonon light scattering. Namely, in addition to already studied by us behavior of acousto-optical nonlinearity in the vicinity of the first (with $m = 1$) unit-level maximum now an area near the second unit-level maximum (with $m = 2$) has been investigated comprehensively. For this purpose, in parallel with previously presented analytical description of this phenomenon, the inspection in the amplitude and frequency domains has been developed to refine somewhat our previous considerations. It had been demonstrated that an area of the second unit-level maximum exhibits almost the widest band-shape of two-phonon light scattering and consequently gives the spectral (and frequency) bandwidth exceeding the regime with $m = 1$ by about two times. Additional broadening of the spectral bandwidth had been achieved experimentally due to exploiting the damped piezoelectric transducer at the cost of the operation efficiency in part. Together with these aspects, the effect of nonlinear apodization has been revealed in full measure within the regime with $m = 2$ during the investigations carried out.

This effect appears due to a combined action of the revealed acousto-optical nonlinearity and the linear acoustic losses in crystalline material of AO cell. The obtained nonlinear apodization is able to reduce the first side lobes down to the level of about -27 dB. In other words, exactly this level exhibits the initially achieved dynamic range of potential system for optical spectrum analysis of high spectrum resolution without any additional facilities.

The obtained data, achieved with the calomel-made AO cell (namely, the spectral resolution $\delta\lambda_M \approx 0.35 \text{ \AA}$ at 405 nm, the resolving power exceeding $R_M = 11,570$ within the spectral bandwidth $\Delta\lambda_M \approx 427 \text{ \AA}$) in the presence of nonlinear apodization, have no formal advantages over our previous results [3.17]. Nevertheless, now we have much better understanding of the features specific to physical processes within the regime of two-phonon light scattering, which leads to practically useful conclusions [3.28-3.31]. These inferences have been confirmed by the developed analysis and our proof-of-principle experiments.

4. Three-phonon acousto-optical interaction

The unexpected features of square-law nonlinearity inherent in the non-collinear three-phonon acousto-optical interaction controlled by elastic waves of finite amplitude in birefringent crystals with linear acoustic attenuation are distinguished and investigated. They lead to breakthrough applications of strongly nonlinear three-phonon interaction to linear optical spectrum analysis with ~100% efficiency and qualitatively improved resolution. Principally new physical degree of freedom, unique for this nonlinear phenomenon, is revealed and characterized. The indispensable theoretical developments and proof-of-principle acousto-optical experiments with specially designed wide-aperture tellurium dioxide cell are presented. The obtained experimental results confirm the elaborated approaches promising potentially the highest possible spectral resolution that one can expect in principle from acousto-optical technique within optical spectrum analysis.

4.1. Introduction

Strongly nonlinear behavior of light beams within Bragg acousto-optical interaction (AOI) in an anisotropic medium with linear acoustic attenuation can be experimentally detected without any observable effect of the AOI process on an elastic wave. We study the case when similar process is governed by the elastic wave of finite amplitude exhibiting the linear attenuation. In this case, the elastic wave amplitude is described by an independent non-homogeneous (due to the linear acoustic losses) wave equation in a given field approximation, while light beams amplitudes are governed by a set of combined differential equations with square law nonlinearity. This acousto-optical (AO) nonlinearity is parametric by its nature; the elastic wave amplitude controls it. Usually, the Bragg AOI incorporates conserving both the energy and the momentum for each partial act of a three-particle interaction. When the central cross-section of two wave vector surfaces, reflecting two eigen-states of light polarization in optically anisotropic media, is crossed by the direct line, placed close enough to a joint center of those surfaces and being collinear to the wave vector of an elastic wave, one can obtain up to four points of intersection [4.1]. This fact indicates that the chosen geometry of AOI in anisotropic medium allows, as a maximum, the four-orders of light deflected by an elastic wave in the Bragg regime. In the particular case, when these four intersections are equidistant, a four-order AOI can be provided by only one harmonic elastic (i.e. acoustic) wave, as it is shown for a uniaxial tellurium dioxide crystal in Fig. 4.1a. By this is meant that, under certain conditions, i.e. at the exactly chosen angle of light incidence on the selected crystal cut and at fixed frequency of the acoustic wave, it will be possible to realize the Bragg AOI caused by sequential participation of the first, second, and third phonons. As a result, a three-phonon AOI will be observed.

Historically, this phenomenon had been revealed in 80s past century [4.2] and then studied additionally [4.3, 4.4]. Time to time some non-systematic theoretical attempts had been undertaken in a view of considering potential applications of this phenomenon to performing various logic-based operations all-optically [4.5]. Such a place of three-phonon AOI can be easily explained first of all due to its strongly nonlinear nature and the nonlinear behavior of light beams within this regime of interaction. Together with this, the three-phonon AOI was traditionally mentioned together with the two-phonon anomalous AOI for crystallographic orientation in the vicinity of an optical axis in the tellurium dioxide crystal. However, availability of the corresponding vector diagram does not guarantee the effective process of such an AOI in a material. Recently [4.1], it has been demonstrated that within that geometry

the three-phonon AOI has very low efficiency in tellurium dioxide due to almost zero efficiency inherent in the middle step of AOI, which is normal in its physical nature.

The prime objectives of our studies are to reveal physically new features inherent in the nonlinearity of three-phonon AOI controlled by elastic waves of finite amplitude. We clarify the details of this nonlinearity both theoretically and experimentally in wide-aperture crystals with moderate linear acoustic attenuation and analyze the principle opportunity of applying this phenomenon to the optical spectrum analysis with the considerably (about three times) qualitatively advanced spectral resolution. Identifying a sequence of the local unit-level maxima in the distribution of light scattered into the third order, which occur as the acoustic power density grows, gives a chance to optimize the transmission function profile specific to each maximum. Fortunately, already the first maximum has really desirable profile of transmission function at the fixed angle of incidence for the incoming light beam with a wide optical spectrum.

Then, we deduce that non-collinear three-phonon AOI can have ~100% efficiency due to an additional birefringence factor, distinguished within this nonlinear phenomenon. It can be achieved at the fixed optical wavelength for a wide spectrum of acoustic frequencies or at the fixed acoustic frequency for a wide range of optical wavelengths. However, only the second option provides linearity between the input and output signals, i.e. linear dependence of the scattered light intensity on the incident one, within strongly nonlinear three-phonon AOI, which is able additionally to treble the spectral resolution, see Fig. 4.1b. This is why we choose the second option with the fixed acoustic frequency promising a breakthrough approach to AO technique of the pattern optical spectrum analysis with greatly progressed spectral resolution. Thus one has to note that similar approach demonstrates a pioneer possibility to apply the non-collinear three-phonon AOI to practical usage for the first time to our knowledge. Such a possibility is demonstrated at first theoretically for the tellurium dioxide (TeO₂) crystal of tetragonal symmetry as an example. Then, it is confirmed during the proof-of-principle experiments with a specially designed unique wide-aperture acousto-optical cell (AOC), based on the tellurium dioxide crystal and governed by acoustic waves of finite amplitude with linear acoustic attenuation.

4.2. Three phonon acousto-optical interaction

4.2.1. General solution

Let us start from the cross-sections of surfaces for the wave vectors describing the three-phonon AOI in crystals, see Fig. 4.1. Strongly nonlinear behavior of optical components with the Bragg AOI in anisotropic medium can be achieved in usual experiment without any observable influence of the scattering process on the acoustic wave. In this case the amplitude of acoustic wave is governed by a wave equation that includes the linear acoustic attenuation. Usually, the Bragg AOI incorporates conserving both the energy and the momentum for each partial act of a one-phonon light scattering [4.6], but one has to take into account both angular and frequency mismatches in the wave vectors of interacting waves.

Under certain conditions, i.e. at well-determined angle θ_0 of light incidence on selected crystal cuts and at specifically chosen fixed frequency of acoustic wave, one can observe Bragg scattering of the light caused by participating three phonons and the conservation laws are given by $v_1 = v_0 + f_3$, $\vec{k}_1 = \vec{k}_0 + \vec{K}$, $v_2 = v_0 + 2f_3$, $\vec{k}_2 = \vec{k}_0 + 2\vec{K}$, $v_3 = v_0 + 3f_3$, and $\vec{k}_3 = \vec{k}_0 + 3\vec{K}$ simultaneously (v_m , \vec{k}_m and f , \vec{K} are the frequencies and wave vectors of light and acoustic waves, $m = 0, 1, 2, 3$) [2].

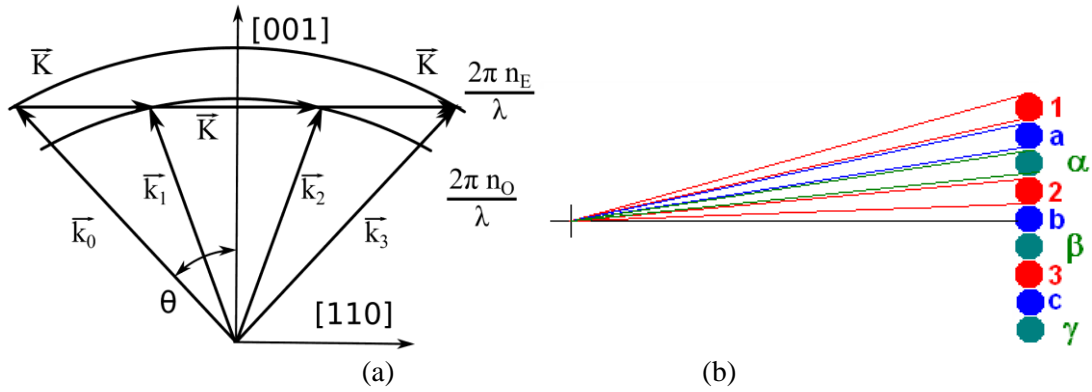


Fig. 4.1. The non-collinear three-phonon AOI vector diagram (a) and scheme of tripling the spectral resolution (b). Spots 1, 2, 3, ... are related to a one-phonon AOI, the additional spots a, b, c, ... describe a two-phonon AOI, while the extra-spots α , β , γ , ... correspond to the three-phonon AOI refining the spectral resolution.

Such a five-wave process occurs at the frequency f_3 of acoustic wave, peculiar to the three-phonon AOI, which can be geometrically found directly from Fig. 1a, as

$$f_3 = \lambda^{-1} V b_3, \quad (4.1)$$

where $b_3 = (0.5 |n_E^2 - n_O^2|)^{1/2}$ is the dispersive birefringence factor and $n_E \neq n_O$ are the current (and still not quite well determined) refractive indices of a crystal, V is the ultrasound velocity, λ is the incident light wavelength. The polarization states of light in various orders of scattering can be orthogonal to each other, whereas the frequencies of light beams in the first, second, and third orders are shifted by f_3 , $2f_3$ and $3f_3$ relative to the zero order light beam. The optimal angle for light incidence θ is given by $\sin \theta = 3 (2 |n_E^2 - n_O^2|)^{1/2} / (4n_O)$.

Originally equations for the complex amplitudes $C_m(x)$ of light waves ($m = 0, 1, 2, 3$), appearing due to a quasi-stationary three-phonon Bragg light scattering by an acoustic wave of the amplitude U , are given by [2]

$$\begin{aligned} \text{a) } \frac{dC_0}{dx} &= -q_a U C_1 \exp(-i\eta_0 x), \\ \text{b) } \frac{dC_1}{dx} &= q_a U C_0 \exp(i\eta_0 x) - q_n U C_2 \exp(-i\eta_1 x), \\ \text{c) } \frac{dC_2}{dx} &= q_n U C_1 \exp(i\eta_1 x) - q_a U C_3 \exp(-i\eta_2 x), \\ \text{d) } \frac{dC_3}{dx} &= q_a U C_2 \exp(i\eta_2 x). \end{aligned} \quad (4.2)$$

The coordinate x is directed orthogonally to the acoustic beam propagation, i.e. almost along the direction of all the light beams passing. Products of the factors $q_{n, a}$ of AOI for normal and anomalous light scattering, respectively, and the acoustic wave complex amplitude U can be expressed as $\sigma_{n, a} = q_{n, a} U = \pi (M_2^{(n,a)} P/2)^{1/2} / (\lambda \cos \theta)$. The constant angular-frequency mismatches $\eta_m = k_{m, x} - k_{m+1, x}$ are explained in terms of x -components for light wave vectors. However, in the case related to acoustic wave of finite amplitude in a medium with the linear acoustic losses, Eq.(4.2) has to be complemented by a wave equation for the complex amplitude $U(z, t)$ of a slow acoustic wave

$$\frac{\partial U}{\partial z} + \frac{1}{v} \frac{\partial U}{\partial t} = -\alpha U, \quad (4.3)$$

passing exactly along the axis z associated with optical aperture of an AOC. Here, the axis z is orthogonal to the axis x , v is the velocity of that acoustic wave, and the factor α describes the linear acoustic attenuation.

The simplest boundary conditions $|C_0(x=0)|^2 = I$, $C_{1,2,3}(x=0) = 0$ and exploit the conservation law $|C_0|^2 + |C_1|^2 + |C_2|^2 + |C_3|^2 = I$, resulting from Eq.(2), where I is the intensity of continuous-wave incident light beam. Then, one can use the relations $\eta_0 \equiv \eta$, $\eta_1 = 3\eta$, and $\eta_2 = 7\eta$ [2] to obtain the evolution equation for the complex amplitude $C_3(x)$ of the light scattered into the third order

$$\begin{aligned} & \frac{d^4 C_3}{dx^4} - 28i\eta \frac{d^3 C_3}{dx^3} + [\sigma_n^2 + 2\sigma_a^2 - 239\eta^2] \frac{d^2 C_3}{dx^2} + \\ & i\eta[644\eta^2 - 11\sigma_n^2 - 28\sigma_a^2] \frac{dC_3}{dx} + \sigma_a^2 [\sigma_a^2 - 110\eta^2] C_3 = 0. \end{aligned} \quad (4.4)$$

with the boundary conditions $C_3(x=0) = (dC_3/dx)(x=0) = (d^2C_3/dx^2)(x=0) = 0$ and $(d^3C_3/dx^3)(x=0) = \sigma_n \sigma_a^2$. It is seen that the ratio $\chi = \sigma_n/\sigma_a$ reflects the properties of an AO-material in the chosen direction of acoustic wave propagation and plays very important role here.

4.2.2. Transmission function without acoustic losses

First, we analyze Eqs. (4.2) and (4.3) with an ideal lossless case, when $\alpha = 0$ and the acoustic wave has a constant amplitude $U \equiv U_0$ along the optical aperture of an AOC. At the absence of any mismatch $\eta = 0$, one yields

$$C_3(x) = \frac{\sqrt{2}}{\sqrt{4+\chi^2}} \left\{ \frac{\sin \left[\frac{\sigma_a x}{\sqrt{2}} \sqrt{2+\chi^2 - \chi\sqrt{4+\chi^2}} \right]}{\sqrt{2+\chi^2 - \chi\sqrt{4+\chi^2}}} - \frac{\sin \left[\frac{\sigma_a x}{\sqrt{2}} \sqrt{2+\chi^2 + \chi\sqrt{4+\chi^2}} \right]}{\sqrt{2+\chi^2 + \chi\sqrt{4+\chi^2}}} \right\}. \quad (4.5)$$

At $\eta \neq 0$, one can calculate the following 3D- and 2D-plots with $q_a = 1.00$ and $q_n = 1.15$. It is seen that the ratio $\chi = \sigma_n/\sigma_a$ reflects the properties of an AO-material in the chosen direction of acoustic wave propagation and plays very important role here. Figure 4.2a exhibits a sequence of the unit level maxima, whose widths of profiles are increasing as the dimensionless coordinate $\sigma_a x$ grows.

A pair of 2D-plots with $\eta = 0$ in Fig. 4.2b shows that when $\chi = 1.15$ (solid line) one can see a sequence of the unit level maxima, but when, for example $\chi = 1.0$ (dashed line), this sequence becomes destroyed rather fast as the parameter χ is varied. Nevertheless, the first maxima for both these cases are very close to one another.

Initially, let us concentrate our attention on the dynamics (behavior) of the first maximum, which is the narrowest in Fig. 4.2a, but it can be achieved simpler than the others due to relatively low level of the acoustic power density required for its achievement. Whereas one of the important factors, affecting the magnitude of this maximum and determining the needed acoustic power, is the ratio χ . Figure 4.3 represents a set of 2D-plots reflecting the dependences of light intensity, scattered into the first maxima inherent in the three-phonon AOI, with various ratios χ lying between 0.5 and 2.0.

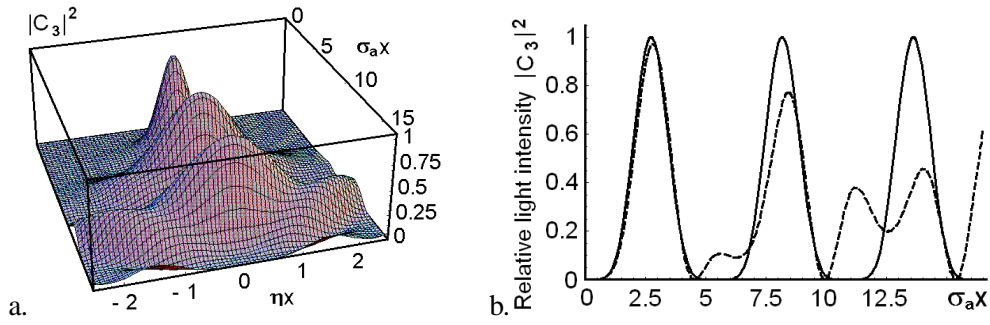


Fig. 4.2. Relative light intensity $|C_3|^2$ distributions: (a) 3D-plot in the coordinates $\sigma_a x$ and ηx ; (b) a pair of 2D-plots with $\eta = 0$; when $\chi = 1.15$ (solid line) one can see a sequence of the unit level maxima, but when, for example $\chi = 1.0$ (dashed line), this sequence becomes destroyed.

The analogous 3D-plot is depicted in Fig. 4.3c. These 2D-plots predict that choosing the exact value $\chi = 1.15$ is maybe not too critical for experimental verification of our analysis. This is rather important deduction because the ratio χ is usually the property of a material, which can be varied not easily. The plots in Fig. 4.4 show a triplet of the first transmission functions inherent in the non-collinear three-phonon light scattering.

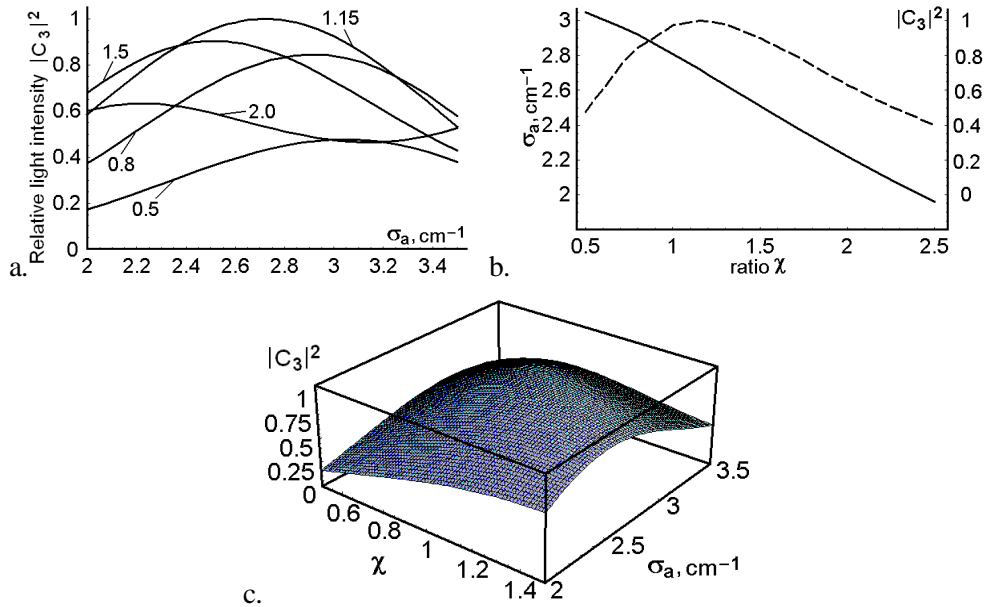


Fig. 4.3. Relative light intensity $|C_3|^2$, scattered into the first maxima inherent in the three-phonon AOI, with various ratios χ lying between 0.5 and 2.0 due to the acoustic power density described by σ_a with $\eta = 0$: a) $|C_3|^2$ vs. the parameter σ_a , b) $|C_3|^2$ vs. the ratio χ , the inter- relation between σ_a and χ is shown too, and c) The corresponding 3D-plot with various ratios χ lying between 0.5 and 1.5 due to the acoustic power density described by σ_a with $\eta = 0$.

It is seen that the first maximum exhibits the narrowest transmission function, but it can be observed at the lowest value of the dimensionless coordinate $\sigma_a x = 2.72$, which is the most attractive for applications associated with low-power signals. Figure 4.4 depicts the first transmission function of the width for $\sigma_a x = 2.72$ in detail; the whole width is equal to $\eta_\Sigma x = |\eta_- x + \eta_+ x| \approx 0.76$ at the 0.405-level. As before, we are using the level of 0.405 taken from the Rayleigh criterion [4.7] due to operating over sinc^2 signals. This level coincides also with the -4 dB level exploited as well.

Because of the mismatch had been originally [4.2] defined as $\eta = \pi \lambda f_3 (\Delta f)/(n_0 V^2)$, one can find that the frequency bandwidth of a three-phonon AOI at the 0.405-level is determined by

$$\Delta f \approx 0.76 n_o V^2 / (\pi \lambda f_3 L). \quad (4.6)$$

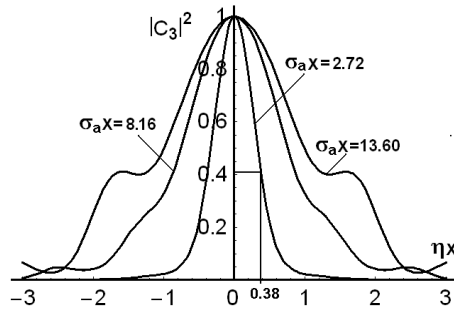


Fig. 4.4. Transmission functions i.e. relative light intensities $|C_3|^2$ distributions with $\eta \neq 0$ and $\chi = 1.15$ at the isolated points $\sigma_a x = 2.72, 8.16,$ and 13.60 specific to the unit-level maxima from Fig. 2b.

4.2.3. Transmission function with acoustic losses

In reality $\alpha \neq 0$, and Eq.(4.1c) has the general solution $U(z) = U_0 \exp(-\alpha z)$ in the tracking coordinates, while U_0 is now the initial magnitude of that acoustic wave. By this it means that the above-noted solution has to involve a dependence on the coordinate z as $\sigma_a = q_a U_0 \exp(-\alpha z)$ and to take the form $C_3(x, z)$. As a result, one arrives at the modified 3D-distribution similar to Fig. 4.2a and plots similar to Fig. 4.2b with $\eta x = 0$.

Now, one can consider additionally the dimensionless attenuation parameter $a = \alpha z$ describing the linear acoustic losses in a material. With separating the parameter, which includes two dimensionless coordinates $\sigma_a x$ and ηx , characterizing the acoustic power density and the frequency mismatch, as well as the above-included one $a = \alpha z$. Thus one can obtain the following 2D-distributions that should be interpreted using 3D-distribution in Fig. 4.1 for the cases of $a = 0$. These distributions show that growing the parameter $a = \alpha z \in [0, 0.3, 0.5]$ leads in fact only to scaling these distributions along the horizontal axis $\sigma_a x$ when $\eta x = 0$, see Fig. 5.

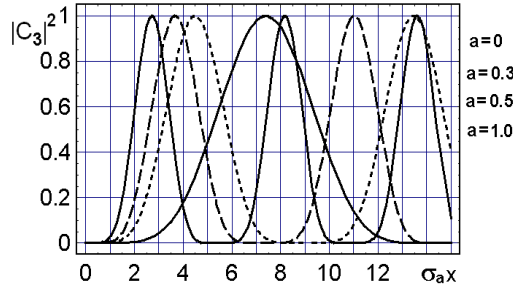


Fig. 4.5. The 2D-plots for relative light intensity $|C_3|^2$ distributions vs. in the dimensionless coordinate $\sigma_a x$ with $\eta = 0$ and $q_n/q_a = 1.15$; solid lines are for $a = 0$ and 1.0 , dashed line is for $a = 0.3$, and dotted line is for $a = 0.5$. One can see a sequence of the unit level maxima and the dynamics of scaling due to effect of linear acoustic losses.

4.3. Frequency of a three Phonon acousto-optical interaction

Now, we make a breaking-through step in theory of the non-collinear three-phonon AOI, see Fig. 4.6. This step can be represented in terms of two surfaces for the refractive indices of ordinary (see an internal dark sphere) and extraordinary (see an external bright ellipsoid) light waves ($N_E \geq N_O$) for a tetragonal crystal at the fixed optical wavelength λ . The parameters of both these surfaces can be varied depending on λ due to the expected dispersion of a crystal within the visible range. The vertical axis in Fig. 4.6 is oriented along the optical axis $[001]$, while two horizontal axes can be oriented depending on the chosen material and the exited elastic mode. Then, this figure includes a multi-vector diagram illustrating the three-phonon

AOI through the tilt angle, which use the same acoustic frequencies and birefringence factor b . The quartets of vectors, going from the geometric center of surfaces, represent the optical wave vectors describing the corresponding orders of AOI, whereas sequentially co-directed trio of the acoustic wave vectors represent three-phonon processes. This vector diagram reflects existence of the revealed here additional physical degree of freedom inherent in the nonlinearity of three-phonon AOI. In consequence of this degree of freedom one can exploit the fixed frequency f_3 to exert control over various optical wavelengths scattered through different angles. In this case, one has to consider two pairs of surfaces peculiar to the refractive indices of ordinary and extraordinary light waves for a tetragonal crystal and each similar pair of surfaces will correspond to an individual light wavelength λ . Nevertheless, each vector diagram for two different nonlinear processes of three-phonon AOI will include acoustic vectors \vec{K} of the same lengths characterizing the same acoustic frequency f_3 . To perform a three-phonon AOI at a given acoustic frequency one has to consider involving a tilt angle into geometry of similar AO process. In so doing, one has to select the concrete optical wavelength for an analysis. Tellurium dioxide is a uniaxial crystal, so that $n_o \equiv N_o$ is the main refractive index for the ordinary state of polarization, while n_e depends on a direction in a crystal and has the form of an ellipsoid, see Fig. 4.6. We are interested in tilts from the [001]-axis, therefore, one can consider the angle $\phi \in [0, \pi/2]$ of a tilt from the [001] axis, see Fig. 4.6.

Let us estimate the acoustic frequency required for three phonon AOI in a crystal, which can exhibit optical activity. For this matter we took the index surface equations for a positive uniaxial crystal in the form [4.4] of

$$\frac{n_{o,e}^2(\vartheta) \cos^2 \vartheta}{N_o^2 (1 \mp \delta)^2} + \frac{n_{o,e}^2(\vartheta) \sin^2 \vartheta}{N_{o,e}^2} = 1, \quad (4.7)$$

where $N_{o,e}$ and $n_{o,e}$ are the main and current ordinary and extraordinary refractive indices of a birefringent crystal, respectively; ϑ is the angle between the optical axis and the incident light beam. Then, one has the optical activity factor $\delta = 0.5 |1 - n_e(\vartheta = 0)/n_o(\vartheta = 0)|$ which characterizes the contribution from optical activity, so that $\delta = 0$ in the absence of optical activity. To simplify the calculations and visualization of the wave vectors diagram one can introduce the tilt angle ϕ between the optical axis and the plane of light scattering, see Fig. 4.6. Here, axes X and Y are taken depending on the real axes in a crystal.

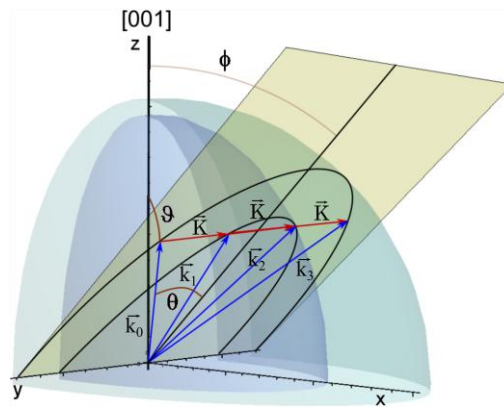


Fig. 4.6. Index surfaces for the ordinary refractive index (inner ellipsoid) and the extraordinary refractive index (outer ellipsoid). The two semi-ellipses represent the intersections of these ellipsoids with the plane of light scattering (yellow plane); declined by the tilt angle ϕ .

In the Cartesian coordinates, the equations for the index surfaces take the form

$$\frac{x^2}{N_{o,e}^2} + \frac{z^2}{N_o^2 (1 \mp \delta)^2} + \frac{y^2}{N_{o,e}^2} = 1 \quad (4.8)$$

for ordinary and extraordinary refractive indices, respectively. We resolve a set of Eqs.(4.8) relative to the variable y , because a trio of the acoustic wave vectors is lying in a sequence along this axis.

In so doing, one estimates the position, for which the distance of intersection with the internal surface will be the same as the distance between internal and external surfaces. In terms of the wave vector diagram (see Fig. 4.6), this condition is the requirement for the three-phonon light scattering to exist. This condition would be satisfied for several tilt angles and will give us the acoustic frequency required for three phonon AOI in a crystal. As a result, one yields a new formula for the acoustic frequency f_3 required for the three phonon AOI in a crystal, which can exhibit optical activity.

$$f_3 = \frac{2V}{\lambda(1-\delta)} \sqrt{\frac{N_O^2(\delta-1)^2 [4N_E^2\delta + (N_E^2 - N_O^2)(\delta^2-1)^2 \cdot \tan^2\phi]}{9N_O^2(1+\delta)^2 - N_E^2(\delta-1)^2 + 8N_O^2(\delta^2-1)^2 \cdot \tan^2\phi}}. \quad (4.9)$$

One can see from Eq.(4.9) that this frequency strongly depends on two parameters: the tilt angle ϕ and has the optical activity factor δ .

To make our consideration more concrete an appropriate AO crystalline material has to be selected for the further analysis. Within similar selection of a material, one has to say that there are not too many possibilities of exploiting either longitudinal or shear elastic modes, passing along various crystallographic directions. The analysis has shown that in fact only one material, namely, tellurium dioxide (TeO_2) single crystal, exhibiting the optical activity had been previously analyzed theoretically due to its crystal-physical properties and considered practically for performing any experiments oriented on a three-phonon AOI. In part, such a selection was historically motivated by very high efficiency of light scattering and not too high acoustic frequency needed for excitation of a three-phonon AOI in this material. This crystal belongs to the 422 – tetragonal symmetry group. It has spectral transmission band $\Delta\lambda = 0.35 - 5.0 \mu\text{m}$ and a pair of dispersive refractive indices, whose main values are $N_O = 2.3297$ and $N_E = 2.4956$ at the wavelength $\lambda = 488 \text{ nm}$ [4.8]; its material density is equal to $\rho \approx 6.0 \text{ g/cm}^3$ [4.9]. This crystal is potentially suitable for effective non-collinear three-phonon AOI and allows pure slow-shear elastic mode with the wave vector $\vec{K} \parallel [110]$, the displacement vector $\vec{u} \parallel [1\bar{1}0]$, the phase velocity $V_s \approx 0.616 \cdot 10^5 \text{ cm/s}$, and the acoustic wave attenuation factor $\Gamma \approx 290 \text{ dB/(cm GHz}^2)$, which gives the amplitude factor α of losses in the form of $\alpha (\text{cm}^{-1}) = 0.1152 \Gamma f^2$.

With $\delta \sim 10^{-4}$, Eq. (4.9) is plotted in Fig. 4.7 to appreciate the relations between the tilt angle ϕ and the acoustic wave frequency f_3 and the experimental data related to the ellipticity of the incident light beam in the particular case of the TeO_2 crystal working at $\lambda = 488 \text{ nm}$.

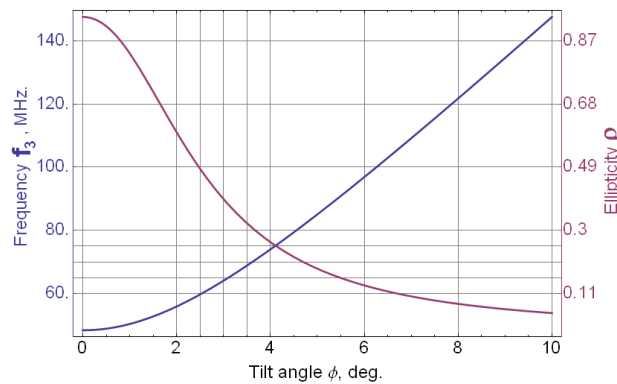


Fig. 4.7. Acoustic frequency and ellipticity of the incident light vs. the tilt angle ϕ needed for the three-phonon AOI in the TeO_2 crystal.

These parameters can be exploited to choose a balance between decreasing the central acoustic frequency (to minimize the effect of acoustic losses) and reducing the ellipticity of light beams

(to simplify conditions for potential experiments with TeO₂ crystal made AOC). One should take into account that reliable realization of a given value for the ellipticity in an AOI-area is not so easy during the experiment.

4.4. Photo-Elastic Effect in Tellurium dioxide

Generally, when the elastic wave is passing through a medium, the dielectric impermeability tensor $\hat{\kappa}$ becomes to be perturbed under action of mechanical deformations γ and takes the form $\hat{\kappa} + \zeta$, where the symmetrical tensor $\zeta = p \hat{\gamma}$ of the 2-nd rank represents small addition to the tensor $\hat{\kappa}$, while p is the tensor of the 4-th rank of photo-elastic coefficients and $\hat{\gamma}$ is the deformation tensor [4.10]. When the slow-shear acoustic mode is passing along the $[1\bar{1}0]$ -axis of a TeO₂-crystal and its displacement vector is oriented along the $[110]$ -axis, one can find $\zeta = p \hat{\gamma} = 0.5 (p_{11} - p_{12}) (\bar{x}_1 \cdot \bar{x}_1 - \bar{x}_2 \cdot \bar{x}_2)$ in the dyadic form. Then, it is well known that physical axes of the optical indicatrix determine a pair of eigen-vectors of the electric induction in a crystal. That is why the quadratic form $p_{eff} = \vec{d}^{(S)} \zeta \vec{d}^{(i)}$ describes the effective photo-elastic constant p_{eff} of AOI, i.e. the efficiency of converting the incident state of light polarization, described by the unit vector $\vec{d}^{(i)}$ oriented along the incident electric induction $\vec{D}^{(i)}$ into the scattered state of light polarization, characterized by the unit vector $\vec{d}^{(S)}$ oriented along the scattered electric induction $\vec{D}^{(S)}$. Now, one may exploit a reduced version of the addition matrix $\tilde{\zeta}$ instead of ζ , which is normalized by the factor $0.5 (p_{11} - p_{12})$ as well as \tilde{p}_{eff} normalized in the same way. Then, only the ellipticity ρ can reflect the angular declination from the optical axis for the light beams, because all the angles of incidence and scattering lie in a range of a few degrees. The reduced matrix of small additions represents a minor of the matrix ζ in the form $\tilde{\zeta} = \bar{x}_1 \cdot \bar{x}_1 - \bar{x}_2 \cdot \bar{x}_2 + i G_{33} (\bar{x}_1 \cdot \bar{x}_2 - \bar{x}_2 \cdot \bar{x}_1)$, which includes the optical activity. The value of G_{33} can be found experimentally for a TeO₂, so that [4.1] $G_{33} \approx 4.26 \times 10^{-5}$ at $\lambda = 488$ nm. Thus with conserving the polarization state ($i \rightarrow i$), i.e. within the normal AOI, as well as with changing the polarization state ($i \rightarrow j$), i.e. with the anomalous AOI, (here, $i, j = 1, 2; i \neq j$) one can find

$$\begin{aligned} \text{a) } |\tilde{p}_{eff}(i \rightarrow i)| &= p_n \approx \frac{1 - \rho^2 - 2\rho G_{33}}{1 + \rho^2}, \\ \text{b) } |\tilde{p}_{eff}(i \rightarrow j)| &= p_a \approx \frac{2\rho + (1 - \rho^2)G_{33}}{1 + \rho^2}, \quad \text{c) } \frac{q_n}{q_a} \approx \frac{1 - \rho^2 - 2\rho G_{33}}{2\rho + (1 - \rho^2)G_{33}}. \end{aligned} \quad (4.10)$$

The plots of the corresponding numerical estimations for these formulas vs. the ellipticity ρ are presented in Fig. 4.8.

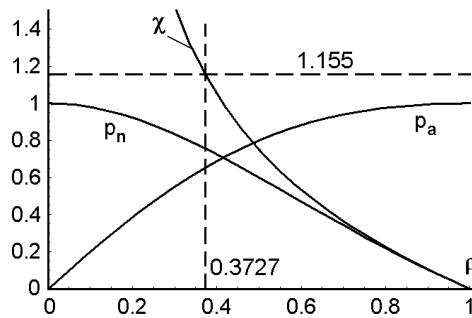


Fig. 4.8. Relations between the photo-elastic constants p_a and p_n .

One can find that the efficiency of normal light scattering ($p_n \approx 0.756$) exceeds the efficiency of anomalous one ($p_a \approx 0.655$) in a TeO₂-crystal at the chosen orientation with $\chi = |p_n / p_a| \approx 1.155$.

Namely, one has found the ellipticity $\rho \approx 0.37275$, which requires the declination angle $\vartheta \approx \phi \approx 3.142^\circ$ and the central acoustic frequency $f_3 \approx 65$ MHz.

4.5. The Nonlinear Apodization

At this point we will not motivate in detail our selection of the level B for linear acoustic losses per optical aperture D of the tellurium-dioxide-made AOC. Nevertheless, together with traditionally exploited value $B = 4$ dB [4.7], the values $B = 2.45 - 7.35$ dB will be taken as well in a view of principle possibility to correct them later by the needed apodization. Choosing these values allows us to avoid unnecessarily strong limitations for this stage of studies. More detailed analysis can be started proceeding from the optical aperture $D = 6.2$ cm of the AOC, restricted by an available sample of the chosen crystalline material. In an attempt of avoiding the effect of optical activity, one has to take the tilt angle 3.0° as a minimum and estimate the ellipticity by about of $\rho \approx 0.3727$ [4.4]. This choice gives the central acoustic frequency $f_3 \approx 65.0$ MHz at $\lambda = 488$ nm, the acoustic losses $\gamma \approx 1.225$ dB/cm and $\alpha \approx 0.1411$ cm⁻¹.

Taking the above-chosen central frequency f_3 , one can find the following levels of acoustic losses $B_k = D_k \Gamma f_3^2$ per the corresponding aperture D_k at this fixed frequency f_3 . Here, the index $k = \{2 - 6\}$ reflects the optical aperture of a crystal in centimeters. This approach differs from an algorithm of the analysis developed recently [4.11], because now exactly the central acoustic frequency f_3 and light wavelength λ are fixed, while the optical aperture is varied.

Since the phase velocity $V_S \approx 0.616 \cdot 10^5$ cm/s is already known, one can theoretically estimate the expected frequency $\delta f_{k,T} = V(3D_k)$ and spectrum $\delta \lambda_{k,T} = \lambda^2 / (3b D_k)$ resolutions (here, $b = f_3 \lambda / V$) for each aperture D_k , see Table 4.1.

For this set of the optical apertures D_k , the first unit level maxima can be reached at a set of the optimized values $(\sigma_a x)^{(k)}_{1,Opt}$ in such a way that both the falling down wings of the corresponding light intensity distributions $|C_3|^2$ have the levels $|C_3|^2_{min,K}$.

Table 4.1. Theoretical characterization of TeO₂ AOC.

D_k , cm	B_k , dB	$\delta f_{k,T}$, kHz	$\delta \lambda_{k,T}$, Å	$(\sigma_a x)^{(k)}_{1,Opt}$	$ C_3 ^2_{min,K}$	β_k	κ_k
2	2.45	10.27	0.771	3.105	0.86	0.302	1.0113
3	3.68	6.85	0.514	3.29	0.72	0.675	1.02443
4	4.9	5.13	0.385	3.47	0.56	1.16	1.04345
5	6.13	4.11	0.309	3.64	0.405	1.808	1.06867
6	7.35	3.42	0.257	3.82	0.28	2.546	1.0984

After performing the above-proposed optimization, one can use the found values of $(\sigma_a x)^{(k)}_{1,Opt}$, which provide more symmetric distributions presented in Fig. 4.9. An example of the corresponding 3D-distribution with the $D_4 = 4.0$ cm and $(\sigma_a x)^{(4)}_{1,Opt} \approx 3.47$ is presented in Fig. 4.10. Looking at these plots, one can find that the combined influence provided by acousto-optical nonlinearity and linear acoustic losses leads to the some equivalent apodization of initially flat incident light beam, see solid lines in Fig. 4.9.

To describe the Gaussian apodization for a flat incoming light beam with the field amplitude A_0 we use the approach based on the apodization parameter β and described previously [4.11].

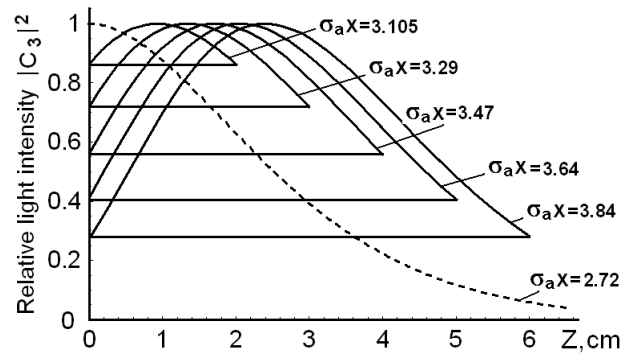


Fig. 4.9. Optimized 2D-profiles of the light distributions at the output facet of the tellurium dioxide-made AOC at $f_3 = 65.0$ MHz with $\alpha \approx 0.1411$ cm $^{-1}$ for the corresponding D_k (solid lines); the dashed line is for a non-optimized profile.

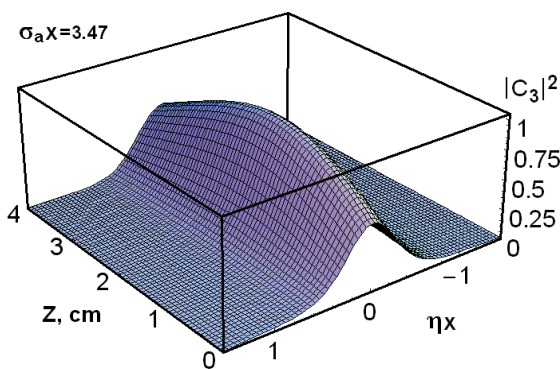


Fig. 4.10. An example of an optimized 3D-profile of the issuing light distribution at $f_3 = 65.0$ MHz and $(\sigma_a x)_{1,Opt}^{(4)} \approx 3.47$ with $D_4 = 4.0$ cm, and $\alpha \approx 0.1411$ cm $^{-1}$.

In the case of the apodization parameter $\beta \approx 0$, an ideal normalized profile of a resolvable spot has full width equal to unity in terms of the dimensionless coordinate $u = w D/\lambda F$ at the intensity level 0.405 in the focal plane of the integrating lens with the focal distance F . The required corrections to theoretical width of a resolvable spot, destroyed by the linear acoustic losses when $\beta \neq 0$, can be made using the correction factors κ . The needed values of these factors are: $\kappa_k \approx 1.01139, 1.02443, 1.04345, 1.06867, \text{ and } 1.09884$, i.e. the main lobe has broadening by about 1.14, 2.44, 4.35, 6.87, and 9.88 % due to the effect of linear acoustic losses for each β_k , respectively. Thus, the performed apodizations, provided by properties of an AOC near the first maximum, are not deep enough (they equal to -14 to -18 dB for the first side lobe) to improve significantly the dynamic range of potential optical spectrum analysis, see Fig. 4.11.

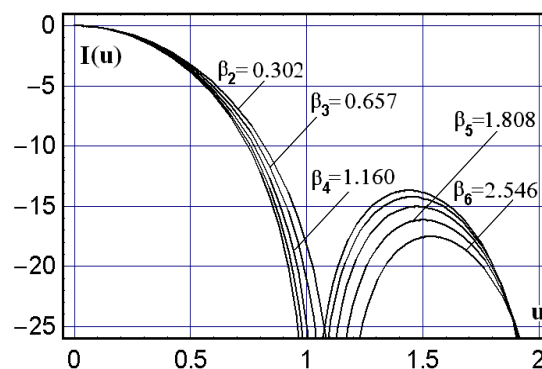


Fig. 4.11. Theoretical logarithmic profiles of resolvable spots with the dimensionless apodization parameters β_k .

4.6. Theoretical estimations of the tellurium dioxide cell

The length L and central frequency f_3 of Bragg AOI in a crystal are restricted by well-known inequality for the Klein-Cook parameter $Q = 2\pi\lambda L f^2/(n_0 V^2) \gg 1$ [4.12]. For the slow-shear acoustic mode passing along the $[1\bar{1}0]$ -axis in tellurium dioxide, one has $V = 0.616 \times 10^5$ cm/s and $n_0 \equiv N_0 \approx 2.3297$ at $\lambda = 488$ nm. With the above-chosen $f_3 = 65$ MHz, one can find $L_{\min} \gg 0.00685 Q$ cm. Taking the limiting value $Q = 4\pi$, as it had been recommended in Ref. [4.12], one yields $L_{\min} \gg 0.086$ cm. The value of L_{\min} is too small to be used practically. Such a small size of L would bring demerits for the piezoelectric transducer. One can mention the lack of robustness (like electrical, mechanical, and thermal ones) as well as potentially not enough efficiency of light scattering, which is directly conditioned by the size of the transducer. That is why we are forced to consider more appropriate size L , for instance, ten times larger. Consequently, at the frequency $f_3 = 65$ MHz one can use $L \geq 0.86$ cm and expect the Bragg character of AOI.

The acoustic beam diffraction can be considered via estimating the length Z of Fresnel zone for a radiating acoustic aperture R . These values are connected with one another as $Z = R^2 f_3/(2V)$ [4.13]. If it is granted that the acoustic beam belongs to Fresnel acoustic zone and $Z = 6.0$ cm at $f_3 \approx 65$ MHz, one can find that $R \approx (2V_s Z/f_3)^{1/2} \approx 0.107$ cm for TeO_2 . Thus with $R \geq 0.11$ cm, one can conclude that the expected angular divergence of acoustic beam is definitely small to be neglected. Consequently, the plane-wave approximation can be used for characterizing the acoustic beam propagation. The exact angular divergence of acoustic beam in the tellurium dioxide AOC at $f_3 \approx 65$ MHz can be estimated as well. A reliable spatial size of the initial acoustic beam aperture that we will consider is close to $L \sim 1.0$ cm. Then, one can calculate the angle of acoustic beam divergence $\nu = V/(f_3 L) \approx 9.5 \times 10^{-4}$ rad $\approx 0.0543^\circ$, which is very small.

The TeO_2 -crystal is extremely anisotropic material. Its acoustic anisotropy is illustrated by 2D-surfaces for the phase velocities in the (001)- and $(1\bar{1}0)$ -planes, see Ref. [4.10, chapter "Elasticity of crystals"]. It's shown there, that the slow-shear acoustic mode has the absolute minimum ($V = 0.616 \times 10^5$ cm/s) with passing along the $[1\bar{1}0]$ -axis. However, the quests for this minimum depend on the chosen plane and exhibit different (by about 3 times from one another) angular behavior. Generally, when an acoustic wave passes through an anisotropic medium, the energy flow can tip out of the wave vector $\vec{K} = K\vec{m}$, where \vec{m} is the unit vector of \vec{K} . Passing the energy flow is characterized by the group velocity vector $\vec{w} = w\vec{s}$, where \vec{s} is the corresponding unit vector, and the group velocity w is equal to the phase velocity V only if $\vec{s} \parallel \vec{m}$. The angle Ψ between the group velocity vector $\vec{w} = V\vec{m} + (I - \vec{m}\vec{m}) \cdot (\partial V/\partial \vec{m})$ and the wave vector \vec{K} is determined by $\cos\Psi = \vec{m} \cdot \vec{s}$. The more the vector \vec{w} tips out of the wave vector \vec{K} , the more the phase velocity V varies with the direction \vec{m} due to $\partial V/\partial \vec{m} \neq 0$, so the angle $\Psi = \arccos(\vec{m} \cdot \vec{s})$ grows from zero. Then, the faster the phase velocity varies with \vec{m} , the farther the vector \vec{w} tips from the vector \vec{K} . Moreover, the vector \vec{w} tips in a direction of growing the velocity, i.e. just outside of a point of a minimal value of the phase velocity in a TeO_2 -crystal [4.10]. That is why, the presence of small tips of \vec{m} from the $[1\bar{1}0]$ -axis, caused by the acoustic diffraction due to a piezoelectric transducer of finite length L , leads to the above-noted tips of \vec{w} . Thus to find the angular distribution of acoustic energy one has to estimate an additional angular contribution 2Ψ together with the beam divergence ν . A contribution 2Ψ can significantly exceed the contribution of diffraction. At the same time, the nonlinear character of the phenomenon under analysis within our article makes it very desirable to not add an additional complexity into consideration. To simplify the problem, one has to formulate the requirements to experimental conditions in such a way that the combined effect of acoustic divergence could be excluded from our studies. By this it means that the cross-section of an acoustic beam should be almost the same during its propagation along the optical aperture

of a crystal. To avoid not perfectly reliable theoretical estimations for this complicated material we use mainly experimental data in our analysis. On the basis of present knowledge, one can expect the trustworthy estimation from the following experimental data: $2 \Psi_{(a)} \approx 60^\circ$ and $2 \Psi_{(b)} \approx 20^\circ$ in the (001)- and (1 $\bar{1}$ 0)-planes, respectively [4.2]. Using these approximations, one has to take the cross-section of an acoustic beam with, i.e. $L \approx H \approx 1.2$ cm, i.e. with the cross-section $S = L \times H \approx 1.5$ cm². Such a choice of sizes for the piezoelectric transducer gives $2 \Psi_{(a)} \approx 60^\circ \approx 2.715^\circ$ and $2 \Psi_{(b)} \approx 20^\circ \approx 0.905^\circ$ that promises an acceptable uniformity for the cross-section of an acoustic beam with the tolerance of about 10% along the optical aperture $D \leq 6.0$ cm. (We understand that such an accuracy is not quite well, but it is better than not to carry out further experiments at all due to non-realistic sizes of transducer).

Now, one can estimate potential performances of the tellurium dioxide-made AOC as a dispersive component. The goals are designing similar crystalline AOC and carrying out the needed proof-of-principle experiments with this AOC.

As it follows from section 4, for the above-chosen geometry in TeO₂ crystal with the declination angle $\vartheta \approx 3.142^\circ$, the ellipticity $\rho \approx 0.37275$, and the slow shear acoustic mode with the acoustic wave vector $\vec{K} \parallel [110]$, one can write $|p_{a \text{ eff}}| \approx 0.655 \times 0.5 |p_{11} - p_{12}| \approx 0.036$, due to $p_{11} \approx 0.074$ and $p_{12} \approx 0.187$ [4.14]. One may restrict himself by only $p_{a \text{ eff}}$, because only the parameter σ_a has been used in the general solutions, see Eqs.(4.5) and (4.6). Because of the material density $\rho_0 \approx 6.0$ g/cm³, $n_O = N_O \approx 2.3297$ and $n_E \approx 2.3301$ at that angle ϑ and $\lambda = 488$ nm, one arrives at the figure of AO merit $M_2 = n_O^3 n_E^3 (p_{a \text{ eff}})^2 / (\rho_0 V^3) \approx 148 \times 10^{-18}$ s³/g. These value of M_2 demonstrates that the anomalous light scattering, governed by the pure slow shear acoustic mode in TeO₂, is sufficiently efficient and this crystal is able to provide effective three-phonon AOI.

Then, the above-chosen first maxima in light distribution require the following optimized power parameters $(\sigma_a x)_{1, \text{Opt}, k}$ associated with $f_3 \approx 65$ MHz when $\alpha = 0.1411$ cm⁻¹ and the correction factors of apodization $\kappa_k \approx 1.01139, 1.02443, 1.04345, 1.06867, \text{ and } 1.09884$, respectively. With $x \equiv L$ and $L \approx 1.2$ cm, one can find from Table 4.1 that $\sigma_{1, \text{Opt}, k} \approx 2.588, 2.742, 2.892, 3.033, \text{ and } 3.183$ cm⁻¹. Now, the standard determination for σ [4.11] with $\cos \theta \approx 1$ can be re-written specifically to the acoustic power density P_1 needed for the first maxima as

$$P_{1,k} \approx \frac{2\lambda^2 \sigma_{1\text{Opt},k}^2}{\pi^2 M_2}. \quad (4.11)$$

Thus, for example at $\lambda = 488$ nm and $f_3 \approx 65$ MHz, Eq.(4.11) gives the optimized value of $P_{1,k} \approx 20 - 33$ mW/mm², see Table 4.2.

One can exploit Eq.(4.10) with $V = 0.616 \cdot 10^5$ cm/s, $L \approx 1.2$ cm, $f_3 \approx 65$ MHz at $\lambda = 488$ nm to estimate the theoretical frequency bandwidths $\Delta f_T \approx 562$ KHz. With this result one can find the theoretically expected spectral bandwidth as $\Delta \lambda_T = \lambda \Delta f_T / f_3 \approx 42.2$ Å as well. Then, using the data related to the frequency and spectral resolution from Table 4.1, one can obtain the theoretically expected numbers N_k of resolvable spots, see Table 4.2

Table 4.2. Theoretical estimations with: $L \approx 1.2$ cm; type of the elastic mode is S [110] with $f_3 \approx 65$ MHz at $\lambda = 488$ nm; the product $\delta \lambda_K = \lambda^2 / (3 b_3 D_K)$ includes the birefringence factor b_3 . Then, $d_{S,k} = \kappa_k \lambda F/D_k$ is an ideal spot size in the approximation of geometric optics

D_k , cm	$\sigma_{1, \text{Opt}, k}$, cm ⁻¹	B_k , dB	$d_{s,k}$, μm	N_k , res. spots	$P_{1,k}$, W/cm ²
2.0	2.588	2.45	20.976	54.7	2.184
3.0	2.742	3.68	14.164	82.1	2.462
4.0	2.892	4.90	10.821	109.5	2.727
5.0	3.033	6.13	8.866	136.8	3.000
6.0	3.183	7.35	7.596	164.2	3.304

4.7. Proof-of-principal experiments

4.7.1. Experiment arrangement

First, one can estimate the potential contributions of the acoustic losses for the chosen slow shear elastic mode passing along the [110]-axis, whose displacement vector is oriented along the $[1\bar{1}0]$ -axis. Because of the coefficient of linear attenuation is $\Gamma \approx 290$ dB/(cm GHz²) in a TeO₂ single crystal [4.9], the factor α [cm⁻¹] of the amplitude acoustic losses is determined as α [cm⁻¹] = 0.1152 Γ [dB/(cm GHz²)] f^2 [GHz]. The carrier frequency $f_3 \approx 65$ MHz at the light wavelengths $\lambda = 488$ nm, specific to the non-collinear three-phonon AOI in tellurium dioxide with the tilt angle $\phi \approx 3.142^\circ$, has been chosen above. Consequently, one can estimate the amplitude factors for linear acoustic losses by γ [dB/cm] = Γf_3^2 , which gives $\gamma = 1.22525$ dB / cm and $\alpha = 0.14115$ cm⁻¹.

Additionally, one has to take into account the losses needed for converting the input electronic signal into an acoustic one, which are usually slightly exceeding 2 dB. However within these our experiments, we have decided to modify the piezoelectric transducer. The practically important problem is connected with relatively narrow frequency and spectral bandwidth of the AOC exploiting the non-collinear three-phonon AOI. The matter is that tellurium dioxide is sufficiently effective AO material, so that the bandsape width of the TeO₂-made AOC can be expanded at the cost of decreasing the efficiency of that AOC. In so doing, the thickness of upper electrode, placed over piezoelectric material, has been a little bit increased to implement the effect of oscillation damping. The goal of such a damping was to decrease the quality factor of acoustic resonance inherent in that piezoelectric transducer. Our experimental estimations have demonstrated that such a damping grew the losses for converting the electronic signal into an acoustic one up to 3.0 – 3.5 dB, while the acoustic resonance curve of that piezoelectric transducer showed a broader maximum.

Previously, we have to restrict ourselves by a maximum level $P \leq 0.5$ W/mm² of acoustic power density. However, novel design of the damped piezoelectric transducer admits the acoustic power density by a magnitude of about $P_1 \leq 3.5$ W/mm² for the acoustic beam cross section of about 1.5 cm² in the AOC under consideration. The produced estimations demonstrate that the above-required levels of the parameters P_1 and $\sigma_{1,Opt}$ for the first unit-level maxima lie in the ranges of accessible values. One can find from Eq.(4.11) that reaching the next maxima [4.10] needs much higher acoustic power densities in comparison with the first ones. This looks rather conjectural from the viewpoint of requirements for the electric strength inherent in the available piezoelectric transducer. After that, pre-experimental estimations for the TeO₂-made AOC with $D = 6.2$ cm and $L \approx 1.2$ cm can be summarized in Table 4.3. These estimations imply exploiting the slow shear elastic mode with the acoustic velocity $V = 0.616 \times 10^5$ cm/s in the scheme of the standard AO spectrum analyzer with the integrating lens of the focal distance $F = 85$ cm.

The design of the tellurium dioxide crystalline AOC under consideration, operating in the regime of the non-collinear three-phonon AOI, is presented in detail in Fig. 4.12. The piezoelectric transducer represented by a thin plate made of the 163° Y-cut LiNbO₃ single crystal has been placed on the (110) crystallographic plane of the TeO₂-crystal. It provides the excitation of a slow-shear mode acoustic beam with the cross section of about 1.5 cm² and the length $L = 1.2$ cm of interaction in the crystal. The needed Bragg and tilt angles, whose orientations are depicted in Fig. 4.12, are enumerated in Table 4.2.

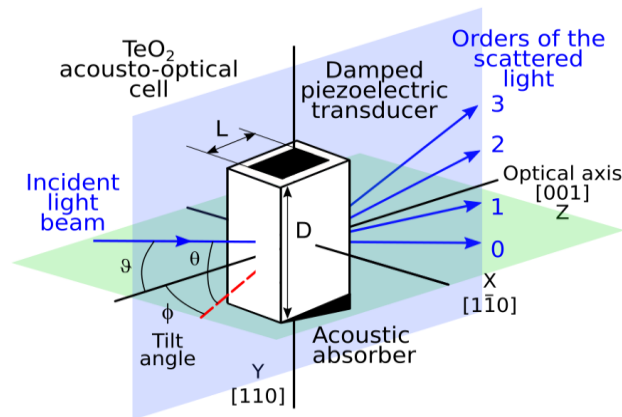


Fig. 4.12. Design of the tellurium dioxide AOC for the three-phonon AOI.

4.7.2. Experimental results

Our proof-of-principal experiments has been performed with a wide-aperture Bragg AOC based on the tellurium dioxide single crystal, which has an active optical aperture of about 6.2 cm, see Fig. 4.13. This pioneer AOC allowed a maximum input acoustic power of about 20 W. It was able to operate over all the visible range starting from the optical wavelength $\lambda = 488$ nm, which combines the convenience of operating in just the visible range with the best-expected performances inherent in this AOC. Practically, we used optical wavelength $\lambda = 488$ nm from the single frequency argon ion laser Innova 300C-I-304 (optical power 0.75 W, Coherent Inc.). The CW-light radiation has the needed elliptic state of the incident light polarization expanded along the crystallographic [110]-axis of the TeO_2 -based AOC.

This AOC was prepared to be governed by the radio-wave signals at the central frequency $f_3 \approx 65$ MHz. A set of electronic equipment for both generating and registering the corresponding electric ultra-high-frequency (UHF) radio-wave signals has been exploited. Initially, the UHF-signal, sweeping or tunable as the case requires, was applied to the electronic input port of the AOC through a wide-band UHF-amplifier HD19152 (0.15 – 230 MHz, 20 W) and the corresponding impedance-matching electronic circuits, see Fig. 4.13.

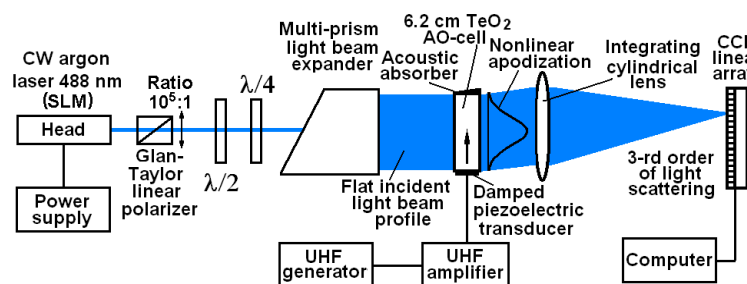


Fig. 4.13. A layout of the experimental set-up; only the 3-rd order of light scattering is depicted.

The optical part of our experiments included a 15-mm Glan-Taylor linear polarizer (the extinction ratio $\sim 10^5$), two rotating polarization plates $\lambda/2$ and $\lambda/4$ (all from Thorlabs), and a four-prism (Edmund Optics) beam expander, which operated as some kind of polarizer as well. This is why first one had to make the required estimations and then to manipulate by both the polarization plates to obtain the elliptic state of the incident light polarization with the pre-assigned ellipticity $\rho \approx 0.3727$. The polarimeter PAX5710 VIS-T (Thorlabs) was used for supervision over light beams. Elliptically polarized light after expander provided rather flat (non-uniformities were better than $\sim 10\%$) initial optical beam profile expanded in the plane of scattering. During the experiments with this beam shaper rather accurate angular adjusting of

the incident light beam had been performed. By this it means that both the correct Bragg angle of incidence and the needed tilt angle had been optimized. The 90-mm achromatic doublet lens (Edmund Optics, clear aperture 72 mm, $\Delta\lambda = 400 - 700$ nm) with the focal length of about 85 cm had been used as the integrating lens, and the multi-pixel CCD-linear array (Toshiba) consisting of $4.7 \mu\text{m}$ pixels was playing the role of a photo-detector. The layout of the experimental set-up is presented in Fig. 4.13, where only the 3-rd order of light scattering pattern is shown.

The experiments consisted of two parts. The first of them included detecting the frequency bandshape with a low oscillation damping, i.e. determining the effective bandwidth of the Bragg non-collinear three-phonon light scattering at a 0.405-level of light intensity. The second part of those experiments was related to estimating possible spectral resolution within involving this AOC into the optical spectrum analysis. It was done via measurements of individual resolvable spots in the focal plane of the integrating lens for the light deflected by into the third order of scattering. Figure 4.14 shows an example of the experimental trace for the frequency bandshape inherent in the TeO_2 -based AOC with the damped piezoelectric transducer at the central frequency about 65 MHz, which had been detected under lighting by the light-blue coherent light $\lambda = 488$ nm. The total experimental frequency bandwidth at a 0.405-level of light intensity has been estimated by $\Delta f_M \approx 798$ kHz. Precise optical measurements have been performed at the wavelength 488 nm to obtain sufficiently reliable estimations for the frequency resolution provided by the TeO_2 -made AOC together with the above-described optical system, including the CCD linear array. The performed measurements have been done with a radio-wave signal applied at the input port of the TeO_2 -cell.

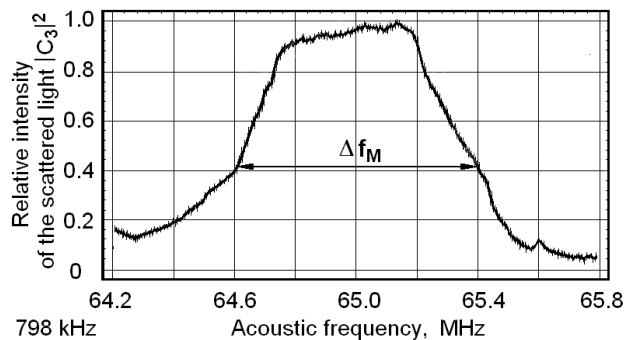


Fig. 4.14. Experimentally obtained frequency bandshape of the TeO_2 -made AOC at $f_3 \approx 65$ MHz and $\lambda = 488$ nm.

As it has been noted, our experimental results have been obtained using the integrating lens with $F = 85$ cm at the wavelength 488 nm, so that theoretically the spot sizes are $d_s^{(4)} = \kappa_4 \lambda F/D_4 \approx 11.08 \mu\text{m}$ and $d_s^{(6)} = \kappa_6 \lambda F/D_6 \approx 7.59 \mu\text{m}$. Together with this, the plot in Fig. 4.15 exhibits the experimental spot sizes $d_M^{(4)} = \kappa_4 \lambda F/D_M^{(4)} \approx 13.8 \mu\text{m}$ and $d_M^{(6)} = \kappa_6 \lambda F/D_M^{(6)} \approx 9.45 \mu\text{m}$, respectively, that correspond to the aberration factor $\zeta_M \approx 1.2437$ (which includes various optical demerits of the used wide-aperture crystal and our optical system), and consequently, to the effective apertures $D_M^{(4)} \approx 3.21$ cm and $D_M^{(6)} \approx 4.81$ cm for the AOC [$\kappa_k \approx 1.01139, 1.02443, 1.04345, 1.06867, 1.09884$, respectively, $F = 85$ cm, and $D_k = \{2.0, 3.0, 4.0, 5.0, \text{ and } 6.0\}$ cm].

The TeO_2 -crystal has rather high refractive indices. For example, the main ones are about $n_o = 2.3297$ and $n_e \approx 2.3301$ at $\lambda = 488$ nm used during the experiments. This is why one can expect significant optical attenuation inside the crystal and remarkable reflections from the facets of TeO_2 -based AOC. Undoubtedly, to minimize potential optical losses the facets of similar AOC ought to have anti-reflection coating [4.11]. Nevertheless, we have performed our proof-of-principle experiments with the AOC that have not been coated. Therefore, the relative efficiency of light scattering into the third order had been first experimentally estimated and then measured at the output facet of the AOC. In so doing, the light intensity detected at the output facet, transmitted through the cell in the absence of an external UHF electronic excitation, had been

counted as the unity. The light intensity scattered into third order in the presence of that electronic signal and measured at the output facet had been considered as the usable optical signal caused by UHF electronic signal. The ratio of this usable optical signal to the initially transmitted light intensity (both are measured at the output facet of that AOC), one can consider as the relative efficiency of AOI. Thus the relative efficiency, determined as it has been described above, had been measured at the optimal acoustic frequency about $f_3 \approx 65$ MHz at $\lambda = 488$ nm. The maximum relative efficiency at the optimal acoustic had been experimentally estimated by the value ~ 0.92 .

Figure 4.15 depicts two from a set of experimentally obtained light intensity profiles with the spot sizes of about 13.8 and 9.5 microns with the side lobe levels of $\leq 3.5\%$, which include affecting the light distribution in these spot by the acoustic losses of ~ 4.90 and 7.35 dB / aperture, respectively. These profiles had been observed from optical apertures $D_4 \approx 4.0$ cm and $D_6 \approx 6.0$ cm, using the same 6.2 cm sample of tellurium dioxide crystal. The measurements showed that the main lobes of spots gave lighted areas, which were exceeding two pixels of the CCD-row that provided acceptable resolution of a pattern from viewpoint of the sampling theorem.

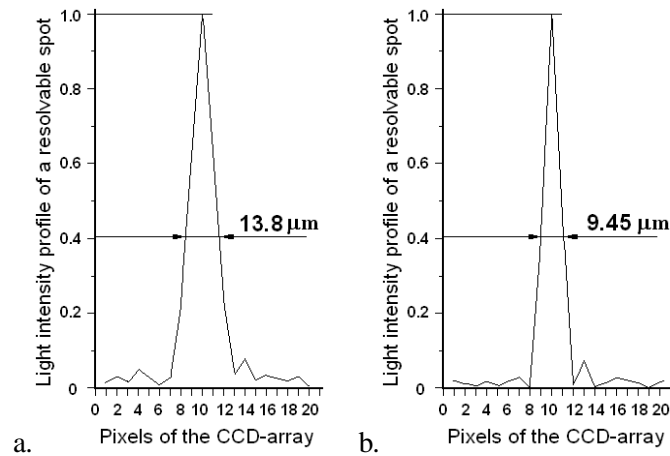


Fig. 4.15 Light intensity profiles of two individual resolvable spots for the TeO_2 -based AOC at $f_3 \approx 65$ MHz and $\lambda = 488$ nm: (a) $D_{4,M} \approx 4.0$ cm and (b) $D_{6,M} \approx 6.0$ cm.

The last data show that remarkable parts of the active optical apertures inherent in the AOC is lost due to imperfectness of the lens and AOC's crystalline material together with the total effect of linear acoustic losses $B_k = \{2.45, 3.68, 4.90, 6.13, \text{ and } 7.35\}$ dB per aperture. Therefore, instead of theoretical limits of the frequency resolutions $\delta f_{T,k} = V/3D_k$, one yields the measured values $\delta f_{k,M} = V/3D_{k,M}$, which lead to the experimentally obtained magnitudes of the spectral resolution $\delta \lambda_{k,M} = \lambda \delta f_{k,M}/f_3$ at $\lambda = 488$ nm. Then, $\Delta \lambda_M = \Delta f_M \lambda / f_3 \approx 60.05$ Å (instead of the theoretical value $\Delta \lambda_T \approx 42.20$ Å because of damping the piezoelectric transducer). Thus the experimentally obtained numbers of resolvable spots are $N_{k,M} = \Delta f_M / \delta f_{k,M} = \Delta \lambda_M / \delta \lambda_{k,M}$ spots.

In Table 4.3, the comparison of theoretical and experimental results is presented. One can see that some experimentally obtained data, namely, the frequency and spectral bandwidths as well as the numbers of resolvable spots exhibit general tendency to exceed the above-calculated theoretical values. This tendency takes place despite the presence of natural imperfectness peculiar to all the optical components in our experimental set-up. Similar results can be attributed to the use of damping the piezoelectric transducer in the developed TeO_2 -made AOC.

Finally, the maximal expected lighted length in the focal plane of the integrating lens is $L_{CE} = d_M N_M < 3.0$ mm, i.e. capabilities of the experimental optical system lie in the frames of the exploited multi-pixel CCD-array. Consequently, the best obtained results with the developed

TeO₂-made AOC are the spectral resolution $\delta\lambda_M \approx 0.351 \text{ \AA}$ at 488 nm and the resolving power exceeding $R_M \approx 13,900$ with the spectral bandwidth $\Delta\lambda_M \approx 60.0 \text{ \AA}$. These data exceed performances of the best acousto-optical spectrometers for space or airborne operations of the twenty-first century [4.15-4.17]. However, they does not have a gain compared with our recently obtained results [4.11] with calomel AOC (the spectral resolution $\delta\lambda_M \approx 0.235 \text{ \AA}$ at 405 nm and the resolving power $R_M \approx 17,200$).

Table 4.3. Comparison of theoretical and experimental data; $\Delta f_T \approx 562 \text{ kHz}$ and $\Delta f_M \approx 798 \text{ kHz}$; $\Delta\lambda_T \approx 42.20 \text{ \AA}$ and $\Delta\lambda_M \approx 60.05 \text{ \AA}$; at $\lambda = 488 \text{ nm}$

$D_{k,T}, \text{ cm}$	$D_{k,M}, \text{ cm}$	κ_k	$\delta f_{k,T}, \text{ kHz}$	$\delta f_{k,M}, \text{ kHz}$	$\Delta\lambda_{k,T}, \text{ \AA}$	$\Delta\lambda_{k,M}, \text{ \AA}$	$N_{k,T}$	$N_{k,M}$
2.0	1.59	1.0113	10.27	12.917	0.771	0.970	55	62
3.0	2.35	1.0243	6.85	8.726	0.514	0.655	82	92
4.0	3.084	1.0435	5.13	6.658	0.385	0.512	110	120
5.0	3.76	1.0687	4.11	5.463	0.309	0.411	137	146
6.0	4.40	1.0984	3.42	4.672	0.257	0.351	164	171

Thus our new experimental results for the above-studied TeO₂-made AOC, exploiting the three-phonon AOI, are not better than our recent data [4.11] obtained within two-phonon AOI in calomel. Although formally the three-phonon AOI has a 1.5-time advantage, in reality the used now and allowing three-phonon AOI TeO₂-crystal exhibits 1.775 times faster acoustic velocity and 1.26 times higher linear acoustical losses, which both have reduced the spectral resolution here.

4.8. Conclusion

The state-of-the-art AO devices based on TeO₂ are applied to various technological needs and very different uses. From precise frequency shifters [4.18] to optical coherence microscopy using filtering properties of the AO cell [4.19]. Also, present investigations are focused in improving the characteristics for imaging applications in the mid-infrared range [4.20], acousto-optical lens [4.21] and the operation of TeO₂ AO cells in low temperatures for space-borne spectroscopy [4.22]. Together we this, our group has made some advances oriented to astrophysical spectroscopy for visible spectra as well as for radio-wave observations using acousto-optics, which are apart from the present thesis [4.23-4.26]. All these investigations are related to the Bragg regime for the one-phonon AO interaction. Our present work, in contrast to the avenues of mentioned publications, is towards the use of the three-phonon AO interaction in the Bragg regime.

The three-phonon AOI is the most complicated non-collinear multi-phonon process in an anisotropic crystal. Generally, each direct line, associated with the acoustic phonons, is able to cross a pair of wave-vector surfaces, reflecting two eigen-states of polarization, as a maximum 4 times, indicating 4 orders of light scattering. In the particular case, when these intersections are equidistant, one can observe the three-phonon AOI in Bragg regime. Here, we have developed the most completed up to now theory of this phenomenon and distinguished novel physical aspects specific to its nonlinearity when three-phonon AOI is excited by acoustic waves of finite amplitude. Additionally, we have considered this phenomenon in birefringent crystals exhibiting moderate linear acoustic attenuation. In so doing, specific AO nonlinearity in behavior of the scattered light intensity and frequency mismatch under strongly fixed angular alignment has been identified. These features have been investigated both theoretically and experimentally. Initially, an opportunity of shaping a sequence of the local unit-level maxima under optimal ratio between photo-elastic constants for normal and anomalous processes had been found. Then, a multitude of the transfer function profiles specific to those unit-level maxima in light scattered into the third order have been revealed. We have selected the transfer function inherent in the first unit-level maximum, as a profile that requires the lowest acoustic power to be achieved. Already this profile is able to give us a chance to study the main peculiarities of the non-collinear three-phonon AOI and to analyze preliminary its applicability

for the precise spectrum analysis of optical signals. Such a selection was based on achieving the unit-level maximum in the third order of light distribution that requires a minimal acoustic power for manifesting that nonlinearity. After that, we have found and characterized an additional degree of freedom specific to the non-collinear three-phonon AOI that gives in particular the following. It allows us to achieve close to 100% efficiency with the fixed acoustic frequency for various optical wavelengths due to existing the distinguished birefringence factor inherent in this phenomenon. Moreover, this factor can be varied via choosing the tilt angle whose acceptability depends on the symmetry of a crystal. Owing to the linear interplay between the scattered light and the incident one despite the AO nonlinearity, one can apply the three-phonon AOI to an advanced optical spectrum analysis with the triple accuracy. By this it means that this phenomenon can be taken for developing an advanced approach to the parallel spectrum analysis of optical signals. Therefore, due to three-phonon AOI gives tripling the spectral resolution in the acousto-optics, a possibility for the spectrum analysis of optical signals with the significantly improved resolution has been demonstrated as well.

Under such conditions, only linear acoustic attenuation represents a limiting factor, which restricts potential performances of spectrum analysis. Nevertheless, the effect of moderate acoustic losses has its specific due to its interplay with AO nonlinearity. The analysis have shown that the result of similar interplay leads to appearing the nonlinear apodization. In our case of the fixed acoustic frequency and variable optical aperture, one can obtain various levels of the acoustical losses per the corresponding optical aperture of the AOC to avoid unnecessary strong limitations during the current stage of investigations.

To demonstrate the details of our analysis and to realize possible experiments the crystals of tetragonal symmetry had been considered as examples. Then, very effective (but complicated) AO material, namely, the TeO_2 -single crystal had been selected as one of the best options for our goals. The needed theoretical, practical, and pre-experimental estimations have been performed to design a unique wide-aperture AOC based on the TeO_2 -crystal. The experiments had been carried out at $\lambda = 488$ nm with various portions of a 6.2 cm-optical aperture AOC based on TeO_2 -crystal exited by the slow shear acoustic mode along the [110]-axis. Along with this, we had explored the use of the tilt angle to proceed specific directions for light waves propagation in order to select adequate refractive indices within the AOI. The results of proof-of-principal experiments with this AOC, governed by elastic waves of finite amplitude, confirm in general the previously developed theory and numerical estimations [4.27]. Moreover, these findings are able evidently to open a new page in the suggested innovative technique for the modern optical spectrum analysis with the significantly progressed spectral resolution based on the three-phonon AOI.

General conclusions

The transmission function of the collinear acousto-optic interaction can be manipulated with the acoustic power density. The spectral resolution can be improved by sacrificing a portion of the efficiency.

The effects of photorefraction and induced absorption do not affect the performance of an acousto-optical cell made of lithium niobate in potential astrophysical observations.

The two- and three-phonon acousto-optical interaction can improve the resolution of the non-collinear interaction in anisotropic crystals, two and three times respectively.

The additional degree of freedom, i.e. the tilt angle, can be used to regulate the frequency needed for the two- and three-phonon acousto-optical interaction.

The diffracted beam from a two- and three phonon acousto-optical interaction due to acoustic waves of finite amplitude exhibits a non-linear apodization.

Bibliography

Chapter 1

- [1.1] A. Korpel, *Acousto-Optics*, 2nd. Ed., Marcel Dekker, New York, (1997).
- [1.2] G. New, *Introduction to Nonlinear Optics*, Cambridge University Press (2011).
- [1.3] A. Yariv & P. Yeh, *Optical Waves in Crystals*, John Wiley & Sons (1983).
- [1.4] J. E. B. Oliveira, C.K. Jen, “Backward collinear acousto-optic interactions in bulk materials”, *Applied Optics* Vol. 29 No. 6 (1990).
- [1.5] C. Kittel, *Introduction to Solid State Physics*, 8th. Ed., John Wiley & Sons, New York, (2004).
- [1.6] D.A. Pinnow. “Guidelines for the selection of acousto-optic materials.” *IEEE Journal of Quantum Electronics*. Vol.QE-6 (1970), 223-238.
- [1.7] T. M. Smith, A. Korpel, “Measurement of light-sound interaction efficiencies in solids”, vol. QE-1 (1965), 283 -284.
- [1.8] E. I. Gordon, “Figure of merit for acousto-optical deflection and modulation devices”, *IEEE J. Quantum Electronics*, vol. QE-2, (1966), 104-105.
- [1.9] R.W. Dixon, “Acoustic diffraction of light in anisotropic media”, *IEEE J. of Quantum Electronics*. Vol.QE-3, no.2 (1967), 85-93.

Chapter 2

- [2.1] J.L. Bertaux, D. Fonteyn, O. Korablev, at al. “SPICAM: Studying the global structure and composition of the martian atmosphere.” In *European Space Agency; SP-1240 “Mars Express: A European mission to the red planet.”* Edited by A. Wilson (ESA Publications Division, 2004).
- [2.2] J.L. Bertaux, D. Nevejans, O. Korablev, at al. “SPICAV on Venus Express: Three spectrometers to study the global structure and composition of the Venus atmosphere.” *Planetary and Space Science*. Vol.55, issue 12, October (2007), 1673-1700.
- [2.3] R.W. Dixon, “Acoustic diffraction of light in anisotropic media”, *IEEE J. of Quantum Electronics*. Vol.QE-3, no.2 (1967), 85-93.
- [2.4] S.E. Harris, S.T.K. Nich, R.S. Fiegelson, “CaMoO₄ electronically tunable optical filter”, *Appl. Phys. Lett.* Vol.17, no.5 (1970), 223-225.
- [2.5] I.C. Chang, “Tunable acousto-optic filter utilizing acoustic beam walk-off in crystal quartz”, *Appl. Phys. Lett.* Vol.25, no.9 (1974), 323-324.
- [2.6] J.A. Kusters, D.A. Wilson, D.L. Hammond, “Optimum crystal orientation for acoustically tuned optical filters”, *J. Opt. Soc. Am.* Vol.64, no.4 (1974), 434-440.
- [2.7] E.T. Aksenov, N.A. Esepkina, A.S. Shcherbakov, “Acousto-optical filter with a LiNbO₃-crystal” *Tech. Phys. Lett*, Vol.2, no.3 (1976), 83-84.
- [2.8] J.D. Fichter, M. Gottlieb, J.J. Conroy. *Appl. Phys. Lett.* Vol.34, no.1 (1979), 1-3.
- [2.9] V.I. Balakshy, V.N. Parygin, L.I. Chrkov. *Physical Principles of Acousto-Optics*, Radio I Svyaz, Moscow, 1985.
- [2.10] A. Korpel. *Acousto-Optics*, 2-nd Ed., Marcel Dekker, New-York, 1997.
- [2.11] F.T.S. Yu. *Introduction to Information Optics*, Academic Press, San Diego, 2001.
- [2.12] A.S. Shcherbakov, A. Aguirre Lopez, “Shaping the optical components of solitary three-wave weakly coupled states in a two-mode waveguide”, *Optics Express*. Vol.11, no.14 (2003), 1643-1649.

- [2.13] A.S. Shcherbakov, A. Aguirre Lopez, “Binary encoded modulation of light based on collinear three-wave acousto-optical weakly coupled states”, *Journal of Optics A: Pure and Applied Optics*. Vol.5 (2003), 471-477.
- [2.14] Yu.I. Sirotnin and M.P. Shaskolskaya. *Fundamentals of Crystal Physics*. (Mir Publishers. Moscow. 1982).
- [2.15] V.G. Dmitriev, G.G. Gurzadyan and D.N. Nikogosyan, *Handbook of Nonlinear Optical Crystals* 3-rd Ed. (Springer, Berlin, 1999).
- [2.16] A.A. Blistanov. *Crystals for Quantum and Nonlinear Optics*. 2-nd Ed. (MISIS, Moscow, 2007).
- [2.17] D.A. Pinnow. “Guidelines for the selection of acousto-optic materials.” *IEEE Journal of Quantum Electronics*. Vol.QE-6 (1970) 223-238.
- [2.18] Handbook “Acoustical Crystals”. Edited by M.P. Shaskolskaya. (Nauka Publishers, Moscow. 1988).
- [2.19] D. A. Bryan, R. Gerson and H. E. Tomaschke, “Increased optical damage resistance in lithium niobate”, *Applied Physics Letters* 44 (1984) 847 – 849.
- [2.20] K. L. Sweeney, L. E. Halliburton, D. A. Bryan, R. R. Rice, Robert Gerson and H. E. Tomaschke, “Point defects in Mg-doped lithium niobate” *Journal of Applied Physics* 57 (1985), 1036 – 1044.
- [2.21] H. Minemoto, T. Nishiyama and K. Shibuya, U. S. Patent No. 6,903,862 B2 (2005).
- [2.22] N. Waasem, A. Markosyan, M. M. Fejer, and K. Buse “Green-induced blue absorption in MgO-doped lithium niobate crystals”, *Optics Letters* 38 (16) (2013), 2953-2956.
- [2.23] T. Volk, N. Rubinina, and M. Wöhlecke, “Optical-damage-resistant impurities in lithium niobate”, *J. Opt. Soc. Am. B* 11 No. 9 (1994), 1681-1687.
- [2.24] F. Xin, G. Zhang, F. Bo, H. Sun, Y. Kong, J. Xu, T. Volk, and N. M. Rubinina, “Ultraviolet photorefraction at 325 nm in doped lithium niobate crystals”, *Journal of Applied Physics* 107 (2010), 033113.
- [2.25] Alexandre S. Shcherbakov, **Adán Omar Arellanes**, Sergey A. Nemov, “Transmission function of the collinear acousto-optical filter controlled by acoustic waves of finite amplitude”, *Optical Engineering* 52 (6), 064001, (2013).
- [2.26] Alexandre S. Shcherbakov, **Adan Omar Arellanes**, Sergey A. Nemov, “Transmission function collinear acousto-optical interaction occurred by acoustic waves of finite amplitude”, *J. Opt. Soc. Am. B* 30 (12), 3174-3183, (2013).
- [2.27] Alexandre S. Shcherbakov, **Adan Omar Arellanes**, Sergey A. Nemov, “Collinear dissipative weakly coupled acousto-optical states governed by the acoustic waves of finite amplitude in a two-mode medium with linear optical losses”, *J. Opt. Soc. Am. B* 31 (5), 953-962 (2014).
- [2.28] **Adan Omar Arellanes**, Alexandre S. Shcherbakov, Sergey A. Nemov, “Dissipative collinear weakly coupled acousto-optical states”, *Proc. SPIE* 9347, 93471R (2015).
- [2.29] **Adan Omar Arellanes**, Alexandre S. Shcherbakov, Emanuele Bertone, “A novel collinear LiNbO₃ acousto optical tunable filter with the improved range of transmission and spectral resolution”, *Proc. SPIE* 9347, 93470E (2015).
- [2.30] Alexandre S. Shcherbakov, **Adan Omar Arellanes**, and Emanuele Bertone, “Advanced collinear LiNbO₃ acousto-optical filter for astrophysical spectroscopy in the near ultraviolet: exploring the high spectral resolution”, *J. Astron. Telesc. Instrum. Syst.* 1 (4), 045002 (2015).
- [2.31] Alexandre S. Shcherbakov, **Adan O. Arellanes**, Emanuele Bertone, “Modern collinear LiNbO₃ acousto-optical filter for optical spectroscopy: the exploration of efficiency and spectral resolution”, *Proc. SPIE* 9744, 97441M (2016).

Chapter 3

- [3.1] N. Uchida and N. Niizeki, “Acoustooptic deflection materials and techniques”, *Proc. IEEE*, Vol. 61, No. 8, 1073-1092, (1973).

- [3.2] L. Wei, S. Yu-Nan, C. Fang, & B. Long, "Feasibility of Non-Collinear TeO₂ Acousto-Optic Tunable Filters Used in the Optical Communication", *Chinese Physics Letters*, 24(4), 986–989, (2007).
- [3.3] *Catalog of Acousto-Optic Tunable Filters - Free Space* (Brimrose Corporation of America, Baltimore, Md., 2014).
- [3.4] C. Zhang, H. Wang, & Y. Qiu, "Study of the Imaging Performance for a Noncollinear Acousto-Optic Tunable Filter", 2010 Symposium on Photonics and Optoelectronics Chengdu, China, 1–4. (2010).
- [3.5] N. S. Prasad, "Deep-UV based acousto-optic tunable filter for spectral sensing applications", *Int. J. High Speed Electron. Syst.* 17, 857–866 (2007).
- [3.6] V. B. Voloshinov and N. Gupta, "Ultraviolet-Visible Imaging Acousto-Optic Tunable Filters in KDP", *Appl. Opt.* 43, 3901 (2004).
- [3.7] N. Gupta, "Materials for imaging acousto-optic tunable filters", *Proc. of SPIE*, vol.9100, 91000C (2014).
- [3.8] M. Gottlieb, A. P. Goutzoulis, and N. B. Singh, "Fabrication and characterization of mercurous chloride acoustooptic devices", *Appl. Opt.* 26, 4681–7 (1987).
- [3.9] N. Gupta, "Investigation of a mercurous chloride acousto-optic cell based on longitudinal acoustic mode", *Appl. Opt.* 48, C151 (2009).
- [3.10] A. S. Shcherbakov, Je. Maximov, and S. E. Balderas Mata, "Shaping the dissipative collinear three-wave coupled states in a two-mode medium with a square-law nonlinearity and linear non-optical losses", *J. Opt. A* 10, 025001, (2008).
- [3.11] A. Korpel. *Acousto-Optics*, 2nd Ed., N.-Y., (Marcel Dekker, 1997).
- [3.12] V.I. Balakshy, V.N. Parygin, L.I. Chirkov. *Physical Principles of Acousto-Optics*, Radio I Svyaz, Moscow, (1985).
- [3.13] M. P. Shaskolskaya, *Acoustic Crystals*, Moscow, (Nauka, 1982).
- [3.14] I. C. Chang, *Handbook of Optics*, Volume II, Chapter 12, 2nd. Ed., edited by M. Bass, (McGraw Hill, 1994).
- [3.15] J. F. Nye, *Physical Properties of Crystals: Their Representation by Tensors and Matrices*, (Oxford University Press, 1985).
- [3.16] M. Born, E. Wolf, *Principles of Optics*, Cambridge, UK, (Cambridge Univ. Press, 1999).
- [3.17] A. S. Shcherbakov and A. O. Arellanes, "Advanced regime of the noncollinear two-phonon acousto-optical interaction governed by elastic waves of finite amplitude and optical spectrum analysis", *J. Opt. Soc. Am. B* 32, 1930-1940 (2015)
- [3.18] H. Schmitzer, H. Wagner, W. Dultz, and M. Kühnelt, "Phase-matched third-harmonic generation in mercury-(I)-chloride", *Appl. Opt.* 41 (3), 470-474 (2002).
- [3.19] W. R. Klein and B. D. Cook, "Unified approach to ultrasonic light diffraction", *IEEE Trans. Sonics & Ultrasonics*, SU-14, 123 - 134 (1967).
- [3.20] R. W. Damon, W. T. Maloney, D. H. McMahon, "Interaction of light with ultrasound: phenomena and applications," in *Physical Acoustics: Principles and Methods*, W. P. Mason, R. N. Thurston, eds., Vol. VII, pp. 273–366, New York (Academic Press, 1970).
- [3.21] A. P. Goutzoulis and D. R. Pape, *Design and fabrication of acousto-optic devices* (M. Dekker, 1994).
- [3.22] J. W. Goodman, *Introduction to Fourier optics*, 3rd Ed.(Viva Books, 2007).
- [3.23] A. S. Shcherbakov, A. O. Arellanes, S. A. Nemov, "Transmission function collinear acousto-optical interaction occurred by acoustic waves of finite amplitude", *J. Opt. Soc. Am. B*, vol. 30, No. 12, 3174-3183, (2013).
- [3.24] V. Ya. Molchanov, V. M. Lyuty, V. F. Esipov, S. P. Anikin, O. Yu. Makarov, and N. P. Solodovnikov, "An Acousto-Optical Imaging Spectrophotometer for Astrophysical Observations", *Astronomy Letters*, Vol. 28, No. 10, pp. 713–720 (2002).

- [3.25] O. Korablev, J-L. Bertaux, A. Grigoriev, E. Dimarellis, Yu. Kalinnikov, A. Rodin, C. Muller, D. Fonteyn, "An AOTF-based spectrometer for the studies of Mars atmosphere for Mars Express mission", *Advances in Space Research*, 29 (2), pp. 143–150 (2002)
- [3.26] O. Korablev, A. Fedorova, J.L. Bertaux, A.V. Stepanov, A. Kiselev, Yu.K. Kalinnikov, A.Yu. Titove, F. Montmessin, J.P. Dubois, E. Villard, V. Sarago, D. Belyaev, A. Reberac, E. Neefs, "SPICAV IR acousto-optic spectrometer experiment on Venus Express", *Planetary and Space Science Vol. 65, Issue 1*, pp. 38–57 (2012).
- [3.27] A. S. Shcherbakov and **A. O. Arellanes**, "Calomel-made crystalline acousto-optical cell designed for an advanced regime of noncollinear two-phonon light scattering", *Opt. Eng.* 55 (3), 037107 (2016).
- [3.28] Alexandre S. Shcherbakov and **Adan O. Arellanes**, "Characterization of the non-collinear acousto-optical cell based on calomel (Hg₂Cl₂) crystal and operating within the two-phonon light scattering ", *Proc. SPIE 9742, 97421V* (2016).
- [3.29] Alexandre S. Shcherbakov and **Adan O. Arellanes**, "Studying an advanced regime of the non-collinear two-phonon light scattering for applications to the optical spectrum analysis", *Proc. SPIE 9731, 973118* (2016).
- [3.30] Alexandre S. Shcherbakov and **Adan Omar Arellanes**, "Features of the non-linearity specific to two-phonon light scattering controlled by elastic waves with linear losses: potentials for high-resolution spectral analysis", *Applied Optics* 55 (18), 4833-4842 (2016).
- [3.31] Alexandre S. Shcherbakov, **Adan Omar Arellanes**, and Vahram Chavushyan, "Precise parallel optical spectrum analysis using the advanced two-phonon light scattering combined with the cross-disperser technique," *Appl. Opt.* 55 (34), 9648-9658 (2016).

Chapter 4

- [4.1] A. S. Shcherbakov, S. E. Balderas Mata, Je. Maximov, and A. Aguirre Lopez. "The existence of five-wave non-collinear acousto-optical weakly coupled states." *Journal of Optics A: Pure and Applied Optics* 10, pp.1-10, (2008).
- [4.2] V. I. Balakshy, V. N. Parygin, and L. I. Chirkov, *Physical Principles of Acousto-Optics*, Radio I Svyaz, Moscow, (1985).
- [4.3] V. Yu. Rakovsky, A. S. Shcherbakov, "Multi-phonon Bragg scattering of the light by elastic waves", *Technical Physics* 35 (7), pp. 815-819 (1990).
- [4.4] J. Xu and R. Stroud, *Acousto-Optic Devices: Principles, Design and Applications*, (Wiley, 1992).
- [4.5] A. S. Shcherbakov, E. Tepichin Rodriguez, A. Aguirre Lopez, "An all-optical 4-bit register based on a four-order scattering of light by coherent acoustic phonons in single crystals", *Mexican Journal of Physics (Revista Mexicana de Fisica)* 50 (3), pp. 297-305, (2004).
- [4.6] A. Korpel. *Acousto-Optics*, 2nd Ed., N.-Y., (Marcel Dekker, 1997).
- [4.7] R. W. Damon, W. T. Maloney, D. H. McMahon, "Interaction of light with ultrasound: phenomena and applications," in *Physical Acoustics: Principles and Methods*, W. P. Mason, R. N. Thurston, eds., Vol. VII, pp. 273–366, New York (Academic Press, 1970).
- [4.8] N. Uchida, "Optical Properties of Single-Crystal Paratellurite (TeO₂)", *Phys. Rev. B* 4, 3736 (1971).
- [4.9] M. P. Shaskolskaya, *Acoustic Crystals*, Moscow, (Nauka, 1982).
- [4.10] Yu. I. Sirotin and M. P. Shaskolskaya, *Fundamentals of Crystal Physics*, (Mir Publishers, 1983).
- [4.11] A. S. Shcherbakov and **A. O. Arellanes**, "Calomel-made crystalline acousto-optical cell designed for an advanced regime of non-collinear two-phonon light scattering", *Opt. Eng.* 55 (3), 037107 (2016).
- [4.12] W. R. Klein and B. D. Cook, "Unified approach to ultrasonic light diffraction", *IEEE Trans. Sonics & Ultrasonics*, SU-14, 123 - 134 (1967).

- [4.13] A. P. Sukhorukov, *Theory of Waves* (Nauka, Moscow, 1990).
- [4.14] I. C. Chang, *Handbook of Optics*, M. Bass, ed., 2nd ed. (McGraw-Hill, 1994), Vol. II, Chap. 12.
- [4.15] V. Y. Molchanov et al., "An acousto-optical imaging spectrophotometer for astrophysical observations," *Astron. Lett.* **28**, 713–720 (2002).
- [4.16] O. Korablev, J. L. Bertaux, A. Grigoriev et al., "An AOTF-based spectrometer for the studies of Mars atmosphere for Mars Express mission," *Adv. Space Res.* **29**, 143–150 (2002).
- [4.17] O. Korablev, A. Fedorova, J. L. Bertaux et al., "SPICAV IR acousto-optic spectrometer experiment on Venus Express," *Planet. Space Sci.* **65**, 38–57 (2012).
- [4.18] A. Dieulangard, J. C. Kastelik, S. Dupont, and J. Gazelet, "Acousto-optic wide band optical low-frequency shifter," *Appl. Opt.* **52**, 8134-8141 (2013).
- [4.19] A. S. Machikhin, V. E. Pozhar, A. V. Viskovatykh, and L. I. Burmak, "Acousto-optical tunable filter for combined wideband, spectral, and optical coherence microscopy," *Appl. Opt.* **54**, 7508-7513 (2015).
- [4.20] S. Valle, J. Ward, C. Pannell, and N. P. Johnson, "Acousto-optic tunable filter for imaging application with high performance in the IR region", Proc. SPIE **9359**, *Optical Components and Materials XII*, 93590E (2015).
- [4.21] Z. Zhou, L. Li, J. Wang, Q. Hu, and Sh. Zeng, "Beam deformation within an acousto-optic lens," *Opt. Lett.* **40**, pp. 2197-2200 (2015).
- [4.22] S. N. Mantsevich, O. I. Korablev, Yu. K. Kalinnikov, A. Yu. Ivanov, A. V. Kiselev, "Wide-aperture TeO₂ AOTF at low temperatures: operation and survival", *Ultrasonics* **59**, pp. 50-58 (2015).
- [4.23] Alexandre S. Shcherbakov, **Adan Omar Arellanes Bernabe**, Vahram Chavushyan, "Designing the acousto-optical cell for optical spectrometer incorporated into the Guillermo Haro Astrophysical Observatory", Proc. of SPIE Vol. 8855 885507 (2013).
- [4.24] Alexandre S. Shcherbakov, **Adan Omar Arellanes Bernabe**, Vahram Chavushyan, "Designing an acousto-optical spectrometer for Guillermo Haro Astrophysical Observatory", Proc. of SPIE Vol. 8842 88420O (2013).
- [4.25] Alexandre S. Shcherbakov, **Adán Omar Arellanes**, Vahram Chavushyan, "Optical spectrometer with acousto-optical dynamic grating for Guillermo Haro Astrophysical Observatory", *International Journal of Astronomy and Astrophysics* **3**, 376-384, (2013).
- [4.26] Miguel Chavez Dagostino, Alexandre S. Shcherbakov, **Adan Omar Arellanes**, Vahram Chavushyan, "High-resolution broadband millimeter-wave astrophysical spectrometer with triple product acousto-optical processor", *International Journal of Astronomy and Astrophysics* **3**, 421-430, (2013).
- [4.27] Alexandre. S. Shcherbakov and **Adan Omar Arellanes**, "Features of the three-phonon acousto-optical interaction due to elastic waves of finite amplitude and an advanced spectrum analysis of optical signals," *J. Opt. Soc. Am. B* **33**, 1852-1864 (2016).

Statements

The acousto-optical non-linearity leads to principally new capabilities on acousto-optics

The revealed optical degree of freedom can play a fundamental role for the performances of the acousto-optic interaction

The acousto-optical non-linearity can be realized within state-of-the-art experiments

Application of these novelties leads to really significant improvements in the performance for spectrum analysis